ISSN 1451 - 9372 (Print)
ISSN 2217 - 7434 (Online)
OCTOBER-DECEMBER 2023
Vol.29, Number 4, 253-337

Chemical Industry & Chemical Engineering Quarterly

The AChE Journal for Chemical Engineering,
Biochemical Engineering, Chemical Technology,
New Materials, Renewable Energy and Chemistry
www.ache.org.rs/ciceq

Journal of the
Association of Chemical Engineers of
Serbia, Belgrade, Serbia

Chemical Industry & Chemical Engineering
CI&CEQuarterly

Journal of the
Association of Chemical Engineers of
Serbia, Belgrade, Serbia

Chemical Industry & Chemical Engineering Quarterly

Vol. 29 Belgrade, October-December 2023 No. 4

Chemical Industry & Chemical Engineering Quarterly (ISSN 1451-9372) is published quarterly by the Association of Chemical Engineers of Serbia, Kneza Miloša 9/I, 11000 Belgrade, Serbia

Editor:
Vlada B. Veljković
veljkovic@yahoo.com

Editorial Office:
Kneza Miloša 9/I, 11000 Belgrade, Serbia
Phone/Fax: +381 (0)11 3240 018
E-mail: shi@ache.org.rs
www.ache.org.rs

For publisher:
Ivana T. Drvenica

Secretary of the Editorial Office:
Slavica Desnica

Marketing and advertising:
AChE Marketing Office
Kneza Miloša 9/I, 11000 Belgrade, Serbia
Phone/Fax: +381 (0)11 3240 018

Publication of this Journal is supported by the Ministry of Education, Science and Technological Development of the Republic of Serbia

Subscription and advertisements make payable to the account of the Association of Chemical Engineers of Serbia, Belgrade, No. 205-2172-71, Komercijalna banka a.d., Beograd

Computer typeface and paging:
Marija B. Tasić

Journal manager:
Aleksandar B. Dekanski

Printed by:
Faculty of Technology and Metallurgy, Research and Development Centre of Printing Technology, Karnegijeva 4, P.O. Box 3503, 11120 Belgrade, Serbia

Abstracting/Indexing:
Articles published in this Journal are indexed in *Thompson Reuters* products: *Science Citation Index - Expanded*™ - access *via Web of Science*®, part of *ISI Web of Knowledge*℠

CONTENTS

The activities of the Association of Chemical Engineers of Serbia are supported by:

MINISTRY OF SCIENCE, TECHNOLOGICAL DEVELOPMENT AND INNOVATION OF REPUBLIC OF SERBIA

Faculty of Technology and Metallurgy, University of Belgrade

Faculty of Science, University of Novi Sad

Institute for Technology of Nuclear and Other Mineral Raw Materials, Bekgrade

Faculty of Technology, University of Novi Sad

Institute of Chemistry, Technology and Metallurgy, University of Belgrade

Faculty of Technical Sciences University of Novi Sad

Faculty of Technology, University of Niš, Leskovac

Faculty of Technical Sciences, University of Priština, Kosovska Mitrovica

IMS Institute, Belgrade

DCP HEMIGAL
Leskovac

Elixir Prahovo

CI&CEQ
Chemical Industry & Chemical Engineering Quarterly

Available online at
Association of the Chemical Engineers of Serbia *AChE*
www.ache.org.rs/CICEQ

Chem. Ind. Chem. Eng. Q. 29 (4) 253–262 (2023) CI&CEQ

ANA LUIZA MENDES[1]
DAIMON JEFFERSON JUNG DE OLIVEIRA[2]
THAMAYNE VALADARES DE OLIVEIRA[3]
FERNANDO AUGUSTO PEDERSEN VOLL[2]
RAFAEL BRUNO VIEIRA[3]
ANDRE BELLIN MARIANO[4]

[1]Universidade Federal do Paraná, Engenharia e Ciência dos Materiais, Curitiba, Brazil

[2]Universidade Federal do Paraná, Engenharia Química, Curitiba, Brazil

[3]Universidade Federal de Uberlândia, Faculdade de Engenharia Química, Uberlândia, Brazil

[4]Universidade Federal do Paraná, Departamento de Engenharia Elétrica, Curitiba, Brazil

SCIENTIFIC PAPER

UDC 66.067.1.081:582.26

EFFECTS OF MICROALGAL CONCENTRATION AND pH WITH FLOCCULANT ON MICROFILTRATION

Article Highlights

- Low microalgae concentration and pH were used with flocculant in microfiltration
- The use of flocculant at lower pH can maximize microalgae separation
- Filtration-flocculation was successfully conducted in crossflow filtration

Abstract

To make algal biomass a suitable feedstock for fuel and bioproducts, a practical way of dewatering and concentrating algal cells must be devised. In this study, a system comprising microfiltration membranes combined with a flocculant was developed on a low-cost ceramic substrate to harvest Tetradesmus obliquus efficiently. The effects of tannin-based flocculant concentration, microalgal concentration, and pH on microfiltration were studied. Permeate flux was evaluated for 5400 s through experiments to analyze the total resistance and the fouling mechanism. Results show that the cake filtration model best represented the data. The experiments at pH 4 and 0.06 kg/m^3 of microalgae (with flocculant) showed improved results with a reduction in the J/J_0 (permeate flux/initial flux) ratio of 39%. In addition, the effects of critical flux, transmembrane pressure, and fouling mechanism on microfiltration were investigated under the best conditions studied. Applying the stepping method to the critical flux yielded a permeate flux of 2.2×10^{-5} m^{3}m^{-2}s^{-1}. The 70 kPa condition showed the highest permeate flux (3.0×10^{-5} m^{3}m^{-2}s^{-1}) and a low cake pore blocking coefficient (k) obtained by the modified Hermia model. This study showed that Tanfloc at low pH could maximize microalgal separation in membrane processes.

Keywords: ceramic membrane, concentration, pH, microalgal, microfiltration.

Currently, microalgae have emerged as promising and innovative biomass sources. Microalgae have several applications: biodiesel production, healthy food, fish feed, biohydrogen production, and carbon dioxide fixation [1]. However, due to the small size of microalgae and their growth in highly dilute conditions, it is important to use an efficient harvest technique [2–4]. Operations currently used in microalgal harvest include centrifugation, sedimentation, flocculation, and membrane filtration [5,6]. Two- or three-step operations in microalgal harvest have been found economical and easily adaptable [7]. For example, a flocculation-sedimentation process combined with membrane filtration has been studied [8–10].

Microalgal harvest through the flocculation-sedimentation process (first step) has already been

Correspondence: T. Valadares de Oliveira, Universidade Federal de Uberlândia, Faculdade de Engenharia Química, 38408-144 Uberlândia, Brazil.
E-mail: thamayne.valadares@ufu.br
Paper received: 25 January, 2022
Paper revised: 16 November, 2022
Paper accepted: 15 December, 2022

https://doi.org/10.2298/CICEQ220125032M

studied using various inorganic flocculants such as salts of polyvalent cations like $Al_2(SO_4)_3$, $Fe_2(SO_4)_3$ and $FeCl_3$; organic flocculants like chitosan, Tanfloc, Flopam, and Zetag [11,12]; and bioflocculants [13].

In particular, Tanfloc is an organic, biodegradable, and nontoxic flocculant (natural polymer). It is a trademark of Tanac (Brazil) and a tannin-based product modified by a physicochemical process. It is obtained from *Acacia mearnsii* and is a high-power flocculant [6,14,15]. Microalgal species, such as *Monoraphidium* sp., showed >90% biomass recovery using 50 mg/L of Tanfloc, while *Scenedesmus* sp. showed 96.7 ± 1.0% maximum flocculation with a Tanfloc concentration of 210 mg/L [11,16]. However, the relatively high flocculant concentration and the long sedimentation time influence the microalgal purity and processing time, respectively [17].

After flocculation, a dewatering technique (second step) is used for the microalgal slurry to increase the biomass concentration and lower the water content [1]. The flocculation-sedimentation process followed by membrane microfiltration can increase the volume of the processed raw material without significantly increasing the capital cost applied to the project with high microalgal retention [8]. The membrane microfiltration technique effectively solves this problem and is largely acknowledged as an effective separation method [18]. Ceramic membranes have several advantages that enable their use in separation processes: good thermal stability, chemical inertia, high permeability, mechanical strength, long lifetime, and low thermal conductivity [5,19].

Some disadvantages of membrane technologies (microfiltration and ultrafiltration) are reported in the literature, such as fouling and reduced permeate flux over time. These technologies mainly work using the size exclusion principle; therefore, the mechanisms of particle deposition on the surface (external fouling) or in the membrane pores (internal fouling) decrease permeate flux. However, fouling can cause an irreversible loss of membrane permeability, causing operational system failure [20].

Membrane fouling decreases permeate flux, and replacement increases operational and maintenance costs. However, when microfiltration is combined with a flocculation-sedimentation process, they increase the harvest efficiency and reduce the operational and maintenance costs [21,22]. Several control strategies can be applied to prevent fouling, such as pH modification, microalgal concentration, flocculants, and the critical flux concept [14,15]. The critical flux concept has been proposed as a smooth and easy fouling control method that takes advantage of the transition of a filtration system between non-fouling and particle deposition states by tuning the system flux rate [23,24].

In this study, a flocculation-sedimentation process followed by microfiltration was conducted. The effects of variation in flocculation-sedimentation parameters on microfiltration were evaluated. The flocculation-sedimentation (first step) parameters studied were microalgal concentration, pH, and the presence or absence of Tanfloc (flocculant). Permeate flux, total resistance, the modified Hermia model, and fouling were analyzed during microfiltration (second step). Subsequently, under conditions of minimum fouling, improvement in *Tetradesmus obliquus* microfiltration and fouling management was investigated through the critical flux using the stepping method.

MATERIALS AND METHODS

Microalgae

Microalgae *Tetradesmus obliquus* (GenBank accession number: KY436159.1) were isolated according to Corrêa *et al.* (2017) [25]. The algal was cultivated with Chu medium (mg/L) [25].

Membranes

Faience clay [Cermassas-Pastacer Ltda.] was used as raw material to produce ceramic membranes. Cationic manioc starch grade Superion 300 with a degree of substitution in the range of 0.033–0.036 mol/mol (Grupo Horizonte-Agrícola Horizonte Ltd., PR, Brazil) and eggshell residues were used as additives. Natural clay was modified through thermal treatment at a temperature of 500 °C for 24 h with a heating rate of 5 °C/min. Before thermal treatment, natural clay was dried in an oven for 12 h and dry ground in a bench ball mill. After thermal treatment, the samples were dry ground in a bench ball mill with alumina balls for 4 h and homogenized with a #60 Tyler mesh (2.5×10^{-4} m) sieve. Egg shells were also homogenized using sieving using the same sieve mesh.

A low-cost membrane prepared with cationic starch (2.5% w/w) and eggshell (2.5% w/w) was used [20,26]. The dimensions of the membrane are 0.20 m (length), 1.07×10^{-2} m (internal diameter), and 1.88×10^{-2} m (external diameter) [26]. The membrane properties are the average pore size (1.0 μm), porosity (55%), and flexural strength (15.16 MPa) [26]. Mercury porosimetry was performed on a mercury porosimeter, model Autopore IV 9500 V1.07.

Microfiltration

Water. Hydraulic permeability was conducted to 6.94×10^{-5} m^3s^{-1} and pressure ranging from 20 kPa to 100 kPa and a temperature of 25 °C [5]. Then, the

membrane was compacted with a flux of 6.94×10^{-5} m^3s^{-1} and a pressure of 100 kPa for 2700 s [5].

Microalgae. Experiments were performed under the conditions of Table 1. The flocculant ratio was 8% w/w (flocculant/microalgae), corresponding to 0.05 kg/m^3 of flocculant per liter of microalgae suspension. These experiments were developed at the pressure of 30 kPa. The microalgae suspension contained 0.06 kg of microalgae/m^3. In addition, the permeate flux over time, the retention of microalgae, and the evolution of J/J_0 were analyzed.

Table 1. Microfiltration experiments based on flocculation parameters: microalgal concentration, pH, and presence or absence of flocculant.

Experiment	Microalgae Concentration (kg/m^3)	pH	Flocculant
1	0.02	4	No
2	0.02	7	No
3	0.02	4	Yes
4	0.02	7	Yes
5	0.06	4	No
6	0.06	7	No
7	0.06	4	Yes
8	0.06	7	Yes

Critical flux

According to the results of the previous experiments, the condition used in these tests was 0.06 kg/m^3 at pH 4. The critical flux experiments were done as described elsewhere [27]. The pure water flux was measured at four pressures (squares filled with a straight line) in 600 s intervals. First, pressure increases of 10 kPa were performed. Subsequently, the pressure was decreased at 10 kPa intervals.

Permeate flux

The permeate flux was calculated by Eq. (1):

$$J = \frac{V_p}{A_p t} \tag{1}$$

where V_p is the volume of the permeate (m^3), A_p is the membrane area (m^2), and t is the operating time (s).

Retention of microalgae

The turbidity removal (*TUR*) was calculated by Eq. (2):

$$TUR(\%) = \frac{T_0 - T_F}{T_0} \tag{2}$$

where T_0 and T_F are the turbidity in the feed and the permeate streams, respectively, in NTU.

Resistance

Total resistance was calculated by Eq. (3):

$$R_T = \frac{TMP}{\mu J} \tag{3}$$

where R_T is the total resistance (m^{-1}), *TMP* is the transmembrane pressure (kPa), J is the filtration flux ($m^3 m^{-2} h^{-1}$), and μ is the dynamic viscosity of water at (0.8937×10^{-3} Pa s).

Fouling mechanism

The modified Hermia model, Eq. (4), was used [20,28–30].

$$-\frac{dJ}{dt} = k(J_{SS} - J)J^{2-n} \tag{4}$$

The model parameters (k, J_{ss}, and n) were estimated by Eq. (5):

$$OF(k, J_{ss}, n) = \sum_{i=1}^{NE}\left(J_i^{\exp} - J_i^{calc}\right)^2 \tag{5}$$

where J_i^{calc} and J_i^{exp} are calculated and experimental values, NE is the number of experimental points used in the parameter estimation, OF is the objective function, J_i^{calc} is the calculated permeate flux, and J_i^{exp} is the experimental permeate flux.

All simulations, parameter estimation, and statistical analyses were realized in Scilab: using the function fminsearch and the Nelder-Mead algorithm. The parameters were calculated according to Bainy *et al.* [31]. The blocking index and its expanded uncertainty (at 95%) were used to identify the most probable fouling mechanism of each membrane [20].

RESULTS AND DISCUSSION

Membrane

The membranes were characterized, and mercury porosimetry showed the pore size distribution from 0.1 μm to 8 μm (average pore size of 0.82 μm). Zhou *et al.* (2009) studied an alumina microfiltration membrane modified with nanocrystalline TiO_2 and a pore size of 0.2 μm [32]. The small size of some algal cells is typically in the range of 2 mm–40 mm [33]. Laksono *et al.* [34] concluded that the microalgae form larger aggregates or flocs with the addition of flocculant; thus, less fouling is expected with the flocculated microalgae and also observed that flocculation can be used as a pretreatment before membrane filtration to control fouling.

Flocculation

Tanfloc has an average molecular mass of 1.70 kDa (2.82×10^{-24} kg) [14]. Due to its high charge

density and low molecular weight, the mechanism of Tanfloc has been suggested to be coagulation [35,36]. The cell surfaces of microalgae have predominantly carboxylic (-COOH) and amine (-NH_2) groups [7]. The carboxylic groups above pH 4–5 are negatively charged, while the amine groups are uncharged [7]. In this study, the pH range studied was 4–7. Positively charged polymers such as Tanfloc neutralize the negative charges; thus, electrostatic repulsion decreases, and aggregates or flakes form [37]. The experiments performed on the membrane showed that the potential is negatively charged in this pH range (4 to 7).

Figure 1 illustrates the flocculation (coagulation mechanism)/microfiltration process of microalgae in nature and flocculated microalgae.

Microalgal concentration and pH

The results of the evolution of (J/J_0) (permeate flux/initial flux) versus time are shown in Figures 2 and 3. For all experiments, the decrease for J/J_0 became stable after 2700 s. However, after the entire process (5400 s of microfiltration), the normalized specific flux decreased by about 40% for the concentration condition of 0.02 kg/m^3. Except for experiment 1, which showed the highest reduction J/J_0 (51% reduction). For the experiments with a microalgal concentration of 0.06 kg/m^3, the decreases in J/J_0 values were greater than 48%, except for the experiment at pH 4 with flocculant, which showed a 39% reduction. Discart *et al.* [10] studied the dosage of coagulants ($FeCl_3$ and chitosan) before filtration [10]. Both coagulants increased the filtration efficiency, and they concluded that the coagulant type and dosage should be optimized per membrane.

Figures 4 and 5 show the results of the modified Hermia modeling for the different experimental conditions tested according to Table 1. Figures 4 and 5 show the decline of the flux for the experiments.

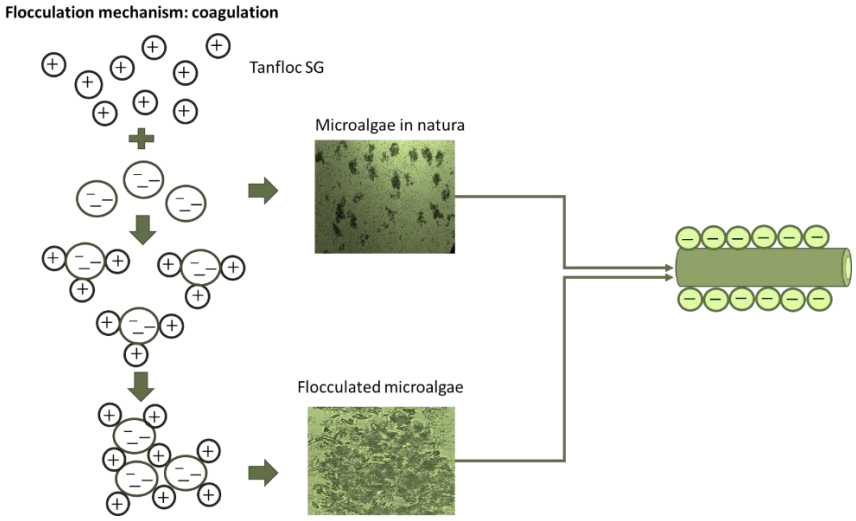

Figure 1. Illustration of the flocculation (coagulation mechanism)/microfiltration process of microalgae in nature and flocculated microalgae.

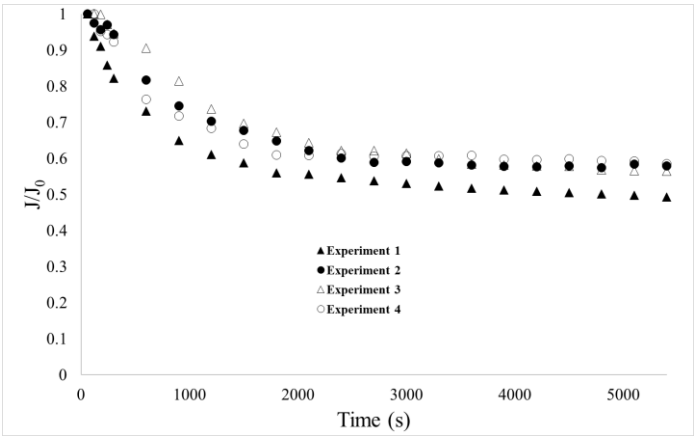

Figure 2. J/J_0 results for 0.02 kg/m^3 microalgal concentration and pH (4 and 7).

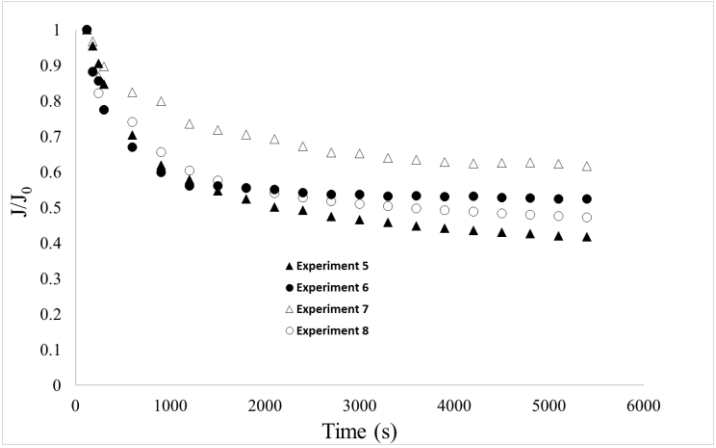

Figure 3. J/J_0 results for 0.06 kg/m^3 microalgal concentration and pH (4 and 7).

The permeate flux decreased slightly with increasing microalgal concentration, as fouling increased when the microalgal concentration increased. The experiments without flocculant increased fouling, as discussed in Membrane.

The cake filtration model provides the best fit (Table 2). The values for the cake blocking coefficient (k) were statistically equal for experiments 1, 2, 4, and 5, while the values obtained for experiments 3, 6, 7, and 8 were statistically different. Laksono *et al.* [34] observed that the cake filtration model was the most relevant. A similar conclusion was observed by Jiang *et al.* [3].

Turbidity removal of the experiments is shown in Table 3. The turbidity removal varied from 93% to 99%. The experiments with a flocculant (3, 4, 7, and 8) had a higher *TUR* than the experiments without a flocculant (1, 2, 5, and 6); due to the mechanism of Tanfloc flocculation (coagulation) [35,36].

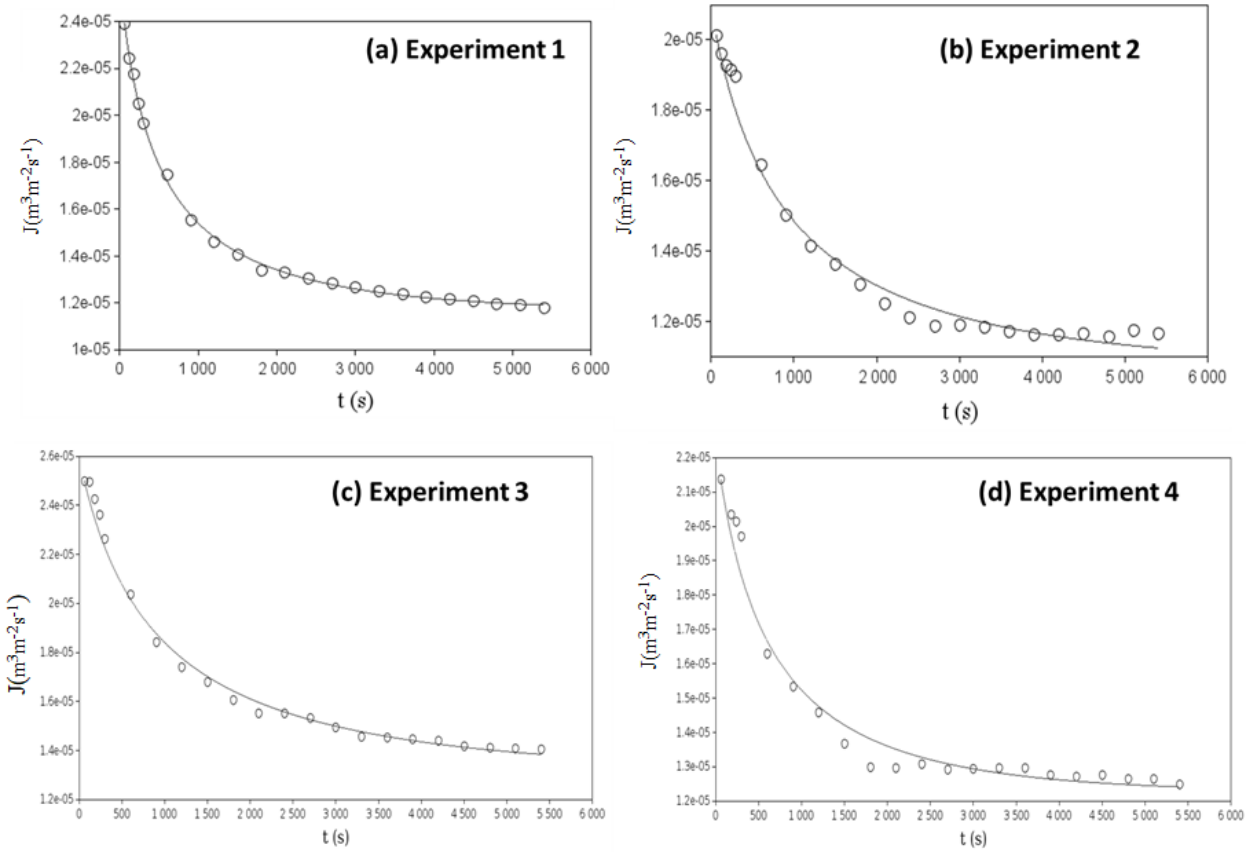

Figure 4. Predictions for the cake models to experiments 1–4 at 30 kPa and 25 °C (lines: estimated results; circles: experimental data).

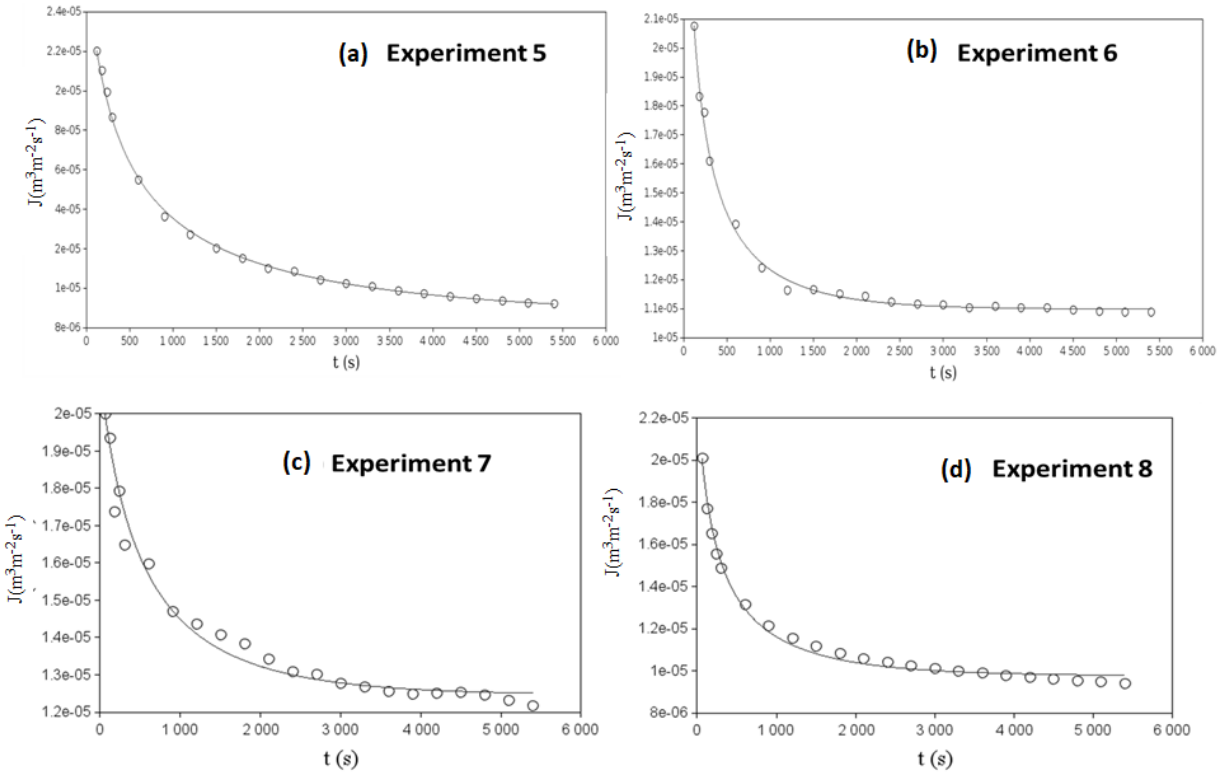

Figure 5. Predictions for the cake models to experiments 5–8 at 30 kPa and 25 °C (lines: estimated results; circles: experimental data).

Table 2. Values for the cake blocking coefficient (k).

Experiment	Cake filtration model (n=0) ×10^{-6}	Uncertainty ×10^{-6}
1	3.75	0.2565
2	3.05	0.7475
3	4.06	0.3430
4	10.27	0.9722
5	1.96	0.3839
6	3.90	0.9248
7	5.17	0.1596
8	9.12	0.1427

Table 3. Turbidity removal (%).

Experiment	Turbidity removal (%)	Standard deviation
1	96.4	0.2
2	93.8	0.2
3	97.5	0.3
4	99.1	0.1
5	93.0	0.1
6	94.0	0.2
7	98.1	0.3
8	99.2	0.2

Critical flux

A concentration of 0.06 kg/m^3 and pH 4 were chosen. This condition was selected because it showed lower fouling. The results of permeate flux versus pressure for the pressure-stepping method are shown in Figure 6. The water showed higher flux values. The microalgae provided greater fouling. The microalgae permeate flux had a linear increase up to the pressure of 70 kPa. After this pressure, the flux remained almost constant. The critical flux was between 2.11×10^{-5} and 2.22×10^{-5} m^{3}m^{-2}s^{-1}. Increasing the pressure was impossible to increase the flux beyond 2.2522×10^{-5} m^{3}m^{-2}s^{-1}. The literature divides the critical flux forms into strong and weak [38]. The results with microalgae were in the weak form. There is rapid fouling for the weak form, and the flux-TMP ratio is lower than the pure water line [38]. Due to the membrane characteristics used, the flux values for pure water are much higher than those with microalgae (Figure 6). The literature evaluated critical flux values for different microalgal concentrations and microalgae species ranging from 15 Lm^{-2}h^{-1} to 50 Lm^{-2}h^{-1} [39]. The operating conditions of 30 kPa (below critical flux), 70 kPa (at critical flux), and 100 kPa (above critical flux) were analyzed to evaluate the three regimes shown in Figure 6.

Effect of TMP on filtration behavior

Figure 7 shows (a) the permeate flux at different pressures (30 kPa; 70 kPa; 100 kPa) and (b) J/J_0 at different pressures (30 kPa; 70 kPa; 100 kPa). When Pore blocking is not apparent in a short-term flow test (or TMP), the total filtration resistance keeps constant; because particle accumulation on the membrane surface does not increase significantly. Under these

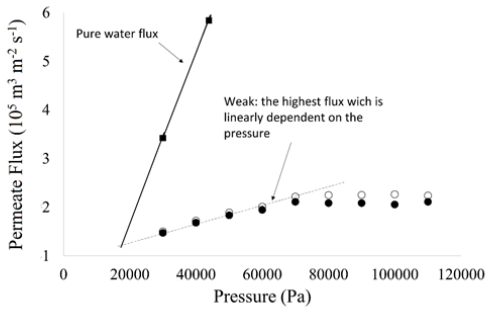

Figure 6. Permeate flux versus pressure for the pressure-stepping method (25°C, pH 4, 0.06 kg/m^3).

conditions, the permeate flux increases linearly with TMP. However, if particle accumulation expressively increases with permeate flux, the filtration resistance increases with time, and the permeate flux stop increasing linearly with TMP. Therefore, the breaking point of the linear flow-TMP profile can be considered a critical flux [24]. Based on the results in Figure 7a, higher TMP showed higher initial flux due to the higher driving force. The pressure of 100 kPa potentiated fouling at the membrane surface, resulting in a decline in permeate flux. The permeate flux became stable after 2160 s in the TMP of 70 kPa. The 70 kPa was the condition that showed the best permeate flux results after 5400 s, with a value of 3.05×10^{-5} m^{3}m^{-2}s^{-1}.

The decrease of J/J_0 (Figure 7(b)) was lower at 30 kPa and 70 kPa. TMP at 30 kPa and 70 kPa went through a slow decline stage, and the total decline was almost 39% and 32%, respectively, while at 100 kPa, there was a decrease of 62%. The flux obtained during the subcritical regime does not show a significant drop with time, while the supercritical regime shows a significant drop [3,40]. In this study, the critical flux was at 70 kPa. The membranes under subcritical conditions had superior antifouling performance, but the 70 kPa pressure performed close to the 30 kPa condition.

The total resistance was dependent on the pressure. The results show that the total fouling resistance increased with permeate volume/filtration area (Figure 8). The membranes at 70 kPa had the lowest total resistance and highest permeate volume/filter area. Operation at pressures below the critical flux is favorable for controlling membrane fouling [41]. Methodologies have been widely studied to reduce microalgae harvesting costs to promote economic viability. The cake pore blocking coefficient (k) (Table 4) at lower pressure is higher than for higher pressures (70 kPa and 100 kPa).

It can be seen from Table 4 that at low pressure, there was a significantly higher coefficient, while at critical pressure, it had the lowest coefficient. It was observed in this work that the most relevant factors were the concentration and pH, and at a concentration of 0.06 kg/m^3, there was a greater reduction of J/J_0, which represented greater fouling.

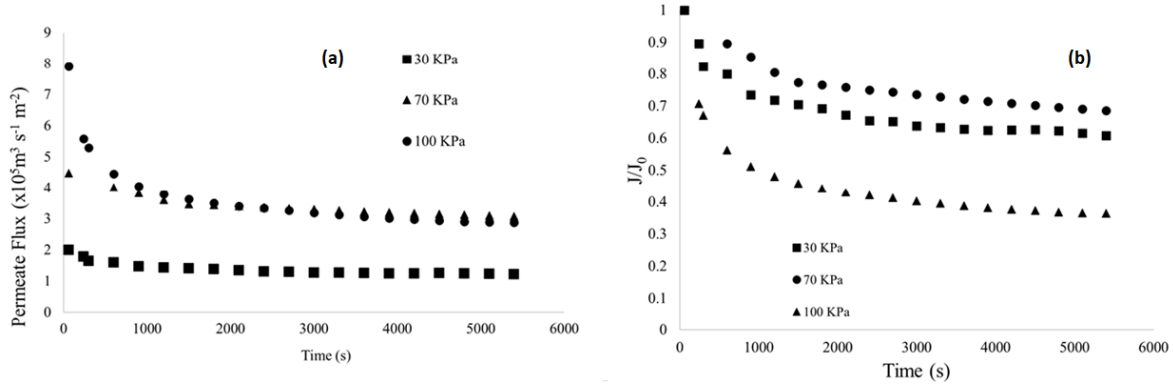

Figure 7. (a) Permeate flux at different pressures; (b) J/J_0 at different pressures.

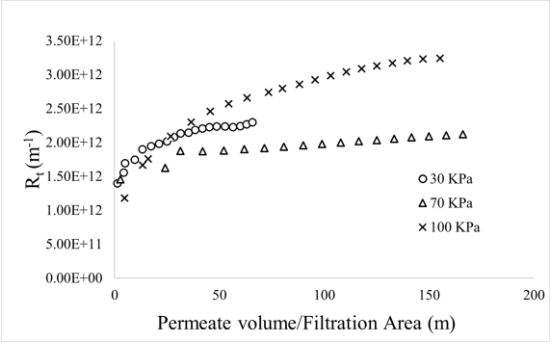

Figure 8. (a) Total fouling resistance with the variation of permeate volume/Filtration area (V/A).

Table 4. Estimated parameters of the model.

Pressure (kPa)	Cake filtration model (n=0) ×10^{-6}	Uncertainty ×10^{-6}
30	4.43	0.4327
70	0.46	0.0660
100	0.71	0.0762

CONCLUSION

The flocculation-sedimentation process followed by microfiltration was investigated, and the conclusions are:

The membranes were characterized, and mercury porosimetry showed the pore size distribution from 0.1 to 8 μm (average pore size of 0.82 μm).

The experiments at pH 4 and 0.06 kg·m^3 of microalgae (with flocculant) showed improved results with a reduction in the J/J_0 ratio of 39%, demonstrating the potential of flocculation to control fouling.

The results of the modified Hermia modeling showed that the cake filtration model best represented the data, which was expected because Tanfloc promotes aggregate or floc formation through coagulation. Therefore, the turbidity removal rate varied from 93% to 99%.

The membranes (0.06 kg·m^3 and pH 4 with flocculant) in the critical regime had better antifouling characteristics than those in the supercritical and subcritical regimes. Applying the stepping method to the critical flux yielded permeate flux of 2.2×10^{-5} m^{3}m^{-2}s^{-1}. The 70 kPa condition showed the highest permeate flux (3.0×10^{-5} m^{3}m^{-2}s^{-1}) and a low cake pore blocking coefficient (k) obtained by the modified Hermia model.

The filtration-flocculation process showed promising results in crossflow microfiltration, verifying the strong interaction between filtration and flocculation.

ACKNOWLEDGEMENT

The authors thank the Brazilian National Council of Scientific and Technological Development - CNPq (Grant 425125/2018-1) and Araucaria Foundation - Support for Scientific and Technological Development of Paraná. They also thank the Federal University of Paraná (UFPR) and the Technology Sector from UFPR for infrastructural support.

NOMENCLATURE

Symbols

J	permeate flux (m^{3}m^{-2}s^{-1})
V	permeate volume (m^3)
A	membrane area (m^2)
t	operating time (s).
TUR	turbidity removal (%)
T	turbidity (NTU)
R	resistance (m^{-1})
TMP	transmembrane pressure (kPa)
k	resistance coefficient
n	blocking index
OF	objective function
J/J_0	normalized specific flux

Greek letters

M	viscosity (Pa s)

Subscripts

p	Permeate
F	streams
0	feed
T	total
Ss	steady-state

REFERENCES

[1] K.H. Min, D.H. Kim, M. Ki, S.P. Pack, Bioresour. Technol. (2021) 126404. https://doi.org/10.1016/j.biortech.2021.126404.

[2] M.K. Danquah, L. Ang, N. Uduman, N. Moheimani, G.M. Forde, J. Chem. Technol. Biotechnol. 84 (2009) 1078–1083. https://doi.org/10.1002/jctb.2137.

[3] S. Jiang, Y. Zhang, F. Zhao, Z. Yu, X. Zhou, H. Chu, Algal Res. 35 (2018) 613–623. https://doi.org/10.1016/j.algal.2018.10.003.

[4] Z. Zhao, A. Ilyas, K. Muylaert, I.F.J. Vankelecom, Bioresour. Technol. 309 (2020) 123367. https://doi.org/10.1016/j.biortech.2020.123367.

[5] J.D. de Oliveira Henriques, M.W. Pedrassani, W. Klitzke, A.B. Mariano, J.V.C. Vargas, R.B. Vieira, Appl. Clay Sci. 150 (2017) 217–224. https://doi.org/10.1016/j.clay.2017.09.017.

[6] R.H.R. Hanashiro, C.B. Stoco, T. V de Oliveira, M.K. Lenzi, A.B. Mariano, R.B. Vieira, Can. J. Chem. Eng. 0 (2019). https://doi.org/10.1002/cjce.23467.

[7] D. Vandamme, I. Foubert, K. Muylaert, Trends Biotechnol. 31 (2013) 233–239. https://doi.org/10.1016/j.tibtech.2012.12.005.

[8] Z. Zhao, K. Muylaert, I.F.J. Vankelecom, Water Res. 198 (2021) 117181. https://doi.org/10.1016/j.watres.2021.117181.

[9] Z. Zhao, Y. Li, K. Muylaert, I.F.J. Vankelecom, Sep. Purif. Technol. 240 (2020) 116603. https://doi.org/10.1016/j.seppur.2020.116603.

[10] V. Discart, M.R. Bilad, R. Moorkens, H. Arafat, I.F.J. Vankelecom, Algal Res. 9 (2015) 55–64. https://doi.org/10.1016/j.algal.2015.02.029.

[11] F. Roselet, D. Vandamme, M. Roselet, K. Muylaert, P.C. Abreu, Bioenergy Res. 10 (2017) 427–437. https://doi.org/10.1007/s12155-016-9806-3.

[12] A.I. Barros, A.L. Gonçalves, M. Simões, J.C.M. Pires, Renew. Sustain. Energy Rev. 41 (2015) 1489–1500. https://doi.org/10.1016/j.rser.2014.09.037.

[13] G. Kandasamy, S.R.M. Shaleh, Appl. Biochem. Biotechnol. 182 (2017) 586–597. https://doi.org/10.1007/s12010-016-2346-7.

[14] N.F.H. Selesu, T. V. de Oliveira, D.O. Corrêa, B. Miyawaki, A.B. Mariano, J.V.C. Vargas, R.B. Vieira, Can. J. Chem. Eng. 94 (2016) 304–309. https://doi.org/10.1002/cjce.22391.

[15] T. Nishimura, G.V. Garcia Lesak, L. Alves Xavier, R. Bruno Vieira, A. Bellin Mariano, Chem. Eng. Technol. 45 (2022) 230–237. https://doi.org/10.1002/ceat.202100490.

[16] R. Gutiérrez, F. Passos, I. Ferrer, E. Uggetti, J. García, Algal Res. 9 (2015) 204–211. https://doi.org/10.1016/j.algal.2015.03.010.

[17] C. Wan, M.A. Alam, X.Q. Zhao, X.Y. Zhang, S.L. Guo, S.H. Ho, J.S. Chang, F.W. Bai, Bioresour. Technol. 184 (2015) 251–257. https://doi.org/10.1016/j.biortech.2014.11.081.

[18] M. Mouiya, A. Abourriche, A. Bouazizi, A. Benhammou, Y. El Hafiane, Y. Abouliatim, L. Nibou, M. Oumam, M. Ouammou, A. Smith, H. Hannache, Desalination. 427 (2018) 42–50. https://doi.org/10.1016/j.desal.2017.11.005.
[19] J.D.D.O. Henriques, M.W. Pedrassani, W. Klitzke, T.V. De Oliveira, P.A. Vieira, A.B. Mariano, R.B. Vieira, Rev. Mater. 24 (2019). https://doi.org/10.1590/s1517-707620190004.0826.
[20] W. de Melo, G.V.G. Lesak, T.V. de Oliveira, F.A.P. Voll, A.F. Santos, R.B. Vieira, Mater. Res. 25 (2022). https://doi.org/10.1590/1980-5373-mr-2021-0365.
[21] F. Wicaksana, A.G. Fane, P. Pongpairoj, R. Field, J. Memb. Sci. 387-388 (2012) 83–92. https://doi.org/10.1016/j.memsci.2011.10.013.
[22] G. Singh, S.K. Patidar, J. Environ. Manage. 217 (2018) 499–508. https://doi.org/10.1016/j.jenvman.2018.04.010.
[23] M.T. Alresheedi, O.D. Basu, B. Barbeau, Chemosphere. 226 (2019) 668–677. https://doi.org/10.1016/j.chemosphere.2019.03.188.
[24] J. Luo, S.T. Morthensen, A.S. Meyer, M. Pinelo, J. Memb. Sci. 469 (2014) 127–139. https://doi.org/10.1016/j.memsci.2014.06.024.
[25] D.O. Corrêa, B. Santos, F.G. Dias, J.V.C. Vargas, A.B. Mariano, W. Balmant, M.P. Rosa, D.C. Savi, V. Kava, C. Glienke, J.C. Ordonez, Int. J. Hydrogen Energy. 42 (2017) 21463–21475. https://doi.org/10.1016/j.ijhydene.2017.05.176.
[26] L.A. Xavier, T.V. de Oliveira, W. Klitzke, A.B. Mariano, D. Eiras, R.B. Vieira, Appl. Clay Sci. 168 (2019) 260–268. https://doi.org/10.1016/j.clay.2018.11.025.
[27] M. Mänttäri, M. Nyström, J. Memb. Sci. 170 (2000) 257–273. https://doi.org/10.1016/S0376-7388(99)00373-7.
[28] B.G. Choobar, M.A. Alaei Shahmirzadi, A. Kargari, M. Manouchehri, J. Environ. Chem. Eng. 7 (2019) 103030. https://doi.org/10.1016/j.jece.2019.103030.
[29] M.J. Corbatón-Báguena, M.C. Vincent-Vela, J.M. Gozálvez-Zafrilla, S. Álvarez-Blanco, J. Lora-García, D. Catalán-Martínez, Sep. Purif. Technol. 170 (2016) 434–444. https://doi.org/10.1016/j.seppur.2016.07.007.
[30] M.C. Vincent Vela, S. Álvarez Blanco, J. Lora García, E. Bergantiños Rodríguez, Chem. Eng. J. 149 (2009) 232–241. https://doi.org/10.1016/j.cej.2008.10.027.
[31] E.M. Bainy, E.K. Lenzi, M.L. Corazza, M.K. Lenzi, Therm. Sci. 21 (2017) 41–50. https://doi.org/10.2298/TSCI160422241B.
[32] J. Zhou, X. Zhang, Y. Wang, X. Hu, A. Larbot, Desalination. 235 (2009) 102–109. https://doi.org/10.1016/j.desal.2008.01.013.
[33] L. Brennan, P. Owende, Renew. Sustain. Energy Rev. 14 (2010) 557–577. https://doi.org/10.1016/j.rser.2009.10.009.
[34] S. Laksono, I.M.A. ElSherbiny, S.A. Huber, S. Panglisch, Chem. Eng. J. 420 (2021) 127723. https://doi.org/10.1016/j.cej.2020.127723.
[35] H. Salehizadeh, N. Yan, Biotechnol. Adv. 32 (2014) 1506–1522. https://doi.org/10.1016/j.biotechadv.2014.10.004.
[36] U. Suparmaniam, M. Kee, Y. Uemura, J. Wei, K. Teong, S. Hoong, Renew. Sustain. Energy Rev. 115 (2019) 109361. https://doi.org/10.1016/j.rser.2019.109361.
[37] M.R. Bilad, V. Discart, D. Vandamme, I. Foubert, K. Muylaert, I.F.J. Vankelecom, Bioresour. Technol. 138 (2013) 329–338. https://doi.org/10.1016/j.biortech.2013.03.175.
[38] R.W. Field, D. Wu, J.A. Howell, B.B. Gupta, J. Memb. Sci. 100 (1995) 259–272. https://doi.org/10.1016/0376-7388(94)00265-Z.
[39] T. De Baerdemaeker, B. Lemmens, C. Dotremont, J. Fret, L. Roef, K. Goiris, L. Diels, Bioresour. Technol. 129 (2013) 582–591. https://doi.org/10.1016/j.biortech.2012.10.153.
[40] P. Le Clech, B. Jefferson, I.S. Chang, S.J. Judd, J. Memb. Sci. 227 (2003) 81–93. https://doi.org/10.1016/j.memsci.2003.07.021.
[41] R.W. Field, G.K. Pearce, Adv. Colloid Interface Sci. 164 (2011) 38–44. https://doi.org/10.1016/j.cis.2010.12.008.

ANA LUIZA MENDES[1]
DAIMON JEFFERSON JUNG DE OLIVEIRA[2]
THAMAYNE VALADARES DE OLIVEIRA[3]
FERNANDO AUGUSTO PEDERSEN VOLL[2]
RAFAEL BRUNO VIEIRA[3]
ANDRE BELLIN MARIANO[4]

[1]Universidade Federal do Paraná, Engenharia e Ciência dos Materiais, Curitiba, Brazil

[2]Universidade Federal do Paraná, Engenharia Química, Curitiba, Brazil

[3]Universidade Federal de Uberlândia, Faculdade de Engenharia Química, Uberlândia, Brazil

[4]Universidade Federal do Paraná, Departamento de Engenharia Elétrica, Curitiba, Brazil

NAUČNI RAD

EFEKTI KONCENTRISANJA MIKROALGI SA FLOKULANTOM I pH NA MIKROFILTRACIJU

Da bi biomasa algi postala pogodna sirovina za gorivo i bioproizvode, mora se osmisliti praktičan način njenog dehidratisanja i koncentrisanja. U ovom radu je razvijen sistem koji se sastoji od jeftinih keramičkih mikrofiltracionih membrana kombinovanih sa flokulantom, kako bi se efikasno sakupio Tetradesmus oblikuus. Proučavani su efekti koncentracije flokulanta na bazi tanina, koncentracije mikroalgi i pH na mikrofiltraciju. Tok permeata je procenjen tokom 90 min kroz eksperimente radi analize ukupnog otpora i mehanizma začepljenja. Rezultati pokazuju da model filtracione pogače najbolje predstavlja podatke. Eksperimenti pri pH 4 i 0,06 kg/m^3 mikroalgi (sa flokulantom) pokazali su poboljšane rezultate sa smanjenjem odnosa J/J_0 (fluks permeata/početni fluks) od 39%. Pored toga, istraženi su efekti kritičnog fluksa, transmembranskog pritiska i mehanizma začepljenja na mikrofiltraciju u najboljim uslovima. Primenom metode koraka na kritični fluks dobijen je fluks permeata od 2,2 × 10^{-5} m^{3}m^{-2}s^{-1}. Pri pritisku od 70 kPa postignut je najveći fluks permeata (3,0 × 10^{-5} m^{3}m^{-2}s^{-1}) i nizak koeficijent blokiranja pora pogače (k) dobijen modifikovanim Hermia modelom. Ovaj rad je pokazao da Tanfloc pri niskom pH može maksimizirati odvajanje mikroalgi u membranskim procesima.

Ključne reči: keramička membrana, koncentracija, pH, mikroalge, mikrofiltracija.

CI&CEQ
Chemical Industry & Chemical Engineering Quarterly

Available online at
Association of the Chemical Engineers of Serbia AChE
www.ache.org.rs/CICEQ

Chem. Ind. Chem. Eng. Q. 29 (4) 263–271 (2023) CI&CEQ

VANDERLEI RODRIGUES COSTA[1]
LUANA MARCELE CHIARELLO[1]
VANDERLEIA BOTTON[1]
EDÉSIO LUIZ SIMIONATTO[2]
VINICYUS RODOLFO WIGGERS[1]
HENRY FRANÇA MEIER[1]
LAÉRCIO ENDER[1]

[1]Chemical Engineering Department, University of Blumenau - FURB, Blumenau, SC, Brazil

[2]Chemistry Department, University of Blumenau - FURB, Blumenau, SC, Brazil

SCIENTIFIC PAPER

UDC 66.092-997:665.33

GREEN CHEMICAL PRODUCTION BASED ON THERMAL CRACKING OF INEDIBLE VEGETABLE OIL

Article Highlights

- Heptaldehyde, undecylenic acid and methyl undecenoate production from castor oil
- Different feed materials were tested to compare the yields of the desired products
- Methyl ester yields a higher concentration of heptaldehyde and methyl undecenoate

Abstract

This work evaluated the process for heptaldehyde, undecylenic acid, and methyl undecenoate production from castor oil, methyl ester of castor oil, and ricinoleic acid. Experiments were performed in a continuous pilot-plant scale pyrolysis reactor. Those are very important green chemical products that the thermal cracking of castor oil might produce. Transesterification of castor oil produces methyl ricinoleate, and its thermal cracking generates methyl undecenoate and heptaldehyde. The pyrolysis temperatures tested were 530 °C, 545 °C, 560 °C, and 575 °C, with residence time from 17 s to 32 s and mass flow at 400 g/h of the mixture of materials with 25% distilled water. It was observed that the temperature influenced the bio-oil yield in different degree for each material. The bio-oil was characterized by iodine index, acid number, and mass, and the contents of its compounds were obtained by GC-FID chromatography. The best result for the undecylenic acid mass yield of the desired compounds occurred at 530 °C, achieving 17.8% from ricinoleic acid and 16.5% from castor oil. For the heptaldehyde, the highest production was also obtained at 530 °C, with a value of 20.7% from methyl ester and 15.2% from ricinoleic acid.

Keywords: triglyceride pyrolysis, castor oil, ricinoleic acid, heptaldehyde, undecylenic acid, methyl undecenoate.

Heptaldehyde and undecylenic acid can be obtained by the thermal cracking of castor oil, its methyl ester, or ricinoleic acid [1,2]. They are among the most important green chemicals obtained from castor oil, known as vital intermediates for products within medicine, fuels, perfumes, polymers, plastics, rubbers, and flavors [3–5]. Ricinoleic acid, sebacic acid, and γ-decalactone are castor oil derivatives produced at a larger scale [6]. Castor bean (*Ricinus communis L.*) is an abundant oleaginous plant in tropical and subtropical regions. It has been cultivated mainly in India, China, Brazil, and Mozambique from 2007 to 2017 [7]. The castor bean seed has an oil percentage of 40% to 55% with approximately 90% of ricinoleic acid (12-hydroxy-9-cis-octodecenoic acid) in its composition [8]. Due to the presence of ricin, a toxic substance to humans, it is not used for food, thus making it inedible oil interesting for producing green chemicals. Other than that, its applications as a precursor of green chemicals are due to its molecule having three functional groups: double bound, hydroxyl, and carboxyl groups, increasing the possibilities of chemical reactions.

Correspondence: V. Botton, Chemical Engineering Department, University of Blumenau - FURB, Rua São Paulo 3250, Blumenau, SC, 89030-000, Brazil.
E-mail: vanderleiabotton@furb.br
Paper received: 14 January, 2022
Paper revised: 29 October, 2022
Paper accepted: 28 December, 2022

https://doi.org/10.2298/CICEQ220114033C

Das *et al*. [9] reported a process where the castor oil was thermally cracked in a stainless steel tubular vertical reactor 76.2 cm height by 2.5 cm internal diameter, filled with steel balls in the preheating section, 0.5% benzoyl peroxide was added as cracking initiator at 45 mmHg of pressure, with yields of 24.8% of heptaldehyde and 35.4% of undecylenic acid at 550 °C. The authors observed that castor oil, when cracked at lower temperatures, favored the occurrence of polymerization of the formed products, making it difficult to analyze their composition. It also hinders the formation of major products by reducing their yields and increasing secondary reactions in the form of acrolein, ketone compounds, and other fatty acids. Botton *et al*. [8] performed the thermal cracking of methyl esters in castor oil (65% of methyl ricinoleate) under steady-state and isothermal conditions in stainless steel auger reactor. They obtained yield values of 17.7% for heptaldehyde and 11.9% for methyl undecenoate with a mass flow of 280 g h^{-1} residence time of 44 s at 525 °C. It is important to say that thermal cracking of the methyl ester in castor oil has an intermediate compound, i.e., methyl undecenoate, which needs to be subsequently converted to the undecylenic acid by alkaline hydrolysis followed by acid hydrolysis [9,10]. As a contribution, this work proposed a simplified reaction mechanism, demonstrating one route for the desired products and another for the undesired products, such as methyl esters with 7 to 11 carbons in the chain, methanol, water, 1-decene, and 1,9-decadiene.

Some researchers have used water in thermal cracking reactions to obtain heptaldehyde, methyl undecenoate, and undecylenic acid, dealing with the performance increase of the process [11,12]. Wetroff *et al*. [11] described in USPTO 2807 633 the thermal cracking of castor oil, methyl ricinoleate, and ricinoleic acid in different conditions and reactor specifications for each material. They focused on the production of heptaldehyde and undecylenic acid with acrolein formation. At the same time, Guobin *et al*. [12] studied the kinetics of the thermal cracking reaction in the methyl ricinoleate and water mixture. According to the authors, the advantage of this route is that in the thermal cracking of methyl ricinoleate to obtain heptaldehyde and methyl undecenoate, it generates less harmful gases since no acrolein formation depends on the glycerol portion present in the triacylglycerol molecule, as well as the fact that viscosity of methyl ricinoleate is lower and easier to work with.

Recently, based on the work of Botton *et al*. [8] and samples of bio-oil produced by thermal cracking of methyl ester in castor oil under isothermal conditions (525 °C) and different residence times, Menshhein *et al*. [13,14] evaluated a process for separation and purification of heptaldehyde and methyl undecenoate with distillation as downstream operation, with an absolute characterization of the products using gas chromatography (GC). As a result, it was possible to concentrate the products in fractions with heptaldehyde and methyl undecenoate in atmospheric distillation. It is the first step for the technical viability and up-scaling of the thermal cracking of the inedible oil process for producing green chemicals.

Literature revision shows the same doubts about which raw material is better for producing a green chemical in terms of heptaldehyde and undecenoate acid (or methyl undecenoate) by thermal cracking. Thus, the main objective of the present work was to evaluate the continuous production of undecylenic acid, heptaldehyde, and methyl undecenoate from thermal cracking in a pilot-plant scale reactor of different materials (castor oil, methyl ester of castor oil, and ricinoleic acid) under different temperatures and residence times. Furthermore, the effects of the residence time and temperature on the product yields, the composition of the non-condensable gases, and the physical-chemical properties of the bio-oil produced, such as density and acid index, were considered.

MATERIALS AND METHODS

Materials

The materials used in experiments of thermal cracking were castor oil from Campestre Vegetable Oils (São Paulo/SP, Brazil), ricinoleic acid from A. Azevedo Oils Industry (São Paulo/SP, Brazil), while the methyl esters were obtained by methylic transesterification of castor oil (MECO) at 65 °C for 2h (FURB, Blumenau/SC, Brazil). The other reagents were obtained from Brazilian suppliers with the purity specifications recommended by the methods and used without any treatment. These materials were analyzed using gas chromatography (GC), whereas the bio-oil produced was analyzed according to standard methods such as density ASTM D4052, acidity index ASTM D664 and iodine index EN 14111.

Methyl ester production

Methyl ester of castor oil was obtained by homogeneous transesterification with the following conditions: reactions were carried out in a 3 L batch reactor; castor oil and methanol were used as reagents in 1:6 and 1:9 stoichiometric excess (i.e., castor oil to methanol) [15]; and with 1% (oil basis) potassium hydroxide (KOH) as a catalyst. The transesterification reaction started by adding methoxide (methanol with

potassium hydroxide) to castor oil at 65 °C, 120 rpm for 2 h. Samples were collected for gas chromatography to determine their esters contents according to European Standard EN 14103. In addition, esters obtained from different reactions were well mixed to form a standard sample for thermal cracking experiments.

Thermal cracking to bio-oil production

Thermal cracking experiments in a continuous pilot-plant scale reactor (Figure 1) to produce bio-oils were conducted using the same reactor with a cylindrical tube and an internal screw and operation procedure as described in Botton *et al.* [8,16]. For the three materials emulsified with 25% distilled water, the mass flow rate was 400 g/h at several temperatures of 530 °C, 545 °C, 560 °C, and 575 °C under steady and isothermal conditions. All the experiments were carried out in triplicate to confirm the reproducibility of the thermal cracking procedure.

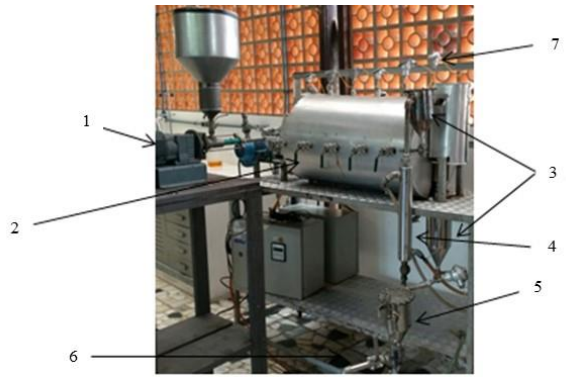

Figure 1. Reactor unit: 1 - Feeding, 2 - Reaction section, 3 - Expansion tanks, 4 - Condensing system, 5 - Flash: the collection of condensable gases occurs, 6 - Collection of non-condensable gases, 7 - Type "K" thermocouples, 8 - SCADA System (Supervisory Control and Data Acquisition).

The products yields (bio-oil and non-condensable gases) were calculated as follows: for the yield of bio-oil, it was considered the mass obtained at the end of the reactor divided by the mass fed; for the gas yield, the mass of the gas produced was divided by the mass of material fed into the reactor. Otherwise, the residence time was calculated as a function of the compositions of the bio-oil and non-condensable gas coupled with the thermal cracking temperature and pressure (atmosphere pressure), using the ideal gas model for density prediction and assuming a plug flow inside the reactor, following previous publications from the research group [8,17].

Gas chromatography analysis

The fatty acid content in the castor oil was esterified with methanolic sulfuric acid before submission to gas chromatography/mass spectrometry (Shimadzu GCMS-QP2010 Plus), according to Botton *et al.* [8]. The fatty acids were identified by comparison of the NIST 08 Mass Spectral Database.

Methyl ester content, obtained from methanolysis of castor oil, was determined using a GC- 7890B (Agilent, Santa Clara, EUA) equipped with flame ionization detector analysis (GC-FID) and Stabilwax capillary column according to Menshhein et al. [13,14] however with a split ratio of 1:50. The ester content (in mass percentage) was determined relative to the peak area of the internal standard (EN, 2003).

The non-condensable gas contents were determined by gas chromatography-flame ionization detection/thermal conductivity detection (GC-FID/TCD) using a Shimadzu GC-17A (Agilent, Santa Clara, EUA) according to Beims *et al.* [18]. The quantified components of non-condensable gases were CO, CO_2, methane, hydrogen and light hydrocarbons in the C_2–C_4 range.

Bio-oil samples obtained by thermal cracking of castor oil, ricinoleic acid and methyl esters were analyzed using the same GC-FID equipment with a split ratio of 1:200, according to Menshhein *et al.* [13,14]. The compounds were identified by comparison of their retention times with those of heptaldehyde, undecylenic acid, and methyl undecenoate standards (Sigma Aldrich). The color maps with yield information as a function of temperature and residence time for the different raw materials were constructed from numerical interpolation of experimental data.

RESULTS AND DISCUSSION

Composition of the feed materials

The fatty acid composition of castor oil obtained by GC-MS was 89.72%, 5.12%, 3.86%, 0.88%, and 0.42% for ricinoleic, oleic, linoleic, stearic and palmitic acid, respectively. This result confirms the major presence of ricinoleic acid in castor oil samples, as described in the literature [19,20], between 85% and 95%. Furthermore, in the GC analysis of the methyl esters samples, the final ester content was 80.14% with 66.8% of methyl ricinoleate, confirming its predominance in the mixture.

Thermal cracking experiments

The experiments were carried out in a pilot plant at four temperatures with the residence times ranging from 17 s to 32 s, approximately, under the continuous mode of operation, at steady-state and isothermal conditions, as shown in Table 1. Bio-oil yields from the castor oil, ricinoleic acid and methyl ester decrease from 84%, 81% and 81% to 57%, 48% and 70%, as a function of the temperature increase from 530 °C to

575 °C, respectively. When lower temperatures were used, castor oil presented the highest bio-oil yields, 530 °C (84%) and 545 °C (78%). On the other hand, with higher temperatures, methyl ester showed the highest bio-oil yields, for instance, at 560 °C (72%) and at 575 °C (70%). This fact might be related to the reaction activation energy, once methyl ricinoleate has a value of 172.9 kJ/mol [12], whereas castor oil has a reaction activation energy of 51 kJ/mol [21]. So, a lower reaction activation energy is expected to lead to a higher number of cracking reactions, forming more components with short chains and leading to a higher gas phase yield. In the study of Ganesan *et al*. [20], the catalytic cracking of castor oil was performed at 400 °C using a catalyst (AlMCM-41), and the liquid yield obtained was also around 85%. On the other hand, Nazarudin *et al*. [22–24] performed the catalytic cracking at 450 °C of used cooking oil and methyl esters of cooking oil, giving liquid yields of 35.6% and 38.85%, respectively, showing a lower yield of gas phase for methyl esters.

Table 1. Mass balance and residence time from thermal cracking products.

Run	T (°C)	Feed material	Residence time (s)	Yields (%)	
				Non-condensable gas	Bio-oil
1		Castor oil	28.74±1.07	12.6±1.2	83.9±3.6
2	530	Ricinoleic acid	26.63±3.18	12.8±0.4	81.4±9.7
3		MECO	32.09±4.15	11.5±2.3	81.7±9.9
4		Castor oil	26.73±1.83	15.3±1.4	78.1±6.0
5	545	Ricinoleic acid	23.98±3.70	17.6±0.4	73.1±13.3
6		MECO	30.17±3.51	12.8±1.7	76.9±8.6
7		Castor oil	23.41±1.35	19.9±1.8	68.7±3.9
8	560	Ricinoleic acid	21.52±1.40	20.3±0.6	66.2±4.6
9		MECO	28.26±3.56	20.9±2.6	72.1±9.2
10		Castor oil	20.30±1.91	30.1±5.6	57.3±6.5
11	575	Ricinoleic acid	17.12±4.8	34.6±2.8	48.4±17.9
12		MECO	27.10±2.73	23.8±2.4	70.0±8.0

Results of Table 1 also show that residence time decreases as temperature increases. This behavior was observed for the three materials, but ricinoleic acid had the shortest residence time for all the evaluated temperatures, and the methyl ester had the longest. It is because methyl ester produces fewer gases than ricinoleic acid and castor oil, reducing its velocity inside the reactor.

Figure 2 presents the samples' volumetric percentages of the gases (CO_2, H_2, CH_4, CO, and C_2–C_4). The presence of CO and CO_2 is observed, confirming decarbonylation (CO release) and decarboxylation (CO_2 release) reactions. CO is produced in a higher concentration than CO_2 in the thermal cracking of methyl esters. It can be explained by the fact that thermal cracking promotes the breakdown of triacylglycerol into free fatty acid and glycerol, which decomposes into acrolein, and the decomposition of acrolein generates CO. This behavior was shown to be similar for castor oil and ricinoleic acid, with lower CO contents due to the absence of glycerol and acrolein. For castor oil, the average was 33.65% CO and for ricinoleic acid, 22.6%. The formation of methane (CH_4) and H_2 was also observed, and the difference grouped in larger volumes of C_2–C_4 compounds, characterizing the intensifications of secondary reactions in the thermal cracking.

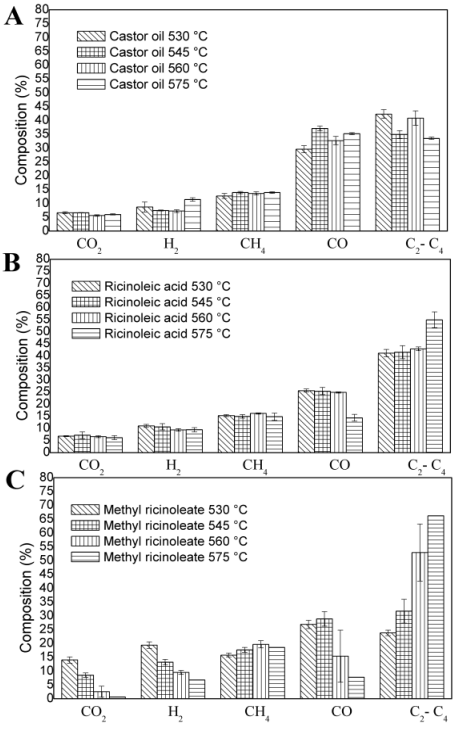

Figure 2. Composition of the non-condensable gases generated for (a) castor oil, (b) ricinoleic acid, and (c) methyl ricinoleate.

The variation in the density of the liquid products (Figure 3A) was obtained using a pycnometer. It was observed that there was a slight reduction in density as a function of temperature in all experiments. This density drop is due to reactions that divide the larger chains into smaller chains, creating products with smaller molar masses.

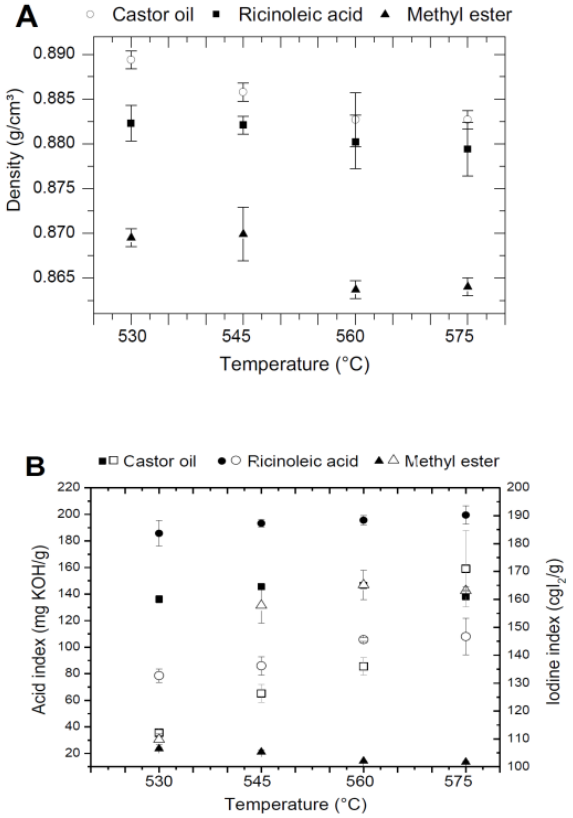

Figure 3. Values of (a) density, (b) acid index (■, ● and ▲), and iodine index (□, ○ and Δ) for castor oil bio-oils, ricinoleic acid, and MECO after thermal cracking at 530, 545, 560 and 575 °C.

The acidity indexes in Figure 3B for the bio-oils increased in relation to the index of each corresponding feed material. The acidity of the bio-oil of castor oil presents a slight increase at 545 °C and then stabilizes. The increase in the acidity index for the bio-oil of castor oil and the bio-oil of ricinoleic acid is because the increase in temperature promotes a higher formation of short-chain carboxylic acids in the secondary reactions. For the ricinoleic acid bio-oil, there was a change as a function of the increase in temperature, with a slight increase from 185.7 mg KOH/g (530 °C) to 199.5 mg KOH/g (580 °C). The decrease in the acidity index of methyl ricinoleate in higher temperatures is related to the higher formation of esters, promoting a reduction in the values starting at 530 °C with 23.6 (mg KOH/g) and ending with 13.5 (mg KOH/g) at 575 °C. For the castor oil bio-oil, the iodine index gradually increases with the temperature, going up from 110 cg I_2/g to 171.0 cg I_2/g with a cracking temperature of 575 °C. It shows that for this temperature, an increase occurs in the breaking reactions forming more unsaturated compounds for the castor oil bio-oil. For the bio-oil of ricinoleic acid, the increase was also gradual for all temperatures, with a higher value of 146.7 cg I_2/g. For the bio-oil of methyl ricinoleate, its greatest variation was from 109.8 at 530 °C to 165.2 cg I_2/g at 560 °C, showing a higher intensity of cracking reactions at higher temperatures.

Green chemical production

All the results of the chromatograms are compared through software (GCM Solution) with its data and compound library (NIST). This software presents a probability of the compounds' identity based on the chromatographic column's retention times and their mass spectra. In the castor bean bio-oil chromatogram (Figure 4A), the volumetric percentage of heptaldehyde and undecylenic acid was determined, with a retention time of 7.97 min for heptaldehyde and 34.8 min for undecylenic acid, respectively. These are the components of higher concentration and targets of this investigation. However, the other compounds had smaller peaks, which make up the total volumetric percentage. Figure 4B and Figure 4C show the chromatograms of the bio-oils obtained at 530 °C of ricinoleic acid and methyl ricinoleate, respectively. The first shows the presence of heptaldehyde, methyl undecenoate, and undecylenic acid from the unconverted triglyceride portion in the esterification. The percentages were obtained by comparison with the methyl undecenoate, heptaldehyde, and undecylenic acid standards.

The final values of the yields of the green chemical produced are given in Table 2. For castor oil, the best yield of the heptaldehyde and undecylenic acid mass yields occurred at 530 °C with 19.03% and 16.5%, respectively. The yield values for ricinoleic acid were 530 °C for both heptaldehyde and ricinoleic acid, with results of 15.2% and 17.8%, respectively.

Methyl ricinoleate obtained its best mass percentage result for heptaldehyde at 530 °C and methyl undecenoate at 560 °C with 20.7% and 23.8%, respectively. Based on these results, the best result for producing heptaldehyde was 20.7% of mass yield at 530 °C, with the methyl ricinoleate material. The best result for the production of undecylenic acid occurred with the thermal cracking of ricinoleic acid, with its mass yield occurring at 530 °C, with a value of 17.8%. For the production of methyl undecenoate, the best temperature was 560 °C, with a mass value of 23.8.

The yield of desirable products was calculated considering the bio-oil yield. The response surface plots are presented in Figure 5 and Figure 6, with

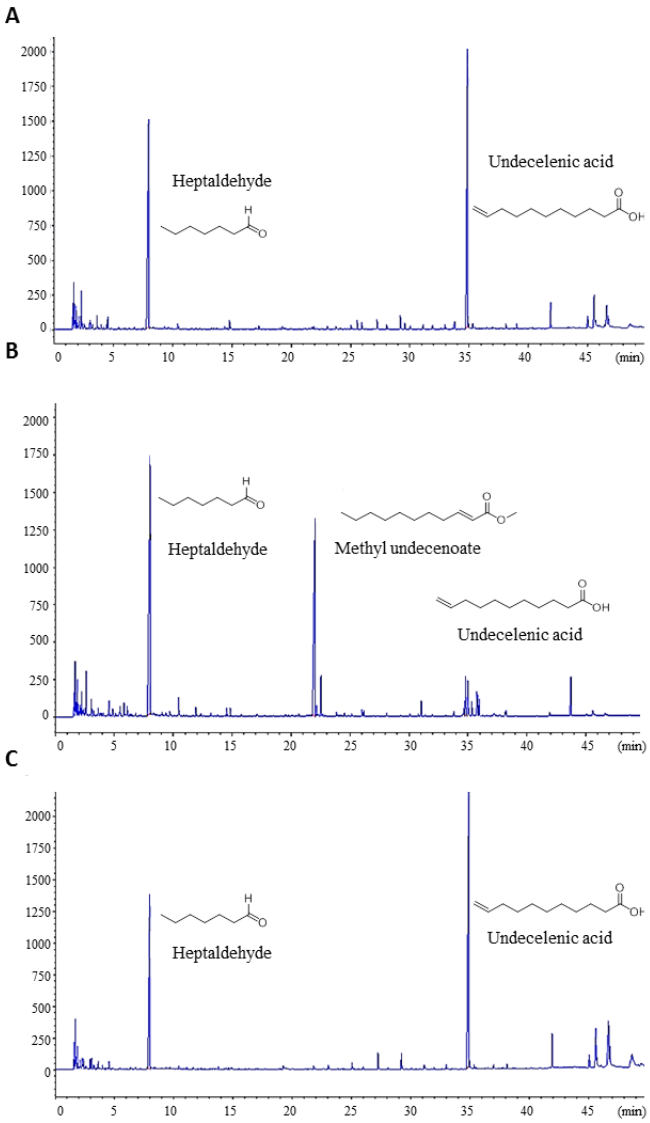

Figure 4. Chromatogram of bio-oil from thermal cracking with 25% of water at 530 °C of (a) castor oil, (b) MECO, and (c) ricinoleic acid.

Table 2. Mass yields of the green chemicals produced - heptaldehyde, undecylenic acid, and methyl undecenoate.

T (°C)	Feed material	Heptaldehyde (%)	Undecylenic acid (%)	Methyl undecenoate (%)
529.7±0.8	Castor oil	9.3±1.4	16.5±1.6	ND*
544.7±0.6		7.9±1.6	15.6±1.6	ND
559.6±1.1		5.1±1.0	13.1±0.8	ND
574.2±0.9		2.3±1.4	10.1±1.4	ND
528.9±2.2	Ricinoleic acid	5.2±1.8	17.8±2.7	ND
544.8±4.5		3.8±2.2	15.7±2.8	ND
557.2±4.4		2.5±0.7	14.4±0.3	ND
580.2±8.3		.5±3.2	9.2±3.4	ND
529.7±0.8	Methyl ester	0.7±3.7	0.8±0.3	20.9±6.1
544.7±0.6		9.7±2.2	1.0±0.3	22.4±3.9
559.6±1.1		8.8±2.1	0.9±0.2	23.8±4.5
574.2±0.9		7.0±2.3	0.8±0.1	23.4±3.5

products yield surface plots as a function of residence time and temperature. Response surfaces were obtained using experimental data, and this analysis provides a possibility of scientific visualization of the entire experimental set in a single color map. The contour plots depict that heptaldehyde behavior was similar for all three materials (Figure 4). The highest yield was achieved at the maximum values of residence time and lower temperatures. Undecylenic acid (Figure 6b) from castor oil and ricinoleic acid also presented this behavior. However, the best conditions for the undecylenic acid from MECO were intermediate temperature and residence time conditions.

If considering that 1 mol of methyl undecenoate generates 1 mol of undecylenic acid, it was possible to relate the methyl undecenoate yield with its acid and thus to compare the results with a base calculation of 1000 g of crude oil with 1000 g of castor oil yield ± 873 g of methyl ricinoleate. With these comparisons, it is clear that the cracking of methyl ricinoleate presented the highest value for producing heptaldehyde when considering the deviation. It was also the one that produced the most undecylenic acid. However, these results show that the yields of desirable products remain lower than expected for commercial-scale production using only the thermal cracking process. In fact, this suggests the use of a catalyst for increasing the selectivity of the cracking in heptaldehyde and undecylenic acid for future investigations.

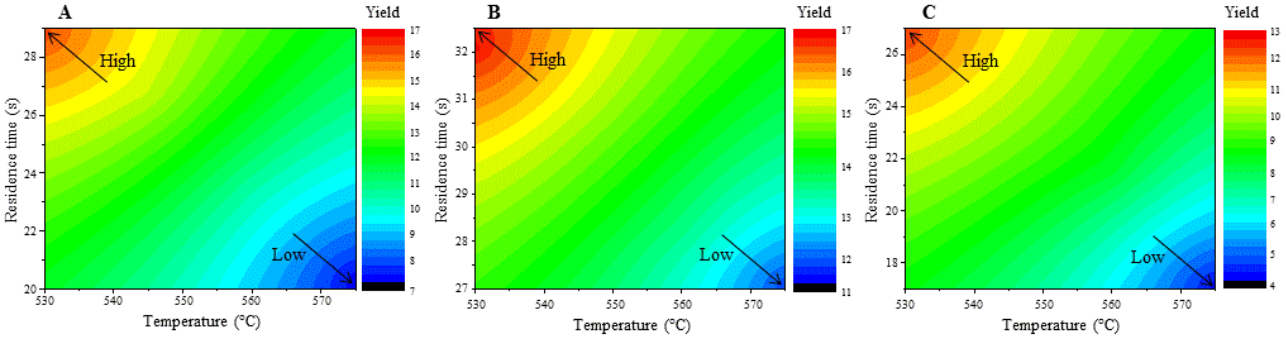

Figure 5. Response surface of heptaldehyde yield from (a) castor oil, (b) MECO, and (c) ricinoleic acid.

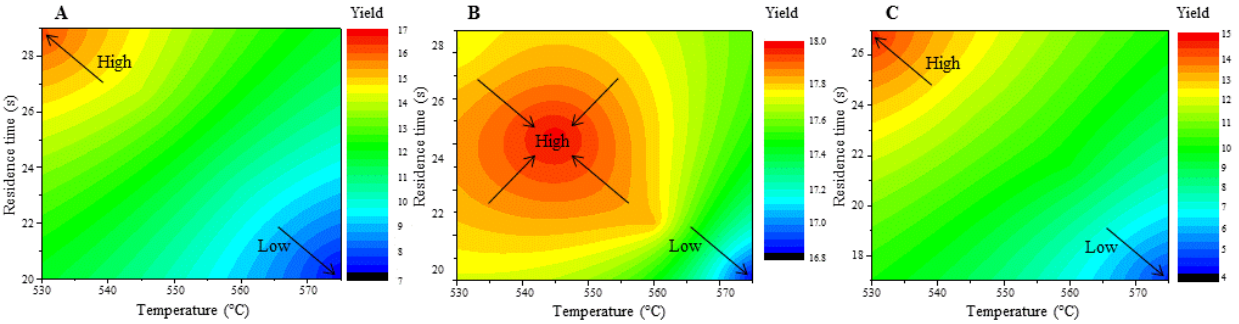

Figure 6. Response surface yield: (a) undecylenic acid yield from castor oil, (b) undecylenic acid and methyl undecenoate from MECO, and (c) undecylenic acid yield from ricinoleic acid.

CONCLUSION

Among the conditions proposed in this work, the best condition for the production of heptaldehyde and undecylenic acid occurred with the thermal cracking of methyl ricinoleate at 530 °C and 560 °C, respectively. While the best mass yield value for heptaldehyde was 20.7%, and the best mass yield value for undecylenic acid (as ester) was 23.8%.

Compared to the yields of castor oil and ricinoleic acid, the production of heptaldehyde was favorable for using castor oil and more favorable for ricinoleic acid in the production of undecylenic acid. It was possible to see the presence of the formation of glycerol and acrolein by its decomposition through the difference in the generated volume of carbon monoxide, which was higher for castor oil. The thermal cracking of methyl ricinoleate presents a smaller volume of secondary reactions in relation to castor oil and ricinoleic acid, yet this fact needs further evaluation. On the other hand,

the use of catalysts to make the process more attractive for commercial production appears like a good opportunity for future work.

ACKNOWLEDGEMENT

The authors are grateful to the University of Blumenau (FURB) and the Chemical Engineering Department of FURB. This study was financed in part by the Coordenação de Aperfeiçoamento de Pessoal de Nível Superior e Brasil (CAPES) Finance Code 001.

REFERENCES

[1] H. Mutlu, M.A.R. MeierEur. J. Lipid Sci. Technol. 112 (2010) 10–30. http://dx.doi.org/10.1002/ejlt.200900138.

[2] X. Mao, Q. Xie, Y. Duan, S. Yu, Y. Nie, Appl. Therm. Eng. 194 (2021) 117093. http://dx.doi.org/10.3390/ma15041565.

[3] E.B. Mubofu, Sustain. Chem. Process. 4 (2016). https://doi.org/10.1186/s40508-016-0055-8.

[4] M. Van der Steen, C.V. Stevens, ChemSusChem. 2, (2009) 692–713. https://doi.org/10.1002/cssc.200900075.

[5] W.J. Kh'ng, W.A. Ibrahim, Z. Hassan, I. Izirwan, Energy Reports. 8, (2022) 11–18. https://doi.org/10.1016/j.egyr.2022.10.111.

[6] S. Singh, S. Sharma, S.J Sarma, S.K. Brar, Environ. Prog. Sustain. Energy. 42 (2022) E14008. https://doi.org/10.1002/ep.14008.

[7] FAOSTAT Statistical Database (2019), Food and Agriculture Organization of the United Nations, http://www.fao.org/faostat/en/#compare [accessed 7 December 2021.

[8] V. Botton, R. Torres De Souza, V.R. Wiggers, D.R. Scharf, E.L. Simionatto, L. Ender, H.F. Meier, J. Anal. Appl. Pyrolysis 121 (2016) 387–393. http://dx.doi.org/10.1016/j.jaap.2016.09.002.

[9] G. Das, R.K. Trivedi, JAOCS 66 (1989) 938–941. https://doi.org/10.1007/BF02682613.

[10] C. Tang, Z. Yuan, Catalytic cracking method for preparing 10-undecenoic acid and heptaldehyde - PCT CN103819330 (2014).

[11] G. Wetroff, L. Thillay, G. Divachetf, J. Khaladji, Pyrolysis of Ricinoleates - PCT US2807633 (1957).

[12] H. Guobin, L. Zuyu, Y. Suling, Y. Rufeng, JAOCS 73 (1996) 1109–1112. https://doi.org/10.1007/BF02523370.

[13] G. Menshhein, V. Costa, L.M. Chiarello, D.R. Scharf, E.L. Simionato, V. Botton, H.F. Meier, V.R. Wiggers, L. Ender, Renew. Energy 142 (2019) 561–568. https://doi.org/10.1016/j.renene.2019.04.136.

[14] G. Menshhein, V. Costa, L.M. Chiarello, D.R. Scharf, E.L. Simionato, V. Botton, H.F. Meier, V.R. Wiggers, L. Ender, Data Br. 25 (2019) 104325. https://doi.org/10.1016/j.dib.2019.104325.

[15] K. Ramezani, S. Rowshanzamir, M.H. Eikani, Energy 35 (2010) 4142–4148. https://doi.org/10.1016/j.energy.2010.06.034.

[16] V. Botton, D.R. Riva, E.L. Simionatto, V.R. Wiggers, L. Ender, H.F. Meier, A.A.C. Barros, Quim. Nova 35 (2012) 677–682. https://doi.org/10.1590/S0100-40422012000400004.

[17] H.F. Meier, V.R. Wiggers, G.R. Zonta, D.R. Scharf, E.L. Simionatto, L. Ender, Fuel 144 (2015) 50–59. https://doi.org/10.1016/j.fuel.2014.12.020.

[18] R.F. Beims, V. Botton, L. Ender, D.R. Scharf, E.L. Simionatto, H.F. Meier, V.R. Wiggers, Fuel 217 (2018) 175–184. https://doi.org/10.1016/j.fuel.2017.12.109.

[19] D.P. Matharasi, G. Ramya, A. Asha, P. Jayaprakash. J. Indian Chem. Soc. 99, (2022) 100757. https://doi.org/10.1016/j.jics.2022.100757.

[20] R. Ganesan, S. Subramaniam, R. Paramasivam, J.S.M. Sabir, J.S. Femilda Josephin, K. Brindhadevi, A. Pugazhendhi, Sci. Total Environ. 757 (2021) 143781. https://doi.org/10.1016/j.scitotenv.2020.143781.

[21] C.A. Canciam, E-xacta 4 (2011) 7–18. http://dx.doi.org/10.18674/exacta.v4i3.667.

[22] I.G. Prabasari, R. Sarip, S. Rahmayani, N. Nazarudin, Makara J. Sci. 23 (2019) 162–168. https://doi.org/10.7454/mss.v23i3.11264.

[23] N. Nazarudin, U. Ulyarti, O. Alfernando, Y.Y. Hans, Reaktor. 22, (2022) 21–27. https://doi.org/10.14710/reaktor.22.1.21-27.

[24] N. Nazarudin, I.G. Prabasari, U. Ulyarti, Susilawati, A. Oktadio, J. Phys. Conf. Ser. 1567 (2020) 022021. https://doi.org/10.1088/1742-6596/1567/2/022021.

VANDERLEI RODRIGUES COSTA[1]
LUANA MARCELE CHIARELLO[1]
VANDERLEIA BOTTON[1]
EDÉSIO LUIZ SIMIONATTO[2]
VINICYUS RODOLFO WIGGERS[1]
HENRY FRANÇA MEIER[1]
LAÉRCIO ENDER[1]

[1]Chemical Engineering Department, University of Blumenau - FURB, Blumenau, SC, Brazil

[2]Chemistry Department, University of Blumenau - FURB, Blumenau, SC, Brazil

NAUČNI RAD

ZELENA HEMIJSKA PROIZVODNJA ZASNOVANA NA TERMIČKOM KREKOVANJU NEJESTIVOG BILJNOG ULJA

Ovaj rad procenjuje proces proizvodnje heptaldehida, undekilenske kiseline i metil undecenoata iz ricinusovog ulja, metil estra ricinusovog ulja i ricinoleinske kiseline. Eksperimenti su izvedeni u kontinualnom poluindustrijskom pirolitičkom reaktoru. Termičkim krekovanjem ricinusovog ulja dobijeni su veoma važni zeleni hemijski proizvodi. Transesterifikacija ricinusovog ulja proizvodi metil ricinoleat, a njegovo termičko krekovanje stvara metil undekenoat i heptaldehid. Ispitivanje pirolize izvršeno je na 530 °C, 545 °C, 560 °C i 575 °C, sa vremenom zadržavanja od 17 s do 32 s i masenim protokom pri 400 g/h mešavine materijala sa 25% destilovane vode. Uočen je uticaj temperature i vrste polazne sirovina na proizvedeno bio-ulje. Bio-ulje je okarakterisano jodnim i kiselinskim brojem i masom, a sastav je određen GC-FID hromatografijom. Najbolji rezultat za maseni prinos undekilenske kiseline postignut je na 530 °C, i to 17,8% od ricinolne kiseline i 16,5% od ricinusovog ulja. Za heptaldehid je, takođe, najveća proizvodnja dobijena na 530 °C, sa vrednošću od 20,7% od metil estra i 15,2% od ricinolne kiseline.

Ključne reči: piroliza triglicerida, ricinusovo ulje, ricinolna kiselina, heptaldehid, undekilenska kiselina, metil undekenoat.

CI&CEQ
Chemical Industry & Chemical Engineering Quarterly

Available online at
Association of the Chemical Engineers of Serbia AChE
www.ache.org.rs/CICEQ

Chem. Ind. Chem. Eng. Q. 29 (4) 273–280 (2023) CI&CEQ

LV CHAO[1,3]
YIN HONGXIN[1]
LIU YANLONG[1]
CHEN XUXIN[1]
SUN MINGHE[1]
ZHAO HONGLIANG[2]

[1]School of Control Engineering, Northeastern University, Hebei, China

[2]School of Metallurgy and Ecological Engineering, University of Science and Technology Beijing, Beijing, China

[3]State Key Laboratory of Complex Nonferrous Metal Resources Clean Utilization, Kunming University of Science and Technology,Yunnan, China

SCIENTIFIC PAPER

UDC 66.092-997:54:519.87

PROCESS STUDY OF CeO_2 PREPARATION BY JET-FLOW PYROLYSIS VIA MICROWAVE HEATING

Article Highlights

- Cerium oxide with high purity was produced via microwave heating
- The effect of gas and material velocity on purity was studied by experiment and numerical simulation
- Single-phase cerium oxide with sphere-like morphology was obtained in this study

Abstract

The spray pyrolysis method has the disadvantage of nozzle plugging, and the conventional heating model causes a large temperature gradient, which leads to unevenly heated reactants. This study used cerium chloride heptahydrate and Venturi reactor as raw material and core equipment. The technology of microwave heating was combined to prepare single-phase sphere-like cerium oxide. The mean size of the particles was near 80nm. The product was characterized via XRD, SEM, and EDS technologies. The purity, morphology, and energy consumption were compared with the conventional spray pyrolysis. Fluent software coupled with HFSS was employed to simulate the effects of different process conditions on products' purity and temperature field in the reactor. There was good correspondence between experimental and simulated results. The results showed that as gas velocity V_g increased, the tendency of the temperature field distribution did not change. The lowest mass fraction of chlorine element reached 0.13% when the gas inlet velocity reached 1.7 m/s. When the material inlet velocity was 0.05 m/s, the mass fraction of the chlorine element was below 0.1%, which indicated that the reactants had a complete reaction. It has been calculated that the heating cost, energy consumption, and CO_2 emission decreased sharply compared with the spray pyrolysis method.

Keywords: cerium oxide, economic benefit, microwave heating, numerical simulation.

Cerium oxide (CeO_2) is the most common composition of rare earth metals with superior characteristics, including high activity, hardness, and stability. Considering the relatively low mining costs of CeO_2, it has been widely applied in numerous fields, such as catalyst, medicine, and abrasive compounds with special physical and chemical properties [1–4].

Studies show that the size and morphology of CeO_2 particles directly affect their physical and chemical properties. In this regard, scholars have utilized different methods, including precipitation [5], gel-sol [6], and pyrolysis, to prepare CeO_2 powder at micro-nano levels. Among these methods, the pyrolysis method has many advantages, like lower cost and higher efficiency. However, it also has the disadvantage of nozzle plugging, which causes frequent replacement, and the experiment cannot be continuously carried out. The roasted products always agglomerated and had varying particle sizes. Aiming at this problem, a method of jet-flow pyrolysis via microwave heating, a new preparation technology of

Correspondence: L. Chao, School of Control Engineering, Northeastern University, Hebei 066004, China.
E-mail: lvchao@neuq.edu.cn
Paper received: 10 May, 2022
Paper revised: 28 November, 2022
Paper accepted: 28 December, 2022

https://doi.org/10.2298/CICEQ220510034C

CeO_2, was developed by our team. This technology has many advantages. For example, the jet effect of the Venturi reactor has been demonstrated to produce an atomization effect on droplets, which perfectly avoided the functional defects of the nozzle [7].

Microwaves are electromagnetic waves with frequencies between 300 MHz and 300 GHz. Based on the penetration characteristic of microwaves, the molecule orientation in the heated object changes with the variation of the microwave field, thereby colliding with nearby molecules and generating heat [8–9]. Microwave heating has the advantages of fast and even heating, which can eliminate the temperature gradient in the reaction system and restrain the products' agglomeration [10–12]. Accordingly, regular morphology and small particle size will be obtained. Due to the opaque equipment, numerical simulation has become an efficient tool to predict and visualize the thermal response of materials subjected to microwave heating [13]. Researchers have conducted numerical simulations to study the interphase transfer process under the microwave field and analyze microwave pyrolysis. Salvi *et al*. [14] simulated the multiphase flow trans-mission and studied the interaction between microwave and fluid by solving Maxwell and heat conduction equations. Then, the effect of temperature distribution and physical properties of the fluid on microwave heating was investigated. Si *et al*. [15] simulated the drying characteristics of lignite in a microwave-fluidized bed based on the Euler model and qualitatively analyzed the heat transfer coefficient, microwave power, and relationship between the gas phase temperature and the gas velocity. In this study, the experiment and simulation were both investigated. It was intended to establish the coupling model of microwave heating, fluid flow, and chemical reaction. Effects of gas and material inlet velocity on temperature field and CeO_2 purity were studied. The heating cost, energy consumption, and CO_2 emission were calculated.

In this study, microwave heating and jet technology are combined to achieve a green and environment-friendly rare earth oxide preparation process with a simple process flow, which aligns with the current low-carbon production concept. At the same time, we use numerical simulation to visually analyze the physical field in the experiment, which provides more reasonable data support for the optimization of the experimental scheme in the future.

MATERIALS AND METHODS

Experiments

The experimental process scheme is shown in Figure 1. Venturi reactor made of quartz was fastened to the center of the microwave oven (Independent design, Shan-Lang Experimental Material Management Department, China). The air compressor (2.0 kW, Jiangsu Dongcheng M&E Tools Co., Ltd, China) provided oxygen for the chemical reaction. The glass rotameter (LZB-15, 1–10 m^3/h, Xiangjin Hardware&Electrical Appliance Co., Ltd) was used to measure the gas velocity generated by the air compressor. The steam generator (LDR3-04, Dongyang Jiaxian Machinery Manufacturing Co., Ltd, China) was used to preheat and provide water vapor for the chemical reaction. Cerium chloride heptahydrate ($CeCl_3 \cdot 7H_2O$, 99%, analytical grade, Sinopharm Chemical Reagent Co., Ltd, China) was the raw material and entered the Venturi reactor from the vertical material inlet. Driven by the gas, the materials were pushed into the reactor to react with oxygen. The solid product of the reaction fell into the solid-product collector. In the industrial production process of the pyrolysis method, hydrogen chloride (HCl) was used to dissolve rare earth ore or recycle it in the extraction process. However, there were no conditions for HCl recovery in the laboratory. Therefore, the gas produced by the reaction was absorbed by the sodium carbonate (Na_2CO_3, 99.8%, AR, Sinopharm Chemical Reagent Co., Ltd, China) solution.

The phase composition of the products was determined using X-ray diffraction (XRD, Empyrean S3, PANalytical) at a scanning rate of 5°/min in the 2θ range from 10° to 90° with Cu K_α radiation (λ=1.540598 nm).

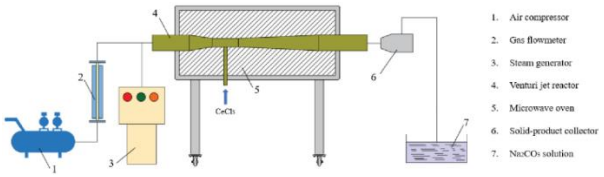

Figure 1. Scheme diagram of the experimental process.

Numerical simulation

The whole numerical simulation was based on the Workbench 19.0 platform. HFSS software was used for the electromagnetic simulation. Fluent software was used to simulate the fluid field and chemical reactions. The two parts were connected using an interface. During numerical simulation, enthalpy, entropy, and other necessities were determined from Practical Inorganic Thermodynamics Data Manual [16].

Geometry

Based on the experimental equipment, the three-dimensional model was simplified and built, as shown in Figure 2. Table 1 presented the sizes of the microwave oven and reactor. The model of the

waveguide was BJ26. The grid of the model consisted of three-dimensional tetrahedral unstructured meshes. In addition, a local coordinate system and an influence sphere were created at the Venturi tube to conduct local encryption on the grid, and the total number of grids reached 370 k.

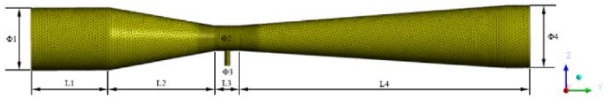

Figure 2. Schematic diagram of Venturi reactor.

Table 1. Mass balance and residence time from thermal cracking products.

	Length (mm)	Width (mm)	Height (mm)	Diameter (mm)
Cavity	690	400	600	-
Waveguide	86.4	43.2	60	-
L1	-	-	100	-
L2	-	-	136	-
L3	-	-	343	-
L4	-	-	30	-
Φ1	-	-	-	30
Φ2	-	-	-	15
Φ3	-	-	-	7
Φ4	-	-	-	30

Four monitoring surfaces were set between the Venturi tube and outlet to study the reactor's temperature field and the content of each substance at each position. The distance between these surfaces and the gas phase inlet was Y_1 = 290 mm, Y_2 = 390 mm, Y_3 = 490 mm, and Y_4 = 590 mm, respectively.

Governing equations

The electromagnetic field distribution of the cavity in the microwave oven, including the reactor, can be determined by solving the Maxwell equation. The time-varying form of the Maxwell equation can be expressed in the form below:

$$\nabla \cdot \boldsymbol{D} = \rho_e \tag{1}$$

$$\nabla \cdot \boldsymbol{B} = 0 \tag{2}$$

$$\nabla \times \boldsymbol{E} = -\frac{\partial \boldsymbol{B}}{\partial t} \tag{3}$$

$$\nabla \times \boldsymbol{H} = -\frac{\partial \boldsymbol{D}}{\partial t} + \boldsymbol{J} \tag{4}$$

where B is the magnetic flux density (Wb/m^3), D is the electric displacement or electric flux density (C/m^2), E is the electric field intensity (V/m), H is the magnetic field intensity (A/m), J is the current density (A/m^2), and ρ_e is the electric charge density (C/m^3).

The complex relative permittivity ε_r is defined as:

$$\varepsilon_r = \varepsilon' + j\varepsilon'' \tag{5}$$

where $j^2 = -1$, ε' is the dielectric constant, and ε'' is the corresponding loss factor (the imaginary part of the dielectric constant). ε' represents the ability of microwaves to penetrate the material, while ε'' represents the ability of the material to store electricity.

The differential wave equation deduced using Maxwell's equations describes the electromagnetic field distribution:

$$\nabla \times \mu_r^{-1}(\nabla \times \boldsymbol{E}) - k_0^2\left(\varepsilon_r - \frac{j\sigma}{\omega\varepsilon_0}\right)\boldsymbol{E} = 0 \tag{6}$$

$$k_0 = \omega / c_0 \tag{7}$$

where ω is the angular frequency (rad/s), ε_0 is the free space permittivity (8.85×10^{-12} F/m), μ_r is the relative permeability, σ represents the electrical conductivity (S/m), k_0 is the wave number in free space, and c_0 represents the speed of light in vacuum (m/s).

When the electromagnetic field interacts with the solution, part of the electromagnetic energy transforms into thermal energy, which is the source item of the energy equation. The energy absorbed by the per unit volume solution can be expressed using the following equation:

$$Q = \frac{1}{2}\omega\varepsilon_0\varepsilon''|\boldsymbol{E}|^2 \tag{8}$$

where $|E|$ is the electric field modulus.

In the reactor, every relative species needs to observe the species mass-conservation equation:

$$\frac{\partial(\rho Y_i)}{\partial t} + \nabla \cdot (\rho \boldsymbol{v} Y_i) = -\nabla \boldsymbol{J}_i + R_i + S_i \tag{9}$$

where Y_i is the mass fraction of the i^{th} substance, R_i is the net production rate of the chemical reaction of the i^{th} substance, S_i is the discrete phase of the i^{th} substance that is responsible for the additional production rate caused by the user-defined source item, and J_i is the diffusive flux of the i^{th} substance produced by the concentration gradient.

The reaction in the Venturi jet pyrolysis reactor is:

$$4CeCl_3(s) + 6H_2O(g) + O_2(g) = 4CeO_2(s) + 12HCl(g) \tag{10}$$

Boundary conditions

The specific boundary conditions are shown in Table 2. The microwave power (P) and frequency (f) were set to 1 kW and 2.45 GHz, respectively. Although there were differences between the real case and the numerical model, the numerical simulation could reveal the effects of experimental factors. Some assumptions were made before the simulation to decrease the difficulty of the simulation and raise its efficiency:

1) The frequency of the microwave is constant at 2.45 GHz.
2) All the fluids in this study are considered incompressible fluids.
3) The initial temperature field is uniform at 300 K (room temperature).

Table 2. Boundary conditions.

	Boundary type	Valve
Excitation	Wave port	-
Wall of waveguides and cavity	Perfect E boundary	-
Gas inlet	Velocity-inlet	1.7 m/s
Material inlet	Velocity-inlet	0.01 m/s
Outlet	Outflow	-

RESULTS AND DISCUSSION

Comparison of experimental results

The XRD pattern of the product is shown in Figure 3. It showed a single phase CeO_2 obtained at the temperature of 901 K. Compared with the spray pyrolysis method at the temperature of 1023 K [17], the intensity of the diffraction peaks was higher. No other impurity peak indicated a better degree of crystallinity and a higher purity of CeO_2. Scanning electron microscope (SEM, Apreo 2C, Thermo scientific) images of nano CeO_2 particles obtained in this study are shown in Figure 4a. Compared with the SEM images of spray pyrolysis shown in Figure 4b, the particles were sphere-like and smaller, so there was less agglomeration. The above indicated that microwave heating could produce purer CeO_2 with more regular morphology at a lower temperature.

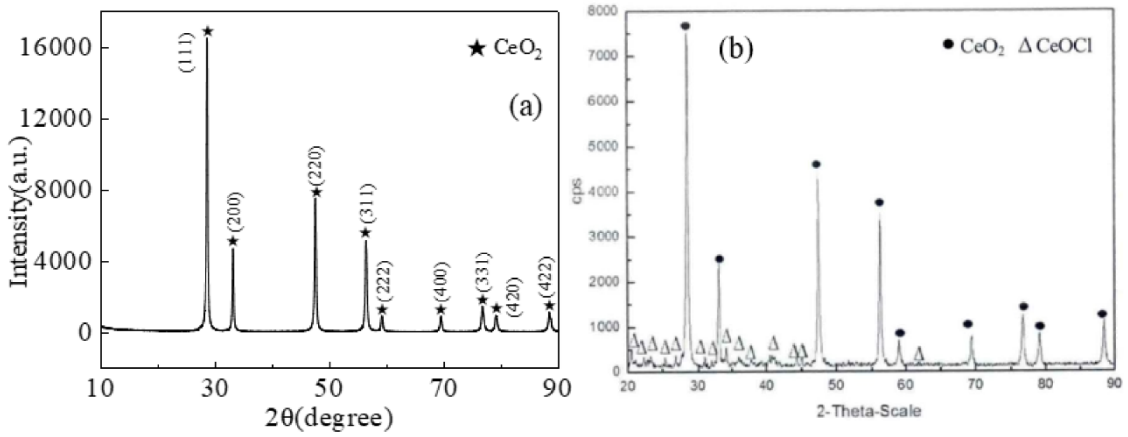

Figure 3. XRD pattern of the product: (a)-this study; and (b)- spray pyrolysis [17].

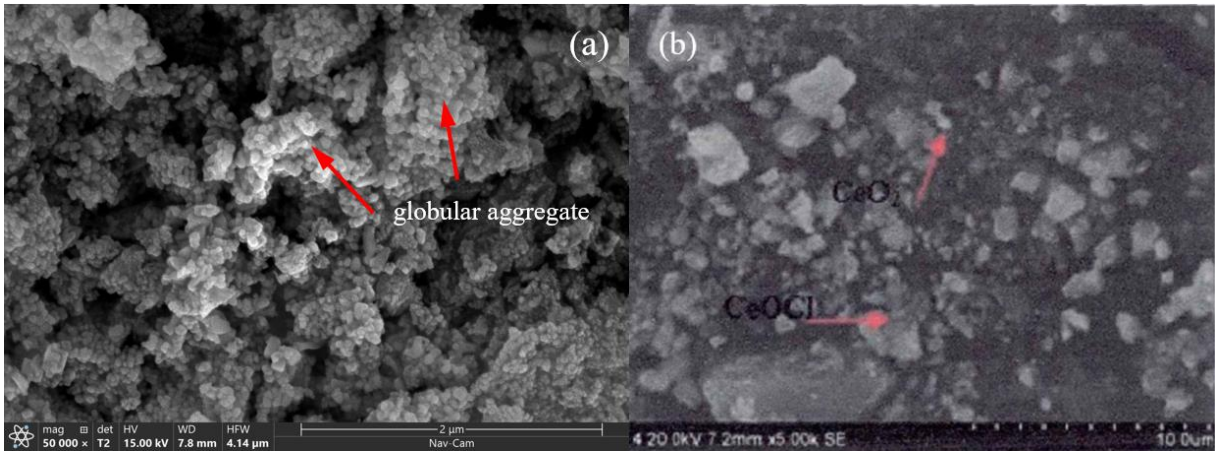

Figure 4. SEM images of the product: (a)-this study; and (b)- spray pyrolysis [17].

Verification

Table 3 presents the comparison of experimental and simulated results. The content of residual chlorine element (M_{Cl}) was used for the evaluation index of the product purity. It was observed that the error between the numerical simulation and experiment was within an acceptable range. Furthermore, it proved that the selected models, measured physical parameters, and

imposed boundary conditions were correct.

Table 3. Model verification.

	Power	Gas velocity	Average temperature	M_{cl}
Experiment	1 kW	2.1 m/s	901 K	1.64%
Simulation	1 kW	2.1 m/s	915.2 K	0.95%
Error	-	-	1.6%	0.7%

Effect of gas phase inlet velocity

Figure 5a illustrates the temperature field in the Venturi reactor. Although it is evident that the central temperature was always higher than the temperature near the wall, it accorded with the characteristics of the microwave heating model. Therefore, this temperature field was the key to obtaining CeO_2 particles with regular morphology and higher purity.

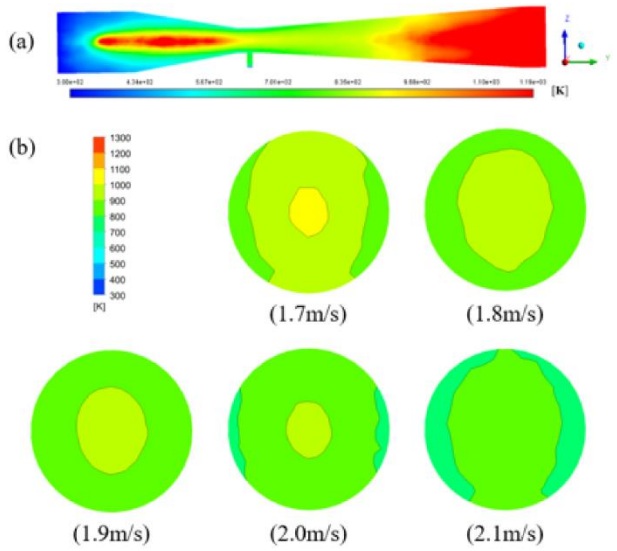

Figure 5. Temperature distribution (a) in the reactor and (b) on Y_2.

Different gas velocity (V_g) was set to 1.7 m/s, 1.8 m/s, 1.9 m/s, 2.0 m/s, and 2.1 m/s, respectively. Figure 5b indicated that the temperature in the reactor was distributed evenly under the microwave field, and there was no dead zone of heat and little temperature gradient. When V_g = 1.7 m/s, the center temperature of the monitoring surface exceeded 1000 K. When V_g = 1.8 ~ 2.1 m/s, the center temperature was lower than 1000 K, and the highest center temperature area decreased gradually. The increase of V_g decreased the reactor temperature, but it had a negligible impact on the tendency of temperature distribution. Figure 6a showed that the increase of gas inlet velocity increased the local velocity at the Venturi tube, the gas and raw material had a better mixing, but the heating time of $CeCl_3$ was shortened. The mass fraction of CeO_2 reached 99.7% when V_g = 1.7 m/s, which indicated that the highest reaction involvement of raw material was achieved. With gas velocity increasing, chlorine element content increased on each monitoring surface. It indicated that increasing gas velocity decreased the purity of CeO_2, as shown in Figure 6b.

Effect of raw material inlet velocity

When V_g=2.1 m/s, the effect of various material inlet velocities (0.01 m/s, 0.02 m/s, 0.03 m/s, 0.04 m/s, and 0.05 m/s) on the purity of CeO_2 was investigated. The nephogram of the CeO_2 mass fraction at the outlet is shown in Figure 7a.

The effect of material velocity (V_m) on the reaction is shown in Figure 7b. It was observed that when V_m = 0.01 m/s, the purity of CeO_2 was lower than 98%. Under this circumstance, the insufficient initial velocity of $CeCl_3$ prevented it from increasing to a higher height to mix with the oxygen. Subsequently, $CeCl_3$ deposited at the bottom, causing an incomplete reaction. When V_m = 0.02 m/s, CeO_2 purity increased by 1%. When V_m = 0.05 m/s, CeO_2 purity reached 99.8%, indicating that $CeCl_3$ mixed well with oxygen

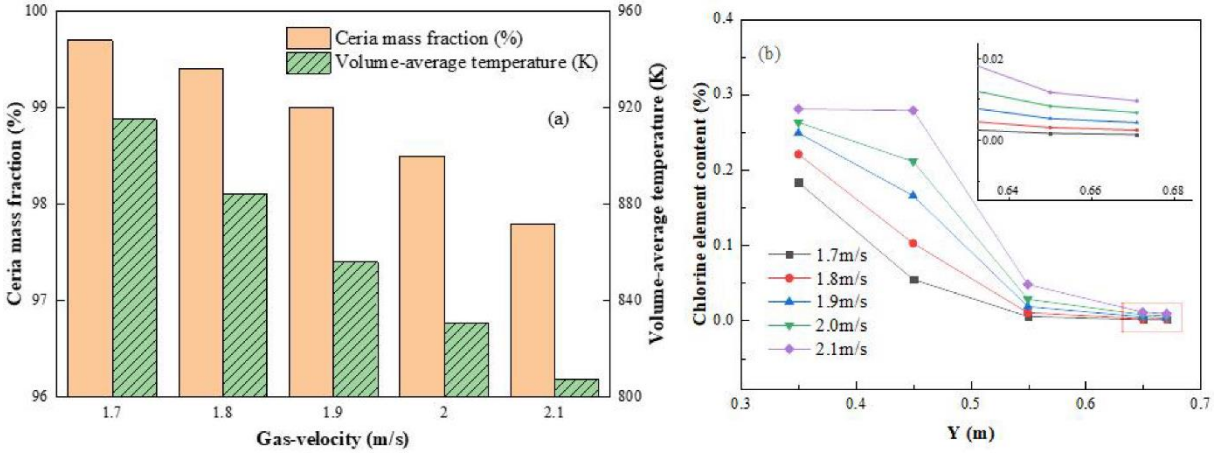

Figure 6. (a) Effect of the gas inlet velocity on Cerium oxide mass faction and volume-average temperature; and (b) Chlorine element content on each monitoring surface.

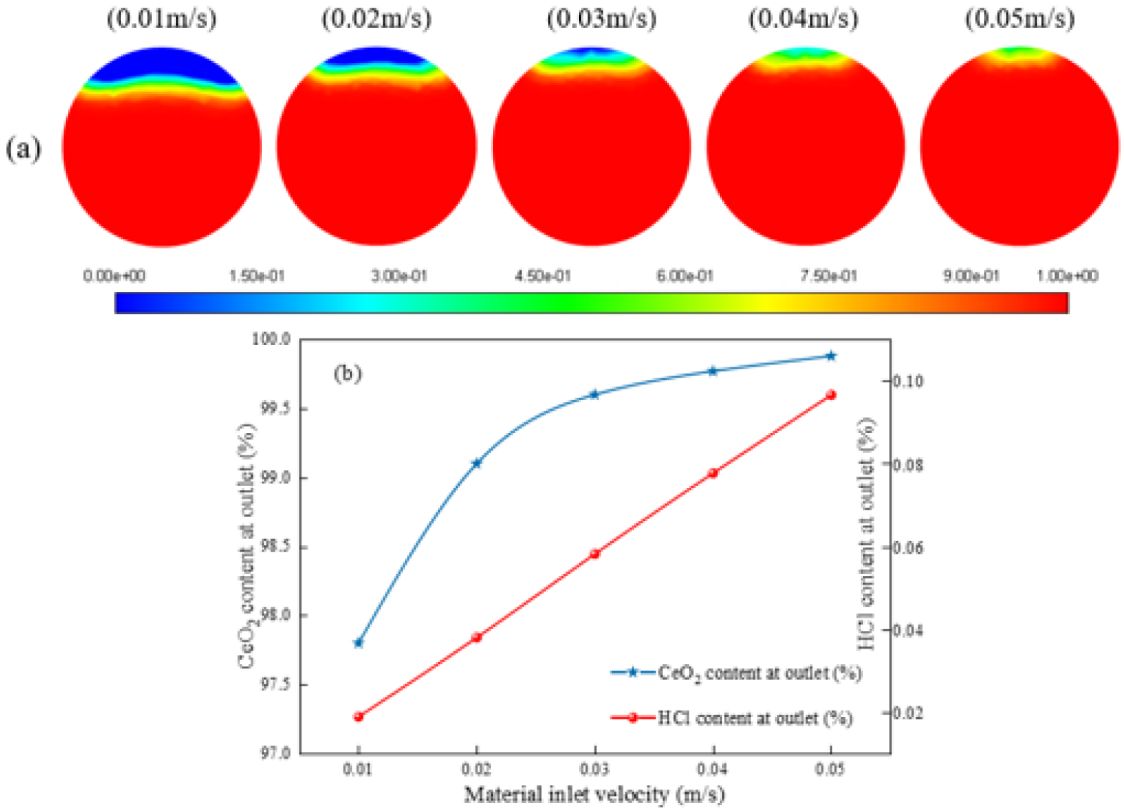

Figure 7. (a) Nephogram of CeO_2 content at the outlet; and (b) Effect of the gas phase inlet velocity on CeO_2 content at the outlet.

by this condition. On the other hand, the content of HCl continuously increased as the material velocity increased. Therefore, it proved that increasing material velocity benefited the chemical reaction. Among the five studied cases, the best results were achieved when V_m = 0.05 m/s.

Energy consumption and cost calculation

According to the experimental process of spray pyrolysis, the heating cost, energy consumption, and carbon dioxide (CO_2) emission were calculated under microwave jet-flow pyrolysis and spray pyrolysis using Eqs (11–16). The CO_2 emission calculation in this study was based on the CO_2 produced by the coal-fired electric generation according to the electric quantity used by the microwave oven. However, there was no CO_2 emission during the whole experimental process. As a result, the heating cost, energy consumption, and CO_2 emission were sharply decreased, as shown in Figure 8. It indicated that microwave jet-flow pyrolysis not only had the advantages of improving particles' morphology but also had a better economic benefit and lower carbon emission than spray pyrolysis. Furthermore, the costs will be further reduced if the production reaches an industrial scale.

$$C_1 = V\rho p_1 \tag{11}$$

where C_1 is the heating cost of spray pyrolysis (yuan) when 27 g CeO_2 is prepared, V is the volume consumption of propane, 24.7 (m^3), ρ is the density of propane 1.83 (kg/m^3), P_1 is the price of propane, 4.9 (yuan/kg).

$$C_2 = 27P_{micro}p_2/Q\varphi \tag{12}$$

where C_2 is the cost of microwave heating (yuan) when 27 g CeO_2 is prepared, P_{micro} is microwave power, 1 (kW), φ is the efficiency of a microwave oven, which is 70%, p_2 is the industrial electric charge, 1.5 (yuan/kWh), Q is the mass flow rate of CeO_2 at the outlet of the reactor 28.044 (g/h).

$$E_1 = b_1V \tag{13}$$

where E_1 is the energy consumption of spray pyrolysis method (kJ), b_1 is the burn value of propane, which is 1.0152e+5 (kJ/m^3), V is the volume consumption of propane, 24.7 (m^3).

$$E_2 = 3.6*10^6*27P_{micro}/Q\varphi \tag{14}$$

where E_2 is the energy consumption of microwave heating (kJ).

$$e_1 = 3VpM_{co_2}/M_{pro} \tag{15}$$

where e_1 is CO_2 emission of spray pyrolysis method (kg), M_{co_2} represents the molecular weight of CO_2, which is 44. M_{pro} represents the molecular weight of propane, which is 44.1.

$$e_2 = 27fP_{micro}/Q\varphi \quad (16)$$

where e_2 is the CO_2 emission of thermal power (kg), and f represents the CO_2 emission per kilowatt-hour generation, 0.785 (kg/kWh).

CONCLUSION

According to the XRD pattern, a single-phase CeO_2 was obtained, and the crystal grew well. SEM images showed CeO_2 nanoparticles obtained in this study had sphere-like morphology and smaller size. The increase of the gas inlet velocity decreased the average temperature when V_g = 1.7 m/s, V_m = 0.05 m/s, and the mass fraction of CeO_2 at the outlet reached 99.7% and 99.8%, respectively. Compared with the spray pyrolysis method, the heating cost, energy consumption, and CO_2 emission were sharply decreased in this study. Furthermore, it demonstrated that jet-flow pyrolysis via microwave heating was a low-carbon and cost technology.

ACKNOWLEDGEMENTS

This research was supported by the National Natural Science Foundation of China(51904069), the Fundamental Research Funds for the Central Universities(N2223026), and the Scientific Research Fund Project of Northeastern University at Qinhuangdao (XNY201808).

REFERENCES

[1] K.B. Kusuma, M. Manju, C.R. Ravikumar, N. Raghavendra, M.A. Shilpa Amulya, H.P. Nagaswarupa, H.C. Ananda Murthy, M.R. Anil Kumar, T.R. Shashi Shekhar, Appl. Surf. Sci. Adv. 11 (2022) 100304. https://doi.org/10.1016/j.apsadv.2022.100304.

[2] P. Janos, J. Ederer, V. Pilarova, J. Henych, J. Tolasz, D. Milde, T. Opletal, Wear 362-363 (2016) 114–120. https://doi.org/10.1016/j.wear.2016.05.020.

[3] S.J. Liang, X. Jiao, X.H. Tan, J.Q. Zhu, Appl. Opt. 57 (2018) 5657–5665. https://doi.org/10.1364/AO.57.005657.

[4] F. Wei, C.J. Neal, T.S. Sakthivel, Y.F. Yu, M. Omer, A. Adhikary, S. Ward, K.M. Ta, Bioact. Mater. 21 (2023) 547–565. https://doi.org/10.1016/j.bioactmat.2022.09.011.

[5] M. Ramachandran, M. Shanthi, R. Subadevi, M. Sivakumar, Vacuum 161 (2019) 220–224. https://doi.org/10.1016/j.vacuum.2018.12.002.

[6] S. Gnanam, V. Rajendran, J. Alloys Compd. 735 (2018) 1854–1862. https://doi.org/10.1016/j.jallcom.2017.11.330.

[7] C. Lv, Q.Y. Zhao, Z.M. Zhang, Z.H. Dou, T.A. Zhang, H.L. Zhao, Trans. Nonferrous Met. Soc. China 25 (2015) 997–1003. https://doi.org/10.1016/S1003-6326(15)63690-1.

[8] A.Z. Fia, J. Amorim, Energy 218 (2021) 119472. https://doi.org/10.1016/j.energy.2020.119472.

[9] J. Liu, J.H. Liu, B.W. Wu, S.B. Shen, G.H. Yuan, L.Z. Peng, Chin. J. Eng. 39 (2017) 208–214. DOI: 10.13374/j.issn2095-9389.2017.02.007.

[10] E. Meloni, M. Martino, M. Pierro, P. Pullumbi, F. Brandani, V. Palma, Energies 15 (2022) 4119. https://doi.org/10.3390/en15114119.

[11] V. Palam, D. Barba, M. Cortese, M. Martino, S. Renda, E. Meloni, Catalysts 10 (2020) 246. https://doi.org/10.3390/catal10020246.

[12] E. Meloni, M. Martino, V. Palma, Renewable Energy 197 (2022) 893–931. https://doi.org/10.1016/j.renene.2022.07.157.

[13] J.Y. Zhu, L.P. Yi, Z.Z. Yang, M. Duan, Chem. Eng. J. 407 (2021) 127197. https://doi.org/10.1016/j.cej.2020.127197.

[14] D. Salvi, D. Boldor, G.M. Aita, C.M. Sabliov, J. Food Eng. 104 (2011) 422429. https://doi.org/10.1016/j.jfoodeng.2011.01.005.

[15] C.D. Si, J.J. Wu, Y.X. Zhang, G.J. Liu, Q.J. Guo, Fuel 242 (2019) 159–149. https://doi.org/10.1016/j.fuel.2019.01.002.

[16] D.L. Ye. Practical Inorganic Thermodynamics Data Manual; Cao, S.L., Ed., Metallurgical Industry Press, Beijing (1981), p. 262–263, 265-266. ISBN:7-5024-3055-5.

[17] X.H. Liu. (2011). [Master's Thesis, Northeastern University]. China National Knowledge Infrastructure. https://kns.cnki.net/kcms2/article/abstract?v=3uoqIhG8C475KOm_zrgu4lQARvep2SAkbI4wwVeJ9RmnJRGnwiiNVgbPSHgq3mML_3baomtbo8MY72vRZI789SFqng4qPhOf&uniplatform=NZKPT.

LV CHAO[1,3]
YIN HONGXIN[1]
LIU YANLONG[1]
CHEN XUXIN[1]
SUN MINGHE[1]
ZHAO HONGLIANG[2]

[1]School of Control Engineering, Northeastern University, Hebei, China

[2]School of Metallurgy and Ecological Engineering, University of Science and Technology Beijing, Beijing, China

[3]State Key Laboratory of Complex Nonferrous Metal Resources Clean Utilization, Kunming University of Science and Technology,Yunnan, China

NAUČNI RAD

PROUČAVANJE PROCESA PRIPREME CeO_2 PIROLIZOM U VENTURI REAKTORU SA MIKROTALASNIM ZAGREVANJEM

Metoda pirolize raspršivanjem ima nedostatak začepljenja mlaznica, a konvencionalni model grejanja izaziva veliki temperaturni gradijent, što dovodi do neravnomernog grejanja reaktanata. U ovom korišćeni su cerijum-hlorid heptahidrat i Venturi reaktor. Mikrotalasno zagrevanja je korišćeno da bi se pripremio jednofazni sferični cerijum oksid. Srednja veličina čestica bila je blizu 80 nm. Proizvod je okarakterisan XRD, SEM i EDS tehnikama. Čistoća, morfologija i potrošnja energije su upoređeni sa konvencionalnom pirolizom raspršivanjem. Softver Fluent, u kombinaciji sa HFSS, korišćen je za simulaciju efekata različitih uslova procesa na čistoću proizvoda i temperaturno polje u reaktoru. Utvrđeno je dobro slaganje između eksperimentalnih i simuliranih rezultata. Rezultati su pokazali da se sa povećanjem brzine gasa distribucija temperaturnog polja ne menja. Najmanji maseni udeo elementa hlora od 0,13% postignut je kada je brzina ulaznog gasa bila 1,7 m/s. Kada je ulazna brzina materijala bila 0,05 m/s, maseni udeo elementa hlora je bio ispod 0,1%, što je ukazivalo na potpunu reakciju reaktanata. Izračunato je da su troškovi grejanja, potrošnja energije i emisija CO_2 naglo smanjeni u poređenju sa metodom pirolize raspršivanjem.

Ključne reči: cerijum oksid, ekonomska korist, mikrotalasno zagrevanje, numerička simulacija.

CI&CEQ
Chemical Industry & Chemical Engineering Quarterly

Available online at
Association of the Chemical Engineers of Serbia AChE
www.ache.org.rs/CICEQ

Chem. Ind. Chem. Eng. Q. 29 (4) 281–289 (2023) CI&CEQ

SEVGI CAN GÖL
ELIF AKBAY

Eskişehir Technical University, Dept. of Chemical Engineering, İki Eylül Campus, Eskişehir, Turkey

THE EFFECT OF METAL-TITANIA INTERACTION ON PHOTODEGRADATION IN SBA-15-SUPPORTED METAL-TITANIA PHOTOCATALYSTS

Article Highlights

- Several transition metals were inserted into the Ti-SBA-15 by using two-step synthesis methods
- Co-Ti-SBA-15 is a suitable photocatalyst with the highest photocatalytic activity for dye
- The enhanced activity comes from the increased electron transfer mobility due to metal doping
- Co-Ti-SBA-15 has high stability in dye degradation over five-run without any structural deviation

Abstract

Several transition metals (Fe, Cu, Ni, Cr, and Co) were inserted into the Ti-SBA-15 using two-step synthesis methods. XRD, SEM-EDX, N_2 adsorption-desorption isotherms, XRF, and UV-DRS analysis were used for characterizations. The results confirmed preserving an ordered mesoporous structure, well-dispersed Ti-metal and enhanced light absorption compared with Ti-SBA-15. The photocatalytic performances were evaluated in the degradation of methylene blue under UV light. The results show that the Co-Ti-SBA-15 exhibited the highest photocatalytic activity among the prepared photocatalysts for the degradation of methylene blue. The significant activity increase might be attributed to the increased reactant adsorption by the mesoporous structure of SBA-15, the good distribution of TiO_2 in the pores of SBA-15, and the increased electron transfer mobility due to metal doping. In addition to efficiency, Co-Ti-SBA-15 is a suitable catalyst for dye degradation, exhibiting good stability in methylene blue degradation over five photocatalytic runs without any deviation of the structure.

Keywords: transition metals, mesoporous material, Ti-SBA-15, photocatalytic degradation, reusability.

SCIENTIFIC PAPER

UDC 544.526.5:546:66

Photocatalysis is mainly used for the abetment of environmental pollutants and has been attractive to researchers worldwide [1]. Photocatalysis can be superior to other widely used methods, such as oxidation, absorption, ion exchange, etc. [2]. Some semiconductors (TiO_2, Fe_2O_3, ZnO, ZrO_2, Nb_2O_5, SnO_2, and others) and a number of nanocomposites such as Ag-Mn_xO_y, WO_3/g-C_3N_4, g-C_3N_4/ $CdWO_3$, and TiO_2-SnO_2-Sb_2O_5-NiO-carbon nanotubes have been used as photocatalysts and have attracted significant attention due to their wide application for pollution abetment [3–8].

Most importantly, TiO_2 is widely used because of its high photo-stability, low toxicity, commercial availability, and large band gap of 3.2 eV [9–11]. However, its photocatalytic activity is restricted by specific parameters such as low surface area, coagulation in aqueous media, and separation and recycling problems [12]. This limitation may be overcome when dispersed on mesoporous silica support such as Santa Barbara Amorphous (SBA-15).

Correspondence: E. Akbay, Eskişehir Technical University, Dept. of Chemical Engineering, İki Eylül Campus, Eskişehir, 26555, Turkey.
E-mail: eodes@eskisehir.edu.tr
Paper received: 17 October, 2022
Paper revised: 27 December, 2022
Paper accepted: 10 January, 2023

https://doi.org/10.2298/CICEQ221017001G

SBA-15 is a significant mesoporous silica noted for its high surface area, narrow pore size distribution, uniform meso porosity, low cost, and biodegradable template [2,13]. Immobilization of TiO_2 into the SBA-15 could reduce the particle size of TiO_2 and thereby avoid aggregation. The synthesized material is a more effective photocatalyst than commercial Degussa P25 or another synthesized nanoparticle form. There are many studies on different synthesizing methods and optimum TiO_2 loading to synthesize Ti-SBA-15 in the literature [14–17]. The Si/Ti ratio is critical at approximately sixteen because its low or high values defect the mesopore structure of SBA-15 and decrease photocatalytic efficiency [16–18].

TiO_2-SBA-15 can be useful for photocatalysis but can absorb only 4% of the spectrum [19]. On the other hand, doping TiO_2-SBA-15 by metals such as Ag [20], Au [21], W [22], Fe [19], CoMo [23], Sn [24], and Pt [25] extends the response to a wide range of the spectrum and exhibits a synergistic effect on narrowing of the TiO_2 band gap up to 1.45 eV [4]. In these papers, titanium was successfully inserted into the SBA-15 structure by different methods using organic titanium sources and then metal doping by post-synthesized methods. The obtained nanocomposites enhanced the reactant adsorption by the mesoporous structure of SBA-15 with a good distribution of TiO_2, as well as reduced electron-hole recombination rates due to metal doping. As a result, a significant enhancement in photocatalytic activity under visible light or UV has been obtained for the degradation of organic pollutants and the production of added-value chemicals.

Therefore, in this paper, the Ti-SBA-15 composite was prepared by the direct synthesized method using a TiO_2 nano-powder source. To enhance the extended range of the spectrum of TiO_2, a number of transition metal nanoparticles (Cu, Fe, Co, Cr, and Ni) were chosen for doping on the surface of the TiO_2/SBA-15 because transition metals have good electron changeability enhancing catalytic activity, anti-poisoning property, longevity, regeneration, and low cost [26]. The composition, morphology, and optical properties of synthesized photocatalysts are characterized by XRD, SEM-EDX, XRF, UV-DRS, and N_2 adsorption-desorption isotherms. In addition, the photocatalytic activity and stability of the photocatalysts have been evaluated for the degradation of methylene blue under UV light irradiation. Finally, the reused photocatalysts have been tested to determine any structural deviation using XRD, SEM-EDX, and N_2 adsorption-desorption isotherms.

MATERIALS AND METHODS

Chemicals

The tetraethyl orthosilicate (TEOS), Pluronic-123 ((triblock poly(ethylene oxide)-poly(propylene oxide)-poly(ethylene oxide) were bought from Sigma Aldrich. The HCl (37%) was obtained from Riedel-de Haen. The TiO_2 nano-powder, Degussa-P25, and methylene blue were obtained from Merck. The iron (III) nitrate nonahydrate (Fe $(NO_3)_3$. $9H_2O$), Copper (II) nitrate trihydrate (Cu $(NO_3)_2.3H_2O$), Chromium (III) nitrate nonahydrate (Cr $(NO_3)_3.9H_2O$), and Cobalt (II) nitrate hexahydrate (Co $(NO_3)_2.6H_2O$) were supplied by Carlo Erba Reagents. The nickel (II) nitrate hexahydrate (Ni $(NO_3)_2.6H_2O$) was bought from Roth.

Synthesis

The SBA-15 synthesis procedure was given in previous work [27]. The addition of TiO_2 modified this method; 4 g of Pluronic-123 was added to 30 mL of distilled water in a magnetic stirrer at 35 °C for 3 h, after which 150 mL of 2 M HCl was added. In this step, the amount of nano-TiO_2 adjusted to Si/Ti=16 was added to the solution and mixed for two hours, then 9 mL of TEOS was added. The obtained mixture was stirred for twenty hours at 40 °C and was aging to react at 100 °C overnight in Teflon. The samples were filtered and washed with deionized water to remove excess HCl. Drying was carried out at 30 °C for forty-five hours, and calcination was applied at 600 °C under airflow for five and a half hours.

In the metal doping step; 1 g of TiO_2/SBA-15 was dispersed in 10 mL of an aqueous solution of $Fe(NO_3)_3$, $Cr(NO_3)_3$, $Ni(NO_3)_2$, and $Cu(NO_3)_2$ at a loading amount of 10 wt.% by an ultrasonic homogenizer for 15 min. The resulting solution was dried in an oven at 110 °C. Next, the dried sample was calcined at 300 °C for two hours at a heating rate of 5 °C/min. Finally, the sample was washed three times with 250 mL distilled water and dried in an oven at 80 °C for twelve hours.

Characterization

X-ray diffraction (XRD) analyses were performed by an X-ray diffractometer (RigakuRind XRD MiniFlex 300/600) and Cu-Kα (1.54 Aº) radiation (40kV-15mA) with scanning from 2Θ=70° to 2Θ=5° at a rate of 2° per minute^{-1}. The crystallite sizes of the samples were found using Scherrer's equation of $D=k\lambda/\beta\cos\theta$ where D is the crystallite diameter, λ is the radiation wavelength (1.5406Å), β is the peak full with half maximum (FWHM), θ is the diffracting angle and k=0.90 for the spherical shape particle.

Surface analysis of the photocatalysts was performed by a HITACHI TM 3030 Plus branded SEM device. XRF analysis was carried out by Rigaku ZSX Primus II. The BET (Brunauer-Emmett-Taller) specific surface area was calculated from N_2 adsorption-desorption isotherms measured at 77 K in an automatic

adsorption apparatus (Tristar II 3020 Operator Manual v3.02, Micrometric). Degassing of the samples was at 250 °C for four hours. The pore size distributions of the catalysts were given using the Barrett-Joyner-Halenda (BJH) method. UV Diffuse Reflectance Spectra (DRS) were achieved from 200 to 700 nm using a UV-vis spectrophotometer (Shimadzu UV-3600).

Photocatalytic reactions

Photocatalytic degradation of methylene blue was performed in a quartz reactor system equipment with a temperature controller. The reactor system had a thin layer of aluminum foil with 99 % purity. The light source was four 8 W UV (364 nm) low-pressure mercury lamps.

In a typical experiment, 20 mg/L of 150 mL methylene blue at natural pH was taken, and 75 mg of the catalyst was added to the solution. The reaction mixture was magnetically stirred for one hour to reach the adsorption-desorption equilibrium without light. Then, taking 2 mL of the solution, the catalyst was taken by centrifugation at 13000 rpm for twenty minutes. The concentration of the samples was measured by Spectrophotometer (SHIMADZU UV-2600 UV) at 664 nm. The conversion of methylene blue was calculated by dividing the concentration of methylene blue consumed during the reaction by its initial concentrations. After the photocatalytic reaction, the catalyst was collected from the reaction solution by centrifugation and reused five times. Before the following cycle, the catalyst was washed with ethanol and dried on filter paper to separate the methylene blue in the photocatalyst.

RESULTS AND DISCUSSION

To examine the structural properties of M-Ti-SBA-15, XRD, SEM-EDX, XRF, UV-DRS, and N_2 adsorption-desorption isotherms analyses were carried out after the metal doping. In addition, the photocatalytic activity of M-Ti-SBA-15 was evaluated on the degradation of methylene blue.

Morphological, textural, and optical properties of M-Ti-SBA-15

The photocatalysts were examined using low-wide angle XRD patterns given in Figures 1a and 1b. As can be seen in Figure 1a, the XRD patterns show a reflection peak at $2\Theta \cong 0.8°$, which is evidence that it had maintained the 2D hexagonal meso structure of SBA-15 in the synthesized catalysts [19,28]. However, the insertion of the metal decreases the peak intensities. As a result, it creates a tiny contradiction of the lattice parameter (a_0) of the photocatalyst obtained from the d100 spacing included in Table 1 [29]. The crystallite size of metal in the M-Ti-SBA-15 was calculated according to the Scherrer formula; the results are shown in Table 1. The crystallite size of the photocatalyst was approximately the same value for all types of metal because of pore diameter restrictions.

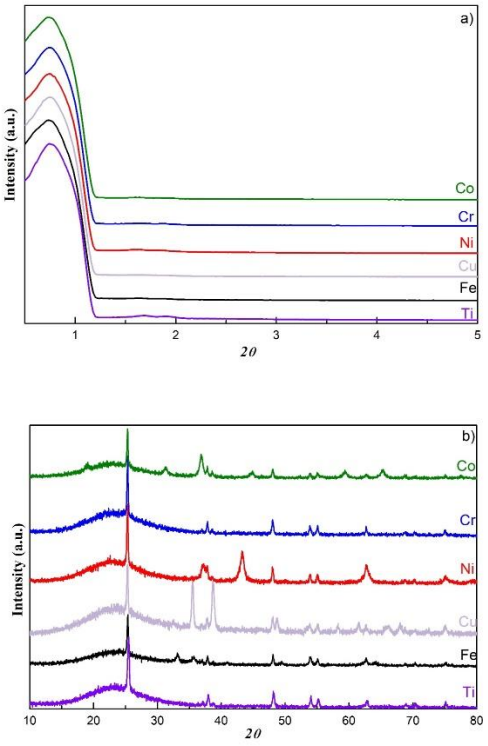

Figure 1. Low-angle XRD patterns (a) and wide-angle XRD patterns (b) of M-Ti-SBA-15 (M=Co, Cr, Ni, Cu, Fe).

Wide-angle XRD patterns of the synthesized catalysts confirm the presence of the crystalline structure of mesoporous M-TiO_2/SBA-15 catalyst (Figure 1b). As shown in Figure 1b, all M-Ti-SBA-15 photocatalysts show a wide and low-intensity peak at $2\theta = 24°$ related to the SBA-15 amorphous walls [17,30,31]. The diffraction peaks obtained from $2\theta \cong 25°$(101), 38° (004), 48° (200), 54° (105), 55° (211), and 63° (204) show the crystal structure of anatase-TiO_2 (JCPDS, 01-084-1285) and the remaining peaks prove the presence of the following metals; Co (JCPDS, 03-065-3103), Cr (JCPDS, 01-073-6548), Ni (JCPDS 65-6920), Cu (JCPDS, 01-080-1916), and Fe (JCPDS, 01-079-5902). A slight deviation after the metal insertion of the anatase TiO_2 peak indexed to the (101) plane at 25.5° indicates that the anatase TiO_2 and the inserted metal are in close contact to promote photogenerated electron transfer and, therefore, photocatalytic efficiency [21].

SEM images of M-Ti-SBA-15 were taken at 15 kV; the results are shown in Figure 2. As shown in

Figure 2a, the SBA-15 has rod-like morphology, which is typical for SBA-15 [32]. In the synthesized photocatalysts, after titania and metal nanoparticles were incorporated into the silica framework, the filamentous structure of SBA-15 remained, which is complies with the small-angle XRD results. Titania particles were distributed evenly on the SBA-15 pore walls in M-Ti-SBA-15 photocatalysts. This phenomenon is also clearly seen in the elemental mapping of Ti in the M-Ti-SBA-15 photocatalyst in Figure 3a. The image of the M-Ti-SBA-15 photocatalyst shows that the metal is well dispersed except for M=Cr, Cu. In these photocatalysts, agglomerated metal particles of different sizes are observed on the external surface of the SBA-15. The elemental mapping images of metals; Co, Cr, Cu, Fe, and Ni show that extremely good distribution was obtained after synthesis, as seen in Figure S1 (Supplementary materials).

The elemental analysis of M-Ti-SBA-15 was determined through XRF analysis and SEM-EDX analyses, as shown in Table 1. The obtained metal loadings in the M-Ti-SBA-15 are in good agreement with the value estimated in the synthesis procedure, except for the Cr metal. The numerical difference between the results of the SEM-EDX and the XRF analyses might have come from analysis techniques; the first is performed on the photocatalyst surface, and the other on the bulk. Only about 2% of the Cr metal was loaded due to the leaching of the Cr during washing in the loading process, as seen in Table 1. In the literature, Cr metal was loaded around 1% at most [33]. The leaching of the Cr might be overcome by loading the Cr metal before the Ti metal.

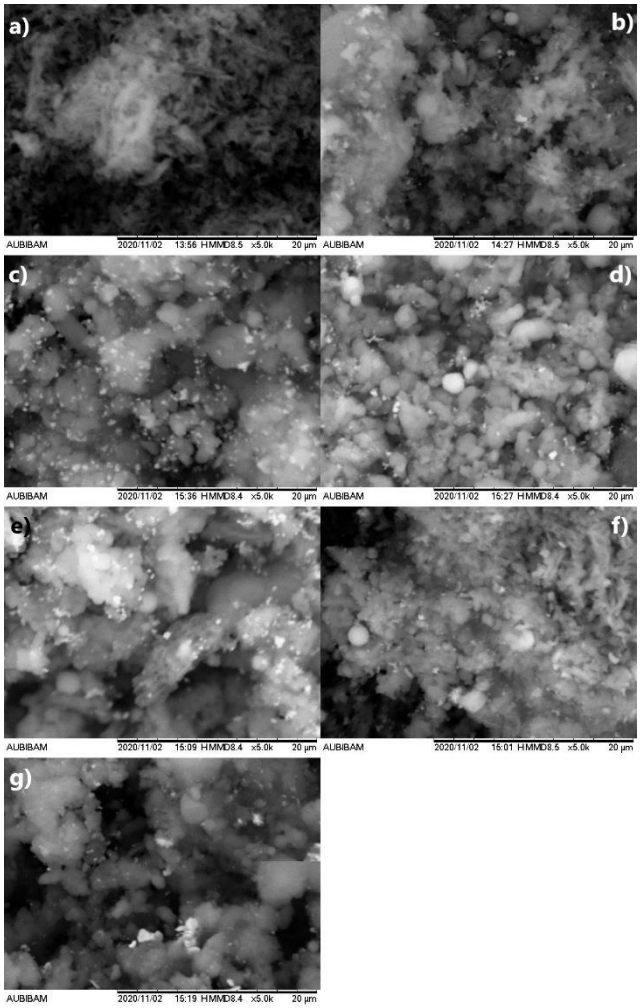

Figure 2. SEM images of SBA-15 (a), Ti-SBA-15 (b), and M-Ti-SBA-15; Co (c), Cr (d), Ni (e), Cu (f), and Fe (g).

Table 1. Structural, chemical, and textural properties of synthesized photocatalysts.

Catalyst	Loading metal amount (%)		Crystallite sizes of TiO_2 (nm)[a]	Surface Area BET[b] (m^2/g)	Pore Volume[c] (cm^3/g)	Pore Diameter (nm)[c]	Lattice parameter a_0(nm)[a]	Pore Wall Thickness nm[d]	Band Gap Energy[e] (eV)[f]
	Determined by XRF	Determined by SEM-EDX							
SBA-15	-	-	-	732	0.89	5.95	13.33	7.38	2.37
Fe-TiO_2/SBA-15	12.8	8.2	10.85	553	0.62	5.40	12.53	7.13	2.04
Cu-TiO_2/SBA-15	7.2	7.5	10.99	460	0.61	5.67	12.69	7.02	3.30
Ni-TiO_2/SBA-15	10.1	7.7	10.92	528	0.67	5.61	12.61	7.00	3.24
Cr-TiO_2/SBA-15	2.5	1.3	10.93	613	0.72	5.55	12.62	7.07	3.24
Co-TiO_2/SBA-15	11.2	7.1	10.87	533	0.62	5.44	12.55	7.11	2.00

[a] From XRD, [b] Multipoint BET method, [c] From BJH method, [d] Wall thickness (a_0 − pore diameter), [e] From UV-DRS

N_2 adsorption-desorption isotherms and the pore size distribution curves of M-Ti-SBA-15 were found using the BJH model from the desorption branch, as shown in Figure 3. According to the IUPAC classification, the synthesized SBA-15 and M-Ti-SBA-15 exhibited type IV characteristic curves with type H1 hysteresis loop [11]. The SBA-15 presents the hysteresis loop at moderate relative pressures ($0.6<p/p_0<0.73$) in a range representing the self-filling of mesopores due to capillary condensation, indicating that maintaining the uniform mesostructure of the SBA-15. All the M-Ti-SBA-15 catalysts also exhibited a similar trend in the hysteresis loop with a slightly higher relative pressure range than the SBA-15. The pore size distribution curves shown in Figure 4b display a uniform pore size of about 7.1 nm with a uniform cylindrical shape for all the samples [30], confirmed by SEM observation.

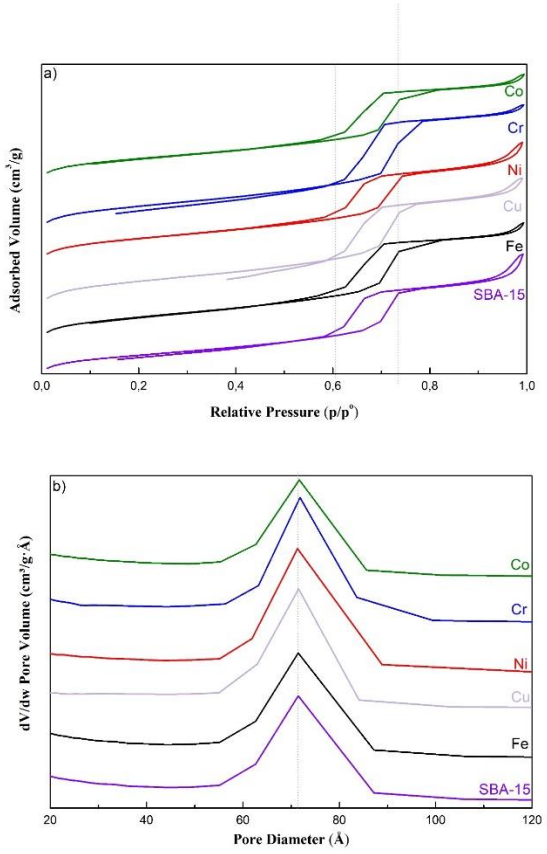

Figure 3. (a) N_2 adsorption-desorption isotherms and (b) pore distributions of M-Ti-SBA-15 (M=Co, Cr, Ni, Cu, Fe).

Textural properties concerning the M-Ti-SBA-15 are presented in Table 1. The decrease in BET surface area, pore volume, pore diameter, and pore wall thickness of the SBA-15 after metal doping perhaps comes from plugging the SBA-15 pores with metal and titania. However, its surface area still falls within the range of high-quality SBA-15, about 500-1000 m^2/g [34]. The textural properties of M-Ti-SBA-15 have minor variations depending on metal types which may be compatible with an ionic radius of metals [35,36]. Meanwhile, the pore wall of M (Fe, Co)-Ti-SBA-15 is thicker than the other metal types considering their ionic radius, which may be attributed to the metal and titania being successfully incorporated inside the mesopore walls [31].

UV-DRS analyses of synthesized photocatalysts are given in Figure 4. It was observed that Ti-SBA-15 has a large absorption drop of around 380 nm, which complies with the absorption on the bandgap of anatase TiO_2 [37]. In addition, the strong adsorption peak at about 350–400 nm demonstrates the TiO_2 particles are larger than 5 nm [38]. After metal doping, the obtained band at 200 nm–240 nm is attributed to the metal-doped SBA-15 framework silica [39]. The absorption range of the synthesized photocatalyst increased compared to the Ti-SBA-15. In particular, the absorption over a broad spectrum range in the Co-Ti-SBA-15 photocatalyst might positively affect the photocatalytic efficiency [40].

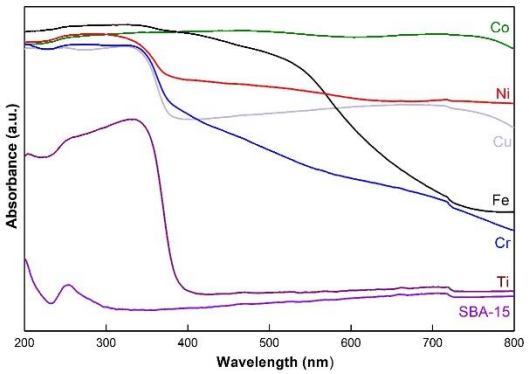

Figure 4. Diffuse reflectance UV-vis spectra of M-Ti-SBA-15 (M=Co, Cr, Ni, Cu, Fe).

The bandgap energy (E_g, eV) was calculated using the Kubelka-Munk function's modified plot, as shown in Figure S2 and Table 1. It is estimated by extrapolation of the linear part of the plot of $[F(R)]\,hv]^2$ versus hv, where h and v are Plank's constant and frequency [14,19].

The calculated values of the optical band gap energies were considerably blue-shift compared with those of the TiO_2 anatase phase (3.2 eV). The decrement in the bandgap energies of photocatalysts indicates quantization effects, which improves the photocatalytic properties.

Photocatalytic properties of M-Ti-SBA-15 and reusability

The photocatalytic activities of M-Ti-SBA-15 were evaluated by the degradation of methylene blue under UV-light irradiation. The results of the photocatalyst

efficiencies are given with adsorption and photocatalyst efficiencies calculated after subtracting the amount of adsorbed dye in Figures 5a and 5b, respectively.

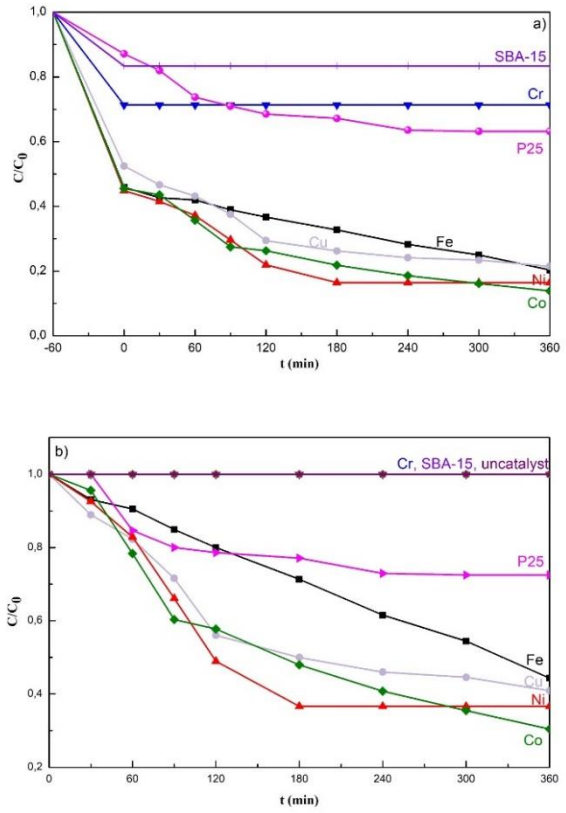

Figure 5. The photocatalytic degradation efficiency of M-Ti-SBA-15 (M=Co, Cr, Ni, Cu, Fe), SBA-15, and Degussa P25 a) with adsorption, and b) with subtracting the adsorption effect (Reaction conditions: 75 m catalyst,150 mL, 20 mg/L MB aqueous solution).

As shown in Figure 5, no methylene blue degradation was obtained in the absence of catalyst and the presence of pure SBA-15 (Figure 6b). It was observed that only SBA-15 reached the adsorption equilibrium after one hour due to the adsorption properties of the SBA-15 (see Figure 6a). The degradation efficiencies of P25 and M-Ti-SBA-15 (Fe, Cu, Ni, Co) toward MB were 27.6%, 55.7%, 60%, 63.4%, and 69.8% after 360 minutes of irradiation, respectively. The all-metal-doped photocatalyst exhibited higher photoactivity than the Degussa P25 in the conditions where all tested photocatalysts had the same amount of TiO_2, except Cr because little Cr was loaded, as understood from the SEM-EDX and XRF results. This enhanced efficiency could be due to the close contact between the titania and metals, increasing electron mobility to participate in the redox reaction to give active oxygen, which enhances the photodegradation of the methylene blue [2,14,20,41]. In this mechanism, with close contact, the electrons in the metal might be transferred to the conduction band of the TiO_2 and accumulate on the surface (1) of the TiO2 preventing the back transfer of electrons by the Schottky barrier [42]. Transferred electrons might reduce the oxygen on the surface of the Co-Ti-SBA-15 to obtain oxygen radicals ($\cdot O_2$)(2). These radicals might be combined with H_2O to give active species further ($\cdot OH$) (3 and 4). At the same time, the (h^+) ions might be directly oxidized by H_2O. Finally, the produced radicals degrade methylene blue to the products (5). The possible reaction process is as follows:

$$Co-Ti-SBA-15+h\nu \rightarrow Co-Ti-SBA-15\left(e^- + h^+\right) \quad (1)$$

$$Co-Ti-SBA-15\left(e^-\right)+O_2 \rightarrow Co-Ti-SBA-15+\bullet O_2^- \quad (2)$$

$$Co-Ti-SBA-15\left(h^+\right)+H_2O \rightarrow Co-Ti-SBA-15 +\bullet OH+H^+ \quad (3)$$

$$\bullet O_2^- + H^+ \rightarrow \bullet OOH \text{ or } \bullet OH \quad (4)$$

$$Methylene\ blue+\bullet O_2^- + \bullet OH \rightarrow Degradation\ products \quad (5)$$

In addition, the high surface area of the M-Ti-SBA-15 increased the adsorption ability of methylene blue molecules, which directly enhanced the reaction rate [21].

A comparison of the photocatalytic efficiency of Co-Ti-SBA-15 with other SBA-15 nanocomposites is given in Table 2. As can be seen in Table 2, the Co-Ti-SBA-15 is a promising catalyst under the given reaction conditions. Furthermore, in studies comparing the efficiency of the synthesized catalysts with Ti-SBA-15 or Degussa P25 efficiency under the same conditions was examined; Ag-TiO_2/SBA-15 [20] and Au-TiO_2/SBA-15 [21] photocatalysts exhibited 4 and 2 times higher photocatalytic activity than those of TiO_2/SBA-15 and Degussa P25, respectively. Compared with these catalysts, obtaining similar efficiency at the Co-Ti-SBA-15 photocatalyst is promising, making it possible to replace precious elements. Additionally, in another study, the photoactivity of Co-SBA-15 was compared with Degussa P25 under sunlight. The same value was found, which might indicate that enhanced photocatalytic efficiency comes from the synergistic effect of the Co-Ti interaction [43].

Overall, the Co-Ti-SBA-15 photocatalyst showed the highest degradation efficiency; therefore, this sample was selected for evaluation of reusability, as shown in Figure 6. After five cycles, no significant decrease in its photocatalytic activity was observed

Table 2. Comparison of the efficiency of some metal-SBA-15 photocatalysts.

Photocatalyst	Dyes	Reaction Conditions Dye concentration (mg/L)/catalyst dosage (mg) /adsorption time(min)/irradiation source	Catalytic efficiency (%), Time (min)	References
Au/TiO_2/SBA-15	Methylene Blue	20.0/100/30/ visible light (300 W)	100 %, 210	[21]
Ag-TiO_2/SBA-15	Methylene Blue	5.0/100/60/visible light (300 W)	89 %, 30	[20]
Ag/CeO_2/SBA-15	Congo red	0.5/500/30/UV (2.16W) pH = 5.5	100%, 180	[44]
WO_3-SBA-15	Methylene Blue	30/100/-/visible light (500W)	90%, 300	[45]
Fe-Ti-SBA-15	Methylene Blue	15.0/20/60/UV (400W)	82%,180	[46]
TiO_2/SBA-15	Methylene Blue	30.0/20/60/UV (300W)	73 %, 150	[11]
Ag@AgBr/SBA-15	Rhodamine B	20.0/300/60/ UV (500W)	88 %, 300	[47]
Co-SBA-15	Methyl violet	50.0/25/120/Solar radiation pH=6	69 %, 150	[43]
Co-Ti-SBA-15	Methylene Blue	20.0/75/60/ UV (32W)	70%, 360	Present work

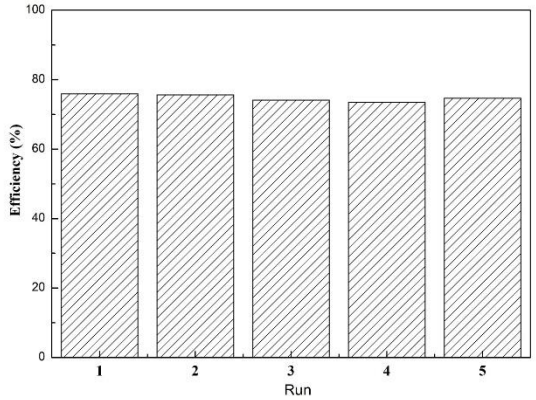

Figure 6. The reusability of Co-Ti-SBA-15.

After this, the reused catalyst was characterized by XRD, SEM-EDX, and N_2 adsorption-desorption isotherms/desorption analyses to determine the structural deviation (Figures S3, S4, and S5 and Table S1). The reused catalyst retained the crystal and hexagonal structure of fresh Co-Ti-SBA-15 and uniform meso structure despite some pore-clogging with the pore size slightly changed from 5.44 nm to 4.76 nm. Furthermore, the obtained metal loadings in the Co-Ti-SBA-15 from the SEM-EDX results were the same as the value of fresh photocatalyst, which showed that no Co-metal leaching occurred during the dye degradation process. Therefore, Co-Ti-SBA-15 maintains its activity and stability after reuse for several cycles.

CONCLUSION

Transition metals (Fe, Cu, Ni, Cr, and Co) were loaded onto highly dispersed TiO_2 within the mesostructured SBA-15. The characterization results show that the expected metal and titania loadings were obtained with a good distribution on SBA-15. Furthermore, the synthesized materials exhibited an intimate contact between the metal and titania, increasing electron mobility and enhancing photocatalytic activity by widening the photo response UV range. Among all the evaluated photocatalysts, Co-Ti-SBA-15 showed a photocatalytic degradation efficiency four times as high as Degussa P25, comparable to the efficiency obtained with precious metals. Therefore, the Co-Ti-SBA-15 photocatalyst, exhibiting excellent reusability of the photocatalytic activity under UV irradiation, may be used in the practical application of pollutant degradation.

ACKNOWLEDGMENT

This study was supported by Eskişehir Technical University Scientific Research Projects Commission under grant no: 22ADP043.

REFERENCES

[1] D.B. Miklos, C. Remy, M. Jekel, K.G. Linden, J.E. Drewes, U. Hübner, Water Res. 139 (2018) 118–131. https://doi.org/10.1016/j.watres.2018.03.042.

[2] D.B. Miklos, C. Remy, M. Jekel, K.G. Linden, J.E. Drewes, U. Hübner, Water Res. 139 (2018) 118–131. https://doi.org/10.1016/j.watres.2018.03.042.

[3] H. Wang, L. Zhang, Z. Chen, J. Hu, S. Li, Z. Wang, J. Liu, X. Wang, Chem. Soc. Rev. 43(15) (2014) 5234–5244. https://doi.org/10.1039/C4CS00126E.

[4] R. Singh S. Dutta, Adv. Powder Technol. 29(2) (2018) 211–219. https://doi.org/10.1016/j.apt.2017.11.005.

[5] M. Saeed, A. Ahmad, R. Boddula, Inamuddin, A.u. Haq, A. Azhar, Environ. Chem. Let 16(1) (2018) 287–294. https://doi.org/10.1007/s10311-017-0661-z.

[6] A. Priya, R.A. Senthil, A. Selvi, P. Arunachalam, C.K. Senthil Kumar, J. Madhavan, R. Boddula, R. Pothu, A.M. Al-Mayouf, Mater. Sci. Energy Technol. 3 (2020) 43–50. https://doi.org/10.1016/j.mset.2019.09.013.

[7] M. Karimi, S. Mansour Bidoki, A. Benvidi, Environ. Eng. Res. 27(3) (2022) 200429–200420. https://doi.org/10.4491/eer.2020.429.

[8] A. Maavia, I. Aslam, M. Tanveer, M. Rizwan, M.W. Iqbal,

M. Tahir, H. Hussain, R. Boddula, M. Yousuf, Mater. Sci. Energy Technol 2(2) (2019) 258–266. https://doi.org/10.1016/j.mset.2019.01.004.

[9] A. Mehta, A. Mishra, M. Sharma, S. Singh, S. Basu, J. Nanopart. Res. 18(7) (2016). https://doi.org/10.1007/s11051-016-3523-x.

[10] A.S.M. Nur, M. Sultana, A. Mondal, S. Islam, F.N. Robel, A. Islam, M.S.A. Sumi, J. Water Process. Eng. 47 (2022) 102728. https://doi.org/10.1016/j.jwpe.2022.102728.

[11] Q. Wei, X.J. Chen, P.F. Wang, Y.B. Han, J.C. Xu, B. Hong, H.X. Jin, D.F. Jin, X.L. Peng, J. Li, Y.T. Yang, H.L. Ge, X.Q. Wang, Chem. Phys. 510 (2018) 47–53. https://doi.org/10.1016/j.chemphys.2018.05.012.

[12] B. Castanheira, L. Otubo, C.L.P. Oliveira, R. Montes, J.B. Quintana, R. Rodil, S. Brochsztain, V.J.P. Vilar, A.C.S.C. Teixeira, Chemosphere 287 (2022) 132023. https://doi.org/10.1016/j.chemosphere.2021.132023.

[13] M.T.P. da Silva, J. Villarroel-Rocha, C.F. Toncón-Leal, F.F. Barbosa, M.O. Miranda, M.A.M. Torres, K. Sapag, S.B.C. Pergher, T.P. Braga, Microporous Mesoporous Mater. 310 (2021). https://doi.org/10.1016/j.micromeso.2020.110582.

[14] L.A. Calzada, R. Castellanos, L.A. García, T.E. Klimova, Microporous Mesoporous Mater. 285 (2019) 247–258. https://doi.org/10.1016/j.micromeso.2019.05.015.

[15] T.-H. Liou, L.-W. Hung, C.-L. Liu, T.-Y. Zhang, J. Porous Mater. 25(5) (2018) 1337–1347. https://doi.org/10.1007/s10934-017-0544-5.

[16] D.S. Conceição, C.A.L. Graça, D.P. Ferreira, A.M. Ferraria, I.M. Fonseca, A.M. Botelho do Rego, A.C.S.C. Teixeira, L.F. Vieira Ferreira, Microporous Mesoporous Mater. 253 (2017) 203–214. https://doi.org/10.1016/j.micromeso.2017.07.013.

[17] M.M. Araújo, L.K.R. Silva, J.C. Sczancoski, M.O. Orlandi, E. Longo, A.G.D. Santos, J.L.S. Sá, R.S. Santos, G.E. Luz, L.S. Cavalcante, Appl. Surf. Sci. 389 (2016) 1137–1147. https://doi.org/10.1016/j.apsusc.2016.08.018.

[18] G. Li, B. Wang, W.Q. Xu, Y. Han, Q. Sun, Dyes Pigm. 155 (2018) 265–275. https://doi.org/10.1016/j.dyepig.2018.03.058.

[19] M. Filip, G. Petcu, E.M. Anghel, S. Petrescu, B. Trica, P. Osiceanu, N. Stanica, I. Atkinson, C. Munteanu, M. Mureseanu, V. Parvulescu, Catal. Today 366 (2021) 10–19. https://doi.org/10.1016/j.cattod.2020.08.003.

[20] L. Liang, Y. Meng, L. Shi, J. Ma, J. Sun, Superlattices Microstruct. 73 (2014) 60–70. https://doi.org/10.1016/j.spmi.2014.05.008.

[21] Y. Chen, J. Wang, W. Li, M. Ju, Mater. Lett. 159 (2015) 131–134. https://doi.org/10.1016/j.matlet.2015.04.030.

[22] F. Chang, J. Wang, J. Luo, J. Sun, B. Deng, X. Hu, Colloids Surf. A. Physicochem. Eng. Asp. 499 (2016) 69–78. https://doi.org/10.1016/j.colsurfa.2016.04.013.

[23] T.T. Nguyen, E.W. Qian, Microporous Mesoporous Mater. 265 (2018) 1–7. https://doi.org/10.1016/j.micromeso.2018.01.026.

[24] D.C. Khandekar, A.R. Bhattacharyya, R. Bandyopadhyaya, J. Environ. Chem. Eng. 7(5) (2019) 103433. https://doi.org/10.1016/j.jece.2019.103433.

[25] Y. Soni, S. Gupta, C.P. Vinod, Mol. Catal. 511 (2021). https://doi.org/10.1016/j.mcat.2021.111732.

[26] W. Gao, X. Tang, H. Yi, S. Jiang, Q. Yu, X. Xie, R. Zhuang, J. Environ. Sci. 125 (2023) 112–134. https://doi.org/10.1016/j.jes.2021.11.014.

[27] E. Akbay, T.G. Ölmez, Mater. Lett. 215 (2018) 263–267. https://doi.org/10.1016/j.matlet.2017.12.117.

[28] K. Chandra Mouli, S. Mohanty, Y. Hu, A. Dalai, J. Adjaye, Catal. Today 207 (2013) 133–144. https://doi.org/10.1016/j.cattod.2012.07.010.

[29] I.C. Nogueira, L.S. Cavalcante, P.F.S. Pereira, M.M. De Jesus, J.M. Rivas Mercury, N.C. Batista, M.S. Li, E. Longo, J. Appl. Crystallogr. 46(5) (2013) 1434–1446. https://doi.org/10.1107/S0021889813020335.

[30] T. Qiang, Y. Song, J. Zhao, J. Li, J. Alloys Compd. 770 (2019) 792–802. https://doi.org/10.1016/j.jallcom.2018.08.074.

[31] R. Malik, P.S. Rana, V.K. Tomer, V. Chaudhary, S.P. Nehra, S. Duhan, Microporous Mesoporous Mater. 225 (2016) 245–254. https://doi.org/10.1016/j.micromeso.2015.12.013.

[32] P. Tamizhdurai, S. Narayanan, R. Kumaran, V.L. Mangesh, C. Kavitha, N. Vidhya Lakshmi, C. Ragupathi, Z.A. Alothman, M. Ouladsmane, G. Mani, Adv. Powder Technol. 32(11) (2021) 4286–4294. https://doi.org/10.1016/j.apt.2021.09.033.

[33] V.R. Elías, G.O. Ferrero, R.G. Oliveira, G.A. Eimer, Microporous Mesoporous Mater. 236 (2016) 218–227. https://doi.org/10.1016/j.micromeso.2016.09.001.

[34] W. Zhan, J. Yao, Z. Xiao, Y. Guo, Y. Wang, Y. Guo, G. Lu, Microporous Mesoporous Mater. 183 (2014) 150–155. https://doi.org/10.1016/j.micromeso.2013.08.038.

[35] S.B.A. Hamid, N.A. Daud, D.D. Suppiah, W.A. Yehya, P. Sudarsanam, S.K. Bhargava, Polyhedron 120 (2016) 154–161. https://doi.org/10.1016/j.poly.2016.08.027.

[36] M.J. da Silva, L.C. de Andrade Leles, M.G. Teixeira, React. Kinet.Mech.Catal. 131(2) (2020) 875–887. https://doi.org/10.1007/s11144-020-01888-4.

[37] A. Wróblewska, P. Miądlicki, J. Sreńscek-Nazzal, M. Sadłowski, Z.C. Koren, B. Michalkiewicz, Microporous Mesoporous Mater. 258 (2018) 72–82. https://doi.org/10.1016/j.micromeso.2017.09.007.

[38] Y.J. Acosta-Silva, R. Nava, V. Hernández-Morales, S.A. Macías-Sánchez, M.L. Gómez-Herrera, B. Pawelec, Appl. Catal., B. 110 (2011) 108–117. https://doi.org/10.1016/j.apcatb.2011.08.032.

[39] R. Pothu, H. Mitta, R. Boddula, P. Balla, R. Gundeboyina, V. Perugopu, J. Ma, Mater. Sci. Technol. 5 (2022) 391–398. https://doi.org/10.1016/j.mset.2022.09.006.

[40] P.V. Suraja, Z. Yaakob, N.N. Binitha, M.R. Resmi, P.P. Silija, Chem. Eng. J. 176-177 (2011) 265–271. https://doi.org/10.1016/j.cej.2011.05.071.

[41] M.K. Sahu, R.K. Patel, J. Ind. Eng. Chem. 40 (2016) 72–82. https://doi.org/10.1016/j.jiec.2016.06.008.

[42] J.S. DuChene, B.C. Sweeny, A.C. Johnston-Peck, D. Su, E.A. Stach, W.D. Wei, Angew. Chem. Int. Ed. 53(30) (2014) 7887–7891. https://doi.org/10.1002/anie.201404259.

[43] F. Xia, E. Ou, L. Wang, J. Wang, Dyes Pigm. 76(1) (2008) 76–81. https://doi.org/10.1016/j.dyepig.2006.08.008.

[44] L.F. Chen, U. Arellano, J.A. Wang, L.M. Balcázar, R. Sotelo, S. Solis, M. Azomosa, J. González, O.A. González Vargas, Y. Song, J. Liu, X.L. Zhou, Catal. Today 394–396 (2022) 62-80. https://doi.org/10.1016/j.cattod.2021.10.014.

[45] S. Kumaravel, S. Thiripuranthagan, T. Vembuli, E. Erusappan, M. Durai, T. Sureshkumar, M. Durai, Optik 235 (2021) 166599. https://doi.org/10.1016/j.ijleo.2021.166599.

[46] F. Chang, M. Jiao, Q. Xu, B. Deng, and X. Hu, Appl. Surf. Sci. 435 (2018) 708–717. https://doi.org/10.1016/j.apsusc.2017.11.168.

[47] L. Hu, H. Yuan, L. Zou, F. Chen, X. Hu, Appl. Surf. Sci. 355 (2015) 706–715. https://doi.org/10.1016/j.apsusc.2015.04.166.

SEVGI CAN GÖL
ELIF AKBAY

Eskişehir Technical University,
Dept. of Chemical Engineering,
İki Eylül Campus, Eskişehir,
Turkey

NAUČNI RAD

EFEKAT INTERAKCIJE METAL-TITANIUM NA FOTODEGRADACIJU U FOTOKATALIZATORIMA METAL-TITANIUM NANETIM NA SBA-15

Nekoliko prelaznih metala (Fe, Cu, Ni, Cr i Co) je ubačeno u Ti-SBA-15 korišćenjem metoda sinteze u dva koraka. Za karakterizaciju su korišćene analize XRD, SEM-EDX, izoterme adsorpcije-desorpcije N_2, XRF i UV-DRS. Rezultati su potvrdili očuvanje uređene mezoporozne strukture, dobro dispergovanog Ti-metala i poboljšanu apsorpciju svetlosti u poređenju sa Ti-SBA-15. Fotokatalitičke performanse su procenjene u degradaciji metilenskog plavog pod UV svetlom. Rezultati pokazuju da je Co-Ti-SBA-15 pokazao najveću fotokatalitičku aktivnost među pripremljenim fotokatalizatorima za razgradnju metilenskog plavog. Značajno povećanje aktivnosti može se pripisati povećanoj adsorpciji reaktanata mezoporoznom strukturom SBA-15, dobroj distribuciji TiO_2 u porama SBA-15 i povećanoj pokretljivosti prenosa elektrona usled dopinga metala. Pored efikasnosti, Co-Ti-SBA-15 je pogodan katalizator za degradaciju boje, pokazujući dobru stabilnost u degradaciji metilen plavog tokom pet fotokatalitičkih ciklusa bez ikakvog odstupanja strukture.

Ključne reči: prelazni metali, mezoporozni materijal, Ti-SBA-15, fotokatalitička degradacija, ponovna upotreba.

CI&CEQ
Chemical Industry & Chemical Engineering Quarterly

Available online at
Association of the Chemical Engineers of Serbia AChE
www.ache.org.rs/CICEQ

Chem. Ind. Chem. Eng. Q. 29 (4) 291–298 (2023) CI&CEQ

IRENA Z. RAKIĆ[1]
ŽARKO S. KEVREŠAN[2]
RENATA KOVAČ[2]
SNEŽANA Ž. KRAVIĆ[1]
ZORICA SVIRČEV[3]
ANA D. ĐUROVIĆ[1]
ZORICA S. STOJANOVIĆ[1]

BIOACCUMULATION AND BIOSORPTION STUDY OF HEAVY METALS REMOVAL BY CYANOBACTERIA *NOSTOC* SP.

Article Highlights

- The capacity for removing heavy metal ions by cyanobacteria *Nostoc* sp. was evaluated
- Parameter influence on metal removal (concentration of HMs, contact time) was explored
- Biosorption and bioaccumulation processes for metal ion uptake were compared
- The results established a high removal potential of the *Nostoc* sp. for toxic metal ions

Abstract

Nowadays, various industrial and urban activities result in discharging enormous quantities of various pollutants and their accumulation in the environment. Considering that heavy metals in wastewater are a serious threat to the environment and human health and that conventional methods for their removal are not highly efficient, the current study mainly focuses on estimating cyanobacterial capability to accumulate different heavy metals from water and comparing bioaccumulation and biosorption processes. Cyanobacteria Nostoc sp. was used, and five heavy metals were selected for this experiment (Cd^{2+}, Cu^{2+}, Pb^{2+}, Ni^{2+}, Zn^{2+}). Examined concentrations of HMs were 20 mg/dm^3, 80 mg/dm^3, and 200 mg/dm^3 for the bioaccumulation study, while 20 mg/dm^3 and 80 mg/dm^3 of each HMs were used for biosorption experiments. Living cells of Nostoc sp. have the highest affinity for Pb^{2+} (98.15%) and Cu^{2+} (95.14%) removal from the solution by bioaccumulation. During the biosorption process, dried biomass of Nostoc sp., besides Pb^{2+} (92.27%) and Cu^{2+} (96.00%), shows a high affinity for Cd^{2+} (91.00%) removal. Living cyanobacterial cells of Nostoc sp. could accumulate 82% of Zn, while dried biomass adsorbs 87% of Zn^{2+}. Although the highest bioaccumulation of Ni^{2+} was only 38% while using the biosorption process, it was significantly higher (63.80%). These results could provide a preliminary study for further investigation in the direction of the development of immobilized biosorbents which could be used for industrial effluent treatment.

Keywords: bioremediation, cyanobacteria, toxic metals uptake, wastewater.

[1]Faculty of Technology Novi Sad, University of Novi Sad, Novi Sad, Republic of Serbia

[2]Institute of Food Technology, University of Novi Sad, Novi Sad, Republic of Serbia

[3]Faculty of Sciences, Department of Biology and Ecology, University of Novi Sad, Novi Sad, Serbia

SCIENTIFIC PAPER

UDC 628.3/.4.582.232:502.174

During the last few decades, increased industrialization mineral exploitation, and intensive agricultural and urban activities resulted in exacerbated environmental contamination due to the release of an enormous quantity of various pollutants into the environment. Many of the major problems with environmental contamination with pollutants are related to water quality issues [1]. Climate changes will further deteriorate water pollution due to the higher water temperature, potential floods, droughts, etc. [1]. Among the wide diversity of pollutants affecting water resources, heavy metals (HMs) are particularly

Correspondence: Z.S. Stojanović Faculty of Technology, University of Novi Sad, Bulevar cara Lazara 1, Novi Sad, Republic of Serbia.
E-mail: zorica.stojanovic@uns.ac.rs
Paper received: 11 May, 2022
Paper revised: 9 November, 2022
Paper accepted: 26 January, 2023

https://doi.org/10.2298/CICEQ220511002R

concerned, considering their strong toxicity, even at low amounts, due to their accumulative effects [2]. The comprehensive definition of 'heavy metals' is that they are naturally occurring metals having an atomic number higher than 20 and an atomic density greater than 5 g/cm^3 [3]. Some of them are required in low concentration by living organisms due to their important roles in metabolic processes, and in that case, they are called essential elements. However, at higher levels, those metals are very toxic and nonessential HMs, which are non-required even in trace amounts for living organisms. The considerable harmful impacts of HMs on human health and the environment are related to their persistence and tendency to accumulate in living forms due to their non-degradable properties [4]. Chronic exposure to HMs can affect the nervous, respiratory, and reproductive systems, the kidney, liver, and other vital organs [4,5]. Also, some HMs, besides being toxic, show cancerogenic effects; thus, they represent a serious threat to the human population [4,5]. Acute exposure can lead predominantly to the dysfunction of the gastrointestinal, heart, and nervous systems, even though symptoms connected with other organs can also occur [6].

Since environmental contamination by HMs is prevalently caused by anthropological activity, regulations and standards regarding the prevention and control of environmental pollution are became more restrictive in recent years. Regardless of the regulatory restriction, due to the hazardous effects on all living organisms, the imperative should be to limit the discharge of toxicants into the environment. Novel and advanced eco-friendly wastewater treatments are needed to prevent contamination of water resources and to meet stringent environmental regulations regarding industrial discharge limits for heavy and toxic metals. Additionally, while regulation forces it to treat, highly efficient and cost-effective wastewater treatments will enable it to treat and recover more water from the industry from being reused. Numerous treatment processes can remove HMs from wastewater [7]. Various materials have been proposed, including silica gel, activated carbons, cellulose nanomaterials, clay, different polymers, etc. [8–10]. Conventional physicochemical methods for heavy metal removal from polluted water include chemical precipitation, ion exchange, reverse osmosis, oxidation or reduction, filtration, flocculation, evaporation, and electrochemical treatment [11–13]. However, most of those techniques are very expensive and are not acceptable from an ecological aspect either. Namely, those methods release secondary pollutants which negatively affect soil fertility [14]. In addition, most conventional methods are ineffective for a lower concentration of HMs (less than 100 mg/dm^3) [13]. Increased environmental protection awareness has prompted the development of more convenient and eco-friendly technologies which would be suitable to remove pollutants to a level lower than defined by law. Additional advantages of these processes would be the eventual recovery and reuse of metals [15]. Biological methods are alternatives to physicochemical methods, where microorganisms and plants are used for remediation. Biological methods which rely on heavy metal microbe interaction are sustainable and promising remediation techniques that have proven to be very effective for HMs removal from wastewater and are considered environmentally friendly and cost-effective [16,17]. Additional advantages of biological methods are in situ application at the contaminated place, cost efficiency, sorbent regeneration ability, and eco-friendly [18]. The concept will be suited to the sustainable goals of the United Nations.

Biosorption and bioaccumulation are biological methods suitable for heavy metal removal from wastewater [19]. The difference between those two processes is that in the biosorption process, pollutants are bounded on the surface of the cell wall, while in bioaccumulation, they are additionally accumulated inside the cell [15]. Biosorption is a metabolically passive process that occurs naturally in living and dead cells. It is a complicated physicochemical process resembling physisorption, chemisorption, ion exchange, and microprecipitation, but with sorbent material of biological origin called biosorbent [15,18,20]. Based on this fact, it is evident that in comparison with the classical chemisorption process, which includes complexations (encompassing coordination and/or chelation) and chemical binding by various materials, biosorption is a broad umbrella term used for the removal of various materials due to the different attractive forces between the substrate and biosorbent [21]. On the other hand, bioaccumulation is an active metabolic process of pollutants uptake by living cells. In bioaccumulation, the first step is biosorption, and then pollutants are transported inside the cell and accumulated intracellularly through the cell metabolic cycle. This process is driven by energy consumption and only occurs in special biological cells.

Cyanobacteria are photosynthetic prokaryotes widely used in various bioremediation processes of HMs due to their significant biosorption and bioaccumulation abilities [22,23].

They can be found in various environments worldwide but usually in lakes, rivers, and seas. Due to their unique physiological adaptive properties, cyanobacteria can inhabit extreme places like deserts, the Arctic, hot springs, and metal-contaminated territory [24–26]. Cyanobacteria use various mechanisms to

cope with the toxic accumulations of HMs [23,24]. They can synthesize metal-binding proteins (MBPs). The largest group of MBPs are metallothioneins, capable of binding HMs with the thiol group of their cysteine amino acids. Synthesis of metallothioneins increases in response to elevated concentrations of certain metals. Besides, the redox machinery inside the cells, including enzymatic (catalase, peroxidase) and non-enzymatic (glutathione, carotenoids) components, help the cyanobacteria to tolerate HM-induced stress [24]. The biosorption capacity of cyanobacteria is correlated with the high number of functional groups on the cell's surface or around the cell [27–29]. Besides others, extracellular polysaccharides (EPSs) have the main role in the HMs biosorption process of cyanobacteria [23,30]. EPSs mainly comprise heteropolysaccharides with a strong anionic character, sulfate groups, various structural conformations, and amphiphilic behavior [31]. Due to the many negative charges on the external cell layers, EPS-producing cyanobacteria have been considered chelating agents for the positively charged HM ions [30]. By chelating, it is possible to remove positively charged heavy metal ions from water solutions. Besides, the production of EPSs increases as the adaptability of cyanobacteria to cope with harsh unfavorable growth conditions by forming a biofilm on the surfaces [32].

Despite the numerous reports on various metal removal from aqueous solutions by using cyanobacteria, most of the studies carried out have examined the removal of single metal and eventually multi-metals by bioaccumulation or biosorption [28,33,34]. Parallel evaluation of biosorption and bioaccumulation activity for multi-elements is also very poor and is limited to particular cyanobacteria cultures. Therefore, in this study, the utility of cyanobacteria culture *Nostoc* sp. in removing heavy metal ions from the water was examined to determine the potential of the examined culture for the bioremediation of polluted waters. Bioaccumulation and biosorption capacity of culture *Nostoc* sp. were compared for several HMs, including Pb, Cd, Cu, Zn, and Ni.

MATERIALS AND METHODS

Chemicals

All chemicals used throughout the experimental works were of analytical reagent grade if otherwise not specified (Merck, Darmstadt, Germany; Lach-Ner, Brno, Czech Republic; and Sigma Aldrich, St. Louis, MO, USA). The stock solution (1000 mg/dm^3) of each heavy metal used for bioaccumulation and biosorption study was prepared by dissolving an appropriate amount of the adequate salt ($Pb(NO_3)_2$, $CdCl_2{\cdot}2H_2O$, $CuSO_4{\cdot}5H_2O$, $ZnSO_4{\cdot}7H_2O$, and $NiCl_2{\cdot}6H_2O$) in doubly distilled water.

Cultivation of *Nostoc* sp.

Cyanobacterial culture *Nostoc* sp. (IRN 9B) was provided by the LAPER Laboratory, Faculty of Sciences, Department for Biology and Ecology, Novi Sad. Five cm^3 of living inoculum culture with a microbial concentration of 3 g/dm^3 was used to inoculate 0.5 dm^3 cultivation medium. The cyanobacteria were grown in a BG-11 medium [35]. The 30 days cyanobacterial cultures were used for all experiments, and microbial suspension concentration was kept constant at 0.2 g/dm^3 b subsequent dilution with a BG-11 medium. The cell concentration in the suspension was determined by the dry weight as a specific volume of cyanobacterial suspension, after being centrifuged and washed thoroughly with distilled water, was dried in an oven at 105 °C until constant weight. Static cultivation was performed under a light/dark cycle of 12/12 h with moderate light intensity at (25±1) °C. During the cultivation time, all vessels were manually shaken twice daily to avoid the aggregation and to prevent the cells' adherence to the vessel's wall. The position of the vessels was changed every third day to reduce the influence of light.

Before experiments, all laboratory glassware and plastic used in experiments were washed with dilute HNO_3 solution (1:1, v/v) to remove any impurity that may affect heavy metal adsorption, then rinsed with distilled and double-distilled water. Afterward, to prevent any contamination, all instruments and mediums were sterilized at 120 °C for 15 min to prevent contamination.

Bioaccumulation study

In a medium with cyanobacteria (after 30 days of cultivation), a defined volume of the stock solution of heavy metal was added in each vessel to obtain final concentrations of 20 mg/dm^3, 80 mg/dm^3, and 200 mg/dm^3. Prepared mediums rested for exactly 72 h, which was more than ample time for sorption equilibrium. Afterward, they were prepared for analysis of their HMs content. Experiments were done in three replicates for each metal and every concentration. A diluted stock solution of HMs by BG-11 medium at concentrations of 20 mg/dm^3, 80 mg/dm^3, and 200 mg/dm^3 without cyanobacteria were filtered, acidified with cc HCl and analyzed by atomic absorption spectrophotometry (AAS) to control the initial concentration of HMs on the resulting medium.

Additionally, for every group of samples, there were three controls without HMs. After 72 h of

bioaccumulation, 50 cm^3 of controls and all the samples were filtered using qualitative filter paper (Whatman No. 1, Whatman International, Maidstone, UK). Afterward, filtrates were acidified with cc HCl (*Suprapur*, Merck, Darmstadt, Germany) to the final acid concentration of 0.1 mol/dm^3. The concentration of metal was determined in acidified filtrates after eventual subsequent dilution.

Bioaccumulation was expressed as a percentage of accumulated metal compared to initial metal concentration (Eq. 1) as follows:

$$Bioaccumulation(\%) = \frac{C_i - C}{C_i} \cdot 100 \quad (1)$$

where C_i (mg/dm^3) is the initial concentration of added heavy metal, while C (mg/dm^3) is the residual concentration of metal ion after 3 days of bioaccumulation.

Biosorption study

The biomass was collected from the control samples (30 days cyanobacterial cultures) by using centrifugation at 3000 rpm for 10 minutes (MSE Harrier 15/80, Nuaillé, France). After that, cells were air-dried to constant weight and ground to powder using a pestle and mortar. The obtained biomass was kept in the polyethylene bottles in a dark place until used. The biosorption study was performed in a 250 cm^3 conical flask, where 40 mg of cyanobacterial dried biomass was in contact with 40 cm^3 of a solution of specific heavy metal. Examined concentrations of each heavy metal were 20 mg/dm^3 and 80 mg/dm^3. All experiments were done in three replicates for each heavy metal ion and both concentrations. Three control samples were without added biomass for every metal and both concentrations. The experiments were performed at a room temperature of (25±1) °C. Each sample was shaken on a magnetic stirrer at 150 rpm. After 30 minutes, 60 minutes, 90 minutes, and 120 minutes, aliquots of 5 cm^3 were taken and filtered through filter paper. Filtrates were acidified with *suprapur* cc HCl (final concentration 0.1 mol/dm^3). The concentration of metal was determined in acidified filtrates after eventual subsequent dilution.

Biosorption uptake of heavy metals expressed as the amount of metal ions adsorbed per specific amount of biosorbent [36] was calculated by the equation (2):

$$Q\left(\frac{mg}{g}\right) = \frac{V(C_i - C)}{m} \quad (2)$$

where Q (mg/g) is the metal uptake, V (dm^3) is the volume of solution, C_i (mg/dm^3) is the initial metal concentration, C (mg/dm^3) is the residual concentration of metal, and m (g) is the dry weight of biosorbent. Besides the biosorption ability of metal uptake per g of dry matter of biosorbent, the percentage of metal uptake from an initial metal concentration was also calculated.

Metal analysis

The examined HMs' concentration was determined in acidified filtrates and controls using an atomic absorption spectrophotometer ICE3000 (ThermoFisher, China). All parameters for AAS (wavelength, slit, flame stoichiometry) were set following the manufacturer's recommendation. Pb, Cd, Cu, and Zn stock solutions in 2% HNO_3 were purchased from CPA chem (Stara Zagora, Bulgaria), while the Ni stock solution was obtained from Merck (Darmstadt, Germany). The concentrations of certain metals were determined after filtrate dilutions to obtain an optimum concentration range for the atomic absorption spectrometric method. All analyses were performed in triplicate, and the calibration curves used were linear (R = 0.998).

All measurements were performed in appropriate repetitions, as mentioned in the manuscript's main text. Obtained data were summarized, and the results were evaluated with Microsoft Office Excel software (version 2007; Microsoft Corp, Redmond, WA, USA). Standard deviation (StDev) was calculated for all types of experiments based on three repeated results. The calibration curves for AAS were treated by linear regression, and the corresponding results were reported with a 95% confidence level.

RESULTS AND DISCUSSION

Cyanobacteria *Nostoc* sp. was observed for individual bioremediation of Pb^{2+}, Cd^{2+}, Cu^{2+}, Zn^{2+}, and Ni^{2+} from water. The bioaccumulation results after 3 days for all examined metal ions are shown in Figure 1.

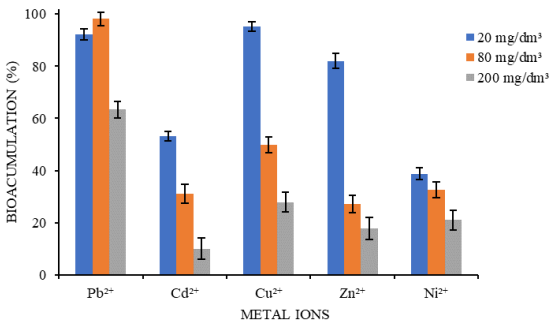

Figure 1. Bioaccumulation of heavy metals in solutions with living cells of Nostoc sp. at 20 mg/dm^3, 80 mg/dm^3 , and 200 mg/dm^3 of heavy metal ions (bars represent the standard deviation).

From Figure 1, it is evident that after 3 days, *Nostoc* sp. accumulated a great amount of Cu^{2+}, Zn^{2+}, and Pb^{2+}. At lower initial concentrations of Cu^{2+} and Zn^{2+} metal ions, the bioaccumulation ability of examined cyanobacteria was more efficient. *Nostoc* sp. removed Cu^{2+} ions up to 95.14% and Zn^{2+} ions up to 82% at a concentration of 20 mg/dm^3 Cu^{2+} and Zn^{2+}, respectively. At an initial concentration of 20 mg/dm^3 Pb^{2+}, *Nostoc* sp. accumulated 92.18% of this heavy metal ion, while bioaccumulation of even 98.15% was obtained when the initial concentration of Pb^{2+} was 80 mg/dm^3. The highest bioaccumulation of Cd^{2+} was 53.27% at a concentration of 20 mg/dm^3, while for the same concentration of Zn^{2+}, the bioaccumulation power of *Nostoc* sp. was 82.06%. As shown in Figure 1, the bioaccumulation efficiency of *Nostoc* sp. for Ni^{2+} removal was the smallest compared to the other HMs. Only 38.75% of Ni^{2+} was removed by *Nostoc* sp. during 3 days of bioaccumulation. From Figure 1, it is evident that metal concentrations significantly influence the biosorption metal uptake. The highest bioaccumulation of Cd^{2+}, Cu^{2+}, Zn^{2+}, and Ni^{2+} was achieved at an initial concentration of 20 mg/dm^3, except for Pb^{2+}, where the highest bioaccumulation was achieved at a concentration of 80 mg/dm^3 (98.15%). It can be explained that during the bioaccumulation, a saturation of *Nostoc* sp. capacity for HMs removal was reached in the case of higher concentrations of Cd^{2+}, Cu^{2+}, Zn^{2+}, and Ni^{2+}, as well as for the highest concentration of Pb^{2+} (200 mg/dm^3) probably due to the disrupted diffusion of the metal ions into the liquid phase. Besides, higher HM concentrations could provoke damage to the cell walls of living cells, so they might lose their binding abilities resulting in remarkably lower bioaccumulation capacity uptake. These results suggest that bioaccumulation of heavy metal ions by *Nostoc* sp. was a very effective remediation process, especially for lower concentrations of metal contaminants.

To calculate the amounts of metal ions adsorbed per specific amount of biosorbent (*Q, mg/g*), residual metal concentrations were measured after 30 minutes, 60 minutes, 90 minutes, and 120 minutes of contact time between metal solution and dried cyanobacterial biomass for all five studied metals. All those results are presented in Table 1. In addition, the dependence of the metal uptake (in %) on the contact time is presented in Figure 2 for all five heavy metal ions.

Table 1. Biosorption uptake of Pb^{2+}, Cd^{2+}, Cu^{2+}, Zn^{2+}, and Ni^{2+} (mg/g) by biomass of Nostoc sp.

Metal ions	*Ci* (mg/dm^3)	$Q_{30\ min}$	$Q_{60\ min}$	$Q_{90\ min}$	$Q_{120\ min}$
		(mg/g)[a]			
Pb	20	12.01±0.98	11.7±1.22	11.56±0.87	11.52±1.05
	80	73.82±3.54	72.6±4.01	71.61±2.82	73.74±4.24
Cd	20	16.6±1.96	17.45±1.57	17.55±1.35	18.2±0.99
	80	70.95±4.54	70.4±3.89	71.95±3.56	64.6±4.53
Cu	20	19.32±2.02	17.89±2.39	17.25±1.80	18.00±1.45
	80	53.1±4.15	60.55±3.87	51.15±3.21	49.05±1.99
Zn	20	16.55±1.56	17.40±0.65	17.35±0.85	16.95±1.20
	80	30.30±3.28	29.00±3.08	30.25±2.22	30.8±2.09
Ni	20	11.84±0.99	11.56±1.76	12.76±1.63	12.32±1.33
	80	22.36±2.56	23.12±1.93	23.44±3.00	19.20±2.15

[a]mean±2StDev, n=3

Biosorption of heavy metals by examined biosorbent depended on the initial concentration and properties of metal ions for most of examined HMs. In the case of Cd^{2+}, initial concentrations of metals did not significantly affect the biosorption uptake of metal. Contact time did not contribute significantly to the Pb^{2+}, Cd^{2+}, Zn^{2+}, and Ni^{2+} uptake by *Nostoc* sp. It can be explained that for all those metals, equilibria between adsorbed and metal remaining in the water were achieved after 30 minutes. Additionally, it can be noticed that the higher biosorption for all the metals was at lower concentrations of 20 mg/dm^{3,} probably as a consequence of cell surface saturation at a higher concentration of HM ions, except for Pb^{2+}, whose biosorption was higher at 80 mg/dm^3 (92.17%).

Biomass of *Nostoc* sp. removed 91% of Cd^{2+} after 120 minutes of contact time, corresponding to the biosorption uptake of 18.2 mg/g of dry biosorbent. Even 96% of Cu^{2+} is removed after the first 30 minutes of the experiment, which respects the biosorption uptake of 19.32 mg/g. Also, there were significant results for Pb^{2+} removal. After only 30 minutes of the experiment, dried *Nostoc* sp. biomass removed up to 73.82 mg/g of Pb^{2+}, which was 92.27%. The highest biosorption for Ni^{2+} was 12.76 mg/g (63.80%) after 90 minutes. Using the biosorption process by dried cyanobacterial biomass sorbent, the uptake of Zn^{2+} was 17.40 mg/g (87%) after 60 minutes of contact time.

Bioaccumulation and biosorption studies evidenced the capability of *Nostoc* sp. for HMs removal. Bioaccumulation is likely to be most effective for Pb^{2+} and Cu^{2+} removal from wastewater, while the biosorption process was very effective for removing Pb^{2+} and Cu^{2+}, Cd^{2+}, and Zn^{2+}. Also, it is worth noting that, compared to the bioaccumulation process, which lasted longer, the biosorption process was more

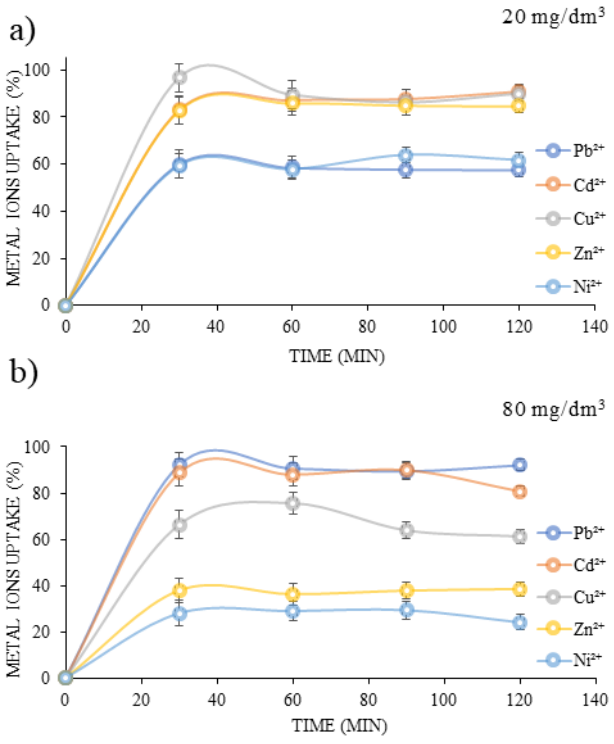

Figure 2. Results of metal ions uptake (%) by dead biomass of Nostoc sp. from water containing HMs ions as a function of contact time. a) 20 mg/dm³ and b) 80 mg/dm³ of metal ions (bars represent the standard deviation).

favorable for removing the studied metal ions due to the very short time. Namely, after 30 minutes, the biosorbent from *Nostoc* sp. could remove more than 90% of Pb^{2+} and Cu^{2+}. On the other hand, results showed that *Nostoc* sp. is not so efficient for decontaminating water resources from Ni^{2+}. It can be explained by the fact for Ni^{2+} removal, either by bioaccumulation or biosorption, initial concentrations were too high.

Many authors reported similar results about heavy metal removal by culture *Nostoc* sp. El-Naggar *et al.* reported that *Nostoc muscorum* removes up to 88% of Cu^{2+}, 82% of Cd^{2+}, 49% of Zn^{2+}, and 44% of Ni^{2+} [37]. Micheletti *et al.* also reported a high affinity of *Nostoc* PCC7936 for Cu^{2+} removal [38]. El-Sheekh *et al.* found that *N. muscorum* accumulates up to 81.8% of Cu^{2+}, 100% of Pb^{2+}, and 33.7% of Co^{2+} [39]. Goswami *et al.* reported that *N. muscorum* accumulates 66% of Zn^{2+} and 71% of Cu^{2+} for 24 h of contact time between cyanobacterial cells and metal solution [40]. Also, Roy *et al.* presented great results of *N. muscorum's* capability to accumulate heavy metals. After 60 h of bioaccumulation, *N. muscorum* removed 96.3% of Pb^{2+}, 96.42% of Cu^{2+}, 80.04% of Cd^{2+}, and 71.3% of Zn^{2+} [41]. Hazarika *et al.* found that *N. muscorum* removed 82% of Cd^{2+} after 30 h at an initial concentration of 5 mg/dm³ and that accumulation at lower initial concentrations of Cd^{2+} was more efficient [42]. Based on the presented results in this work, it is evident that bioaccumulation of observed HMs is more efficient if the initial concentration is lower. Also, in the biosorption experiment, the highest biosorption capacities were at the lowest examined concentration for most metals. It indicated that bioaccumulation and biosorption of HMs by *Nostoc* sp. can be used to remove metal pollutants from wastewater, especially considering that conventional methods for HMs removal from wastewater are ineffective for a lower concentration of HMs.

CONCLUSION

The results of the present study showed that cyanobacteria *Nostoc* sp. possess a high capacity for heavy metal removal from aqueous solution. Both of the used processes, bioaccumulation and biosorption, have shown good uptake capacities for most of the tested heavy metals. Somewhat better HMs uptake from the water was obtained using dead cell *Nostoc* sp. Based on obtained results, it is worth stressing that cyanobacteria represent suitable and promising biosorbents for heavy metal removal from aqueous solutions, which makes them a good candidate as an alternative to conventional methods used for water purification. In addition, biosorption and bioaccumulation techniques are relatively cheap and environmentally friendly bioremediation and wastewater purification processes. Commercial exploitation and application of *Nostoc* sp. cyanobacteria require further investigation in modeling and testing immobilized biomass with industrial effluents.

ACKNOWLEDGMENT

This work was supported by the Ministry of Education, Science and Technological Development of the Republic of Serbia (Project No. 451-03-68/2022-14/200134).

REFERENCES

[1] R. P. Schwarzenbach, T. Egli, T. B. Hofstetter, U. Von Gunten, B. Wehrli, Annu. Rev. Environ. Resour. 35 (2010) 109–136. https://doi.org/10.1146/annurev-environ-100809-125342.

[2] Z. S. Stojanović J.V. Švarc-Gajić, M.Z. Đorđević, N.L. Grahovac, J.R. Vasin, A.D. Đurović, S. Kravić, Hem. Ind. 69 (2015) 185–192. https://doi.org/10.2298/HEMIND131115033S.

[3] H. Ali, E. Khan, Toxicol. Environ. Chem. 100 (2018) 6–19. https://doi.org/10.1080/02772248.2017.1413652.

[4] J. Briffa, E. Sinagra, R. Blundell, Heliyon 6 (2020) e04691.

https://doi.org/10.1016/j.heliyon.2020.e04691.

[5] M. Zaynab, R. Al-Yahyai, A. Ameen, Y. Sharif, L. Ali, M. Fatima, K. A. Khan, S. Li, J. King Saud Univ. - Sci. 34 (2022) 10165. https://doi.org/10.1016/j.jksus.2021.101653.

[6] G.A. Engwa, P.U. Ferdinand, F.N. Nwalo, M.N. Unachukwu, in Poisoning in the Modern World, O. Karcioglu, B. Arslan, Ed., IntechOpen, (2019) 1–23. https://dx.doi.org/DOI: 10.5772/intechopen.82511.

[7] A. Volarić, Z. Svirčev, D. Tamindžija, D. Radnović, Hem. Ind. 75 (2021) 103–115. https://doi.org/10.2298/HEMIND200915010V.

[8] T. Marimuthu, C. Y. Chee, N. M. N. Sulaiman, Int. J. Environ. Sci. Technol. (2022) 3421–3436. https://doi.org/10.1007/s13762-022-04209-5.

[9] A. Gil, L. Santamaría, S.A. Korili, M.A. Vicente, L.V. Barbosa, S.D. de Souza, L. Marçal, E.H. de Faria, K.J. Ciuffi, J. Environ. Chem. Eng. 9 (2021) 105808. https://doi.org/10.1016/j.jece.2021.105808.

[10] D. G. Trikkaliotis, N.M. Ainali, A.K. Tolkou, A.C. Mitropoulos, D.A. Lambropoulou, D.N. Bikiaris, G.Z. Kyzas, Macromol 2, (2022) 403–425. https://doi.org/10.3390/macromol2030026.

[11] E. Remoudaki, A. Hatzikioseyian, P. Kousi, M. Tsezos, Water Res. 37 (2003) 3843–3854. https://doi.org/10.1016/S0043-1354(03)00306-3.

[12] G. Yan, T. Viraraghavan, Bioresour. Technol. 78 (2001) 243–249. https://doi.org/ 10.1016/S0960-8524(01)00020-7.

[13] R. Dixit, Wasiullah, D. Malaviya, K. Pandiyan, U.B. Singh, A. Sahu, R. Shukla, B.P. Singh, J.P. Rai, P.K. Sharma, H. Lade, D. Paul, Sustainability 7 (2015) 2189–2212. https://doi.org/10.3390/su7022189.

[14] U U. Farooq, J.A. Kozinski, M.A. Khan, M. Athar, Bioresour. Technol. 101 (2010) 5043–5053. https://doi.org/10.1016/j.biortech.2010.02.030.

[15] K. Chojnacka, Environ. Int. 36 (2010) 299–307. http://dx.doi.org/10.1016/j.envint.2009.12.001.

[16] Z Z. Rahman, V.P. Singh, Environ. Sci. Pollut. Res. 27 (2020) 27563–27581. https://doi.org/10.1007/s11356-020-08903-0.

[17] A.P.S. Yadav, V. Dwivedi, S. Kumar, A. Kushwaha, L. Goswami, B.S. Reddy, J. Compos. Sci. 5 (2021) 1–18. https://doi.org/10.3390/jcs5010001.

[18] L. Cepoi, L. Rudi, T. Chiriac, S. Codreanu, A. Valuţa, in Cyanobacteria for Bioremediation of Wastewaters, I. Zinicovscaia, L. Cepoi, Ed., Springer International Publishing, Cham, (2016), 45–60. https://doi.org/10.1007/978-3-319-26751-7_5.

[19] J. Kaduková, E. Virčíková, Environ. Int. 31 (2005) 227–232. https://doi.org/10.1016/j.envint.2004.09.020.

[20] A. Robalds, G. M. Naja, M. Klavins, J. Hazard. Mater. 304 (2016) 553–556. https://doi.org/10.1016/j.jhazmat.2015.10.042.

[21] M. Salman, M. Athar, U. Farooq, Rev. Environ. Sci. Biotechnol. 14 (2015) 211–228. https://doi.org/10.1007/s11157-015-9362-x.

[22] A. Al-Amin, F. Parvin, J. Chakraborty, Y. I. Kim, Environ. Technol. Rev. 10 (2021) 44–57. https://doi.org/10.1080/21622515.2020.1869323.

[23] J. Cui, Y. Xie, T. Sun, L. Chen, W. Zhang, Sci. Total Environ. 761 (2021) 144111. https://doi.org/10.1016/j.scitotenv.2020.144111.

[24] H. Chakdar, S. Thapa, A. Srivastava, P. Shukla, J. Hazard. Mater. 424 (2022) 127609. https://doi.org/10.1016/j.jhazmat.2021.127609.

[25] S.B. Hedges, H. Chen, S. Kumar, D.Y-C. Wang, A.S. Thompson, H. Watanabe, BMC Evol. Biol. 4 (2004) Article 44. https://doi.org/doi:10.1186/1471-2148-4-44.

[26] P. Dahech, M. Schlömann, C. Ortiz, J. Appl. Phycol. 33 (2021) 2795–2804. https://doi.org/10.1007/s10811-021-02516-x.

[27] A.M. Abdel-Aty, N.S. Ammar, H.H. Abdel Ghafar, R.K. Ali, J. Adv. Res. 4 (2013) 367–374. http://dx.doi.org/10.1016/j.jare.2012.07.004.

[28] L. Shen, R. Chen, J. Wang, L. Fan, L. Cui, Y. Zhang, J. Cheng, X. Wu, J. Li, W. Zeng, RSC Adv. 11 (2021) 18637–18650. https://doi.org/10.1039/d1ra02366g.

[29] R.I.A. Ahad, S. Goswami, M.B. Syiem, 3 Biotech 7 (2017) 1. https://doi.org/10.1007/s13205-017-0730-9.

[30] R. De Philippis, G. Colica, E. Micheletti, Appl. Microbiol. Biotechnol. 92 (2011) 697–708. https://doi.org/10.1007/s00253-011-3601-z.

[31] S. B. Pereira, A. Sousa, M. Santos, M. Araújo, F. Serôdio, P. Granja, P. Tamagnini, Int. J. Mol. Sci. 20 (2019) 1. 2019, https://doi.org/10.3390/ijms20225693.

[32] S. Rana, L. S. B. Upadhyay, Int. J. Biol. Macromol. 157 (2020) 577–583. https://doi.org/10.1016/j.ijbiomac.2020.04.084.

[33] A.I. Fokina, S.Y. Ogorodnikova, L.I. Domracheva, E.I. Lyalina, E.A. Gornostaeva, T.Y. Ashikhmina, L.V. Kondakova, Eurasian Soil Sci. 50 (2017) 70–77. https://doi.org/10.1134/S106422931611003X.

[34] I I. Zinicovscaia, L. Cepoi, A. Valuta, L. Rudi, O.A. Culicov, M. Vladimirovna, E.I. Kirkesali, S.S. Pavlov, T. Mitina, J. Mater. Sci. Eng. B 4 (2014) 242–247. https://doi.org/10.17265/2161-6221/2014.08.007.

[35] R.Y. Stanier, R. Kunisawa, M. Mandel, G. Cohen-Bazire, Bacteriol. Rev. 35 (1971) 171–205. https://doi.org/10.1128/mmbr.35.2.171-205.1971.

[36] J. Wang, C. Chen, Biotechnol. Adv. 24 (2006) 427–451. https://doi.org/10.1016/j.biotechadv.2006.03.001.

[37] A. H. El-Naggar, H. H. Omar, M. Osman, G. Ismail, Egypt. J. Exp. Biol. 4 (2008) 47–52.

[38] E. Micheletti, G. Colica, C. Viti, P. Tamagnini, R. De Philippis, J. Appl. Microbiol. 105 (2008) 88–94. https://doi.org/10.1111/j.1365-2672.2008.03728.x.

[39] M. M. El-Sheekh, W. A. El-Shouny, M. E. H. Osman, E. W. E. El-Gammal, Environ. Toxicol. Pharmacol. 19 (2005) 357–365. https://doi.org/10.1016/j.etap.2004.09.005.

[40] S. Goswami, O. L. Diengdoh, M. B. Syiem, K. Pakshirajan, M. G. Kiran, Can. J. Microbiol. 61 (2015) 209. https://doi.org/10.1139/cjm-2014-0599.

[41] A.S. Roy, J. Hazarika, N.A. Manikandan, K. Pakshirajan, M.B. Syiem, Appl. Biochem. Biotechnol. 175 (2015) 3863–3874. https://doi.org/10.1007/s12010-015-1553-y.

[42] J. Hazarika, K. Pakshirajan, A. Sinharoy, M.B. Syiem, J. Appl. Phycol. 27 (2015) 1525–1534. https://doi.org/10.1007/s10811-014-0475-3.

IRENA Z. RAKIĆ[1]
ŽARKO S. KEVREŠAN[2]
RENATA KOVAČ[2]
SNEŽANA Ž. KRAVIĆ[1]
ZORICA SVIRČEV[3]
ANA D. ĐUROVIĆ[1]
ZORICA S. STOJANOVIĆ[1]

[1]Tehnološki fakultet Novi Sad, Univerzitet u Novom Sadu, Bulevar cara Lazara 1, 21000 Novi Sad, Srbija

[2]Naučni institut za prehrambene tehnologije, Univerzitet u Novom Sadu, Bulevar cara Lazara 1, 21000 Novi Sad, Srbija

[3]Prirodno-matematički fakultet, Departmant za biologiju i ekologiju, Univerzitet u Novom Sadu, Trg Dositeja Obradovića 3, 21000 Novi Sad, Srbija

NAUČNI RAD

ISPITIVANJE PROCESA BIOSORPCIJE I BIOAKUMULACIJE TEŠKIH METALA PRIMENOM CIJANOBAKTERIJA *NOSTOC* SP.

U današnje vreme različite industrijske i urbane aktivnosti dovode do ispuštanja ogromnih količina raznih zagađujućih materija i njihovog akumuliranja u životnu sredinu. S obzirom da prisustvo teških metala u otpadnoj vodi predstavlja ozbiljan problem po životnu sredinu i ljudsko zdravlje, a i da konvencionalne metode za njihovo uklanjanje nisu efikasne, cilj ovog rada je procena sposobnosti cijanobakterija da uklanjaju različite teške metale iz vode procesima bioakumulacije. i biosorpcije. U ove svrhe su korišćene cianobacterije Nostoc sp. i pet teških metala (Cd^{2+}, Cu^{2+}, Pb^{2+}, Ni^{2+}, Zn^{2+}). Ispitivane koncentracije teških metala su bile 20 mg/dm^3, 80 mg/dm^3 i 200 mg/dm^3 za proces bioakumulacije, dok je za eksperimente biosorpcije korišćeno 20 mg/dm^3 i 80 mg/dm^3 svakog pojedinačnog metala. Žive ćelije Nostoc sp. pokazale su najveći afinitet za uklanjanje Pb^{2+} (98,15%) i Cu^{2+} (95,14%) iz rastvora bioakumulacijom. Tokom procesa biosorpcije, osušena biomasa Nostoc sp., pored Pb^{2+} (92,27%) i Cu^{2+} (96,00%), pokazala je visok afinitet pri uklanjanju Cd^{2+} (91,00%). Žive cijanobakterijske ćelije Nostoc sp. bile su sposobne da akumuliraju 82% Zn^{2+}, dok je osušena biomasa adsorbovala 87% Zn^{2+}. Najveća bioakumulacija Ni^{2+} iznosila je samo 38%, dok je primenom procesa biosorpcije uklanjanje nikla bilo značajno veće (63,80%). Ovi rezultati bi mogli da pruže preliminarnu studiju za dalja istraživanja u pravcu razvoja imobilizovanih biosorbenata koji bi se koristiti za prečišćavanje industrijskih otpadnih voda.

Ključne reči: bioremedijacija, cijanobakterije, teški metali, otpadne vode.

CI&CEQ
Chemical Industry & Chemical Engineering Quarterly

Available online at
Association of the Chemical Engineers of Serbia *AChE*
www.ache.org.rs/CICEQ

Chem. Ind. Chem. Eng. Q. 29 (4) 299–309 (2023) CI&CEQ

MEHMET KALENDER
AYKUT TOPDEMIR

Department of Bioengineering, Fırat University, Elazığ, Turkey

INVESTIGATION OF THE THIN LAYER DRYING OF MICROPROPAGATED *OCIMUM BASILICUM* L: MODELING BY DERIVED EQUATIONS, QUALITY CHARACTERISTICS, AND ENERGY EFFICIENCY

Article Highlights

- Modeling of hot air drying of micropropagated *O. basilicum* L. technique was investigated
- The derived Verma equation was the best model for drying micropropagated *O. basilicum* L. leaves
- Total phenolic, flavonoid contents and antioxidant capacity of the basil samples were typical values
- Stretch bands with alkane, aromatic, and amine/amide were observed in FT-IR spectra
- The energy efficiency analyses showed that the optimum drying temperature was 40 °C.

Abstract

This study presents the modeling of thin layer drying of micropropagated Ocimum basilicum L., some quality characteristics of the dried product, and energy consumption analysis for the dryer used. The experimental drying data obtained from a previous article were used in the statistical analyses. Modeling studies were statistically carried out using the experimental data at a 1 m/s airflow rate and a temperature of 30 °C–50 °C. The statistical analysis showed that the Verma equation was the best-fit model with the lowest chi-square (χ^2) and AIC values at all temperatures studied. From statistical analyses using derived drying models, it was found that the D9 equation having a χ^2 value of 0.0146 and an AIC value of -528.0, was the best model fitting to experimental data. The total phenolic content, flavonoid, and antioxidant capacity of dried basil samples were measured as (2.538 ± 0.029) mg GAE/g, (2.017 ± 0.088) mg quercetin/g, and (2.263 ± 0.001) mmol TEAC/100 g d.w., respectively. From FTIR spectra, dried basil samples had typical functional groups. SEM images showed that a collapse in the surface of the leaves occurred. But, this collapse is not affecting the functional groups on the surface of the leaves. From energy consumption analyses, the optimum drying temperature was found to be 40 °C. The SMER, MER, and SEC values calculated from energy consumption analysis at 40 °C were 0.0043 kg/kWh, 0.0007 kg/h, and 234.81 kWh/kg, respectively.

Keywords: micropropagation, O. basilicum L., thin-layer drying, modeling, characteristic, energy consumption.

SCIENTIFIC PAPER

UDC 66.047:635.71

Correspondence: M. Kalender, Department of Bioengineering, Fırat University, 23100, Elazığ, Turkey.
E-mail: mkalender@firat.edu.tr
Paper received: 22 July, 2022
Paper revised: 5 January, 2022
Paper accepted: 18 February, 2023

https://doi.org/10.2298/CICEQ220722003K

Ocimum basilicum L. (known as basil) is a multipurpose plant belonging to the Lamiaceae family. *O. basilicum* L. having aromatic and essential oil content, grows in Asia's warm, temperate, and tropical regions. It is an attractive and fragrant ornamental plant and a culinary herb [1,2]. Basil can be consumed as a fresh herb with vegetables, poultry, fish, yogurt, salad, or dried form [3,4]. In addition, it can be used to

manufacture perfumes, soaps, cosmetics, and tooth-cleaning products. It is reported that *O. basilicum* L. may be traditionally helpful in treating some diseases such as fever, headache, kidney problems, ulcers, rheumatoid arthritis, and irregular cycles in folk medicine [5]. Also, recent research showed that this plant is a potent antioxidant [6], antiviral [7], and anti-proliferative [8]. There are secondary metabolites such as essential oil, tannins, phenols, flavonoids, anthocyanins, and steroids in the chemical composition of Basil. Also, it contains fat, protein, water, minerals (especially high magnesium, potassium, and iron), and vitamins (especially choline, vitamin C, vitamin E, and vitamin K) [3].

It has been reported that, recently, many medicinal plants used in phytopharmaceutical production have been overexploited and have been exposed to microbial contaminants in their natural habitat [9]. Hence, some biotechnological methods such as callus induction and culture, micropropagation, somatic embryogenesis, and protoplast isolation and culture have been developed to culture plant cells and tissues. [4]. It provides alternatives for propagating valuable and endangered medicinal plants and allows in vitro production of secondary metabolites. Micropropagation is one of the most efficient ways to propagate plants and may significantly increase the production of secondary metabolites. In this way, some selected plant genotypes can be uniform, including in large-scale production [10]. Numerous endangered medicinal and aromatic plant species can be grown using micropropagation regardless of seasonal and climatic conditions [11]. Micropropagation is also used to analyze blooming (by accelerating production) and optimize commercial production to determine the amount of volatile compounds in plant species at different developmental stages [12]. Solid culture media consisting of Murashige-Skoog salts 3% (w/v) sucrose and benzyl adenine (B.A.) are commonly used as growth regulators in micropropagation [4].

Drying is an important stage in many processes used to obtain valuable components from *O. basilicum* L., its dry consumption, and marketing [4]. Due to reducing the water activity in the drying, the microbial growth and the chemical reactions are stopped. However, the drying method and conditions should be chosen appropriately according to the material to be dried. Various drying methods include the sun, convective hot air, microwave, infrared, and freeze. These methods have advantages and disadvantages depending on the process economy (for example, initial investment, operating costs, and energy consumption), environmental contamination, weather uncertainties, and final product quality [13]. Convective hot air dryers are commonly used to dry food and agricultural products because they are independent of weather variations, shortened drying cycles, low nutritional loss, and improved hygiene [14]. Introducing drying kinetics, drying behavior, and energy efficiency is useful in designing the industrial dryer for drying materials. Thus, thin-layer drying models are commonly used to determine drying kinetics and to predict drying behavior and appropriate drying conditions of foods [15,16].

Özcan *et al*. [17] investigated the drying of *O. basilicum* L. using sun and oven drying methods. They found that oven drying is better than sun drying because of the dried product's shorter drying time and good mineral content. Telsfer and Galindo [18] reported that pre-treatment before *O. basilicum* L. drying shortened the drying times by 57% for air drying, 33% for vacuum drying, and 25% for freeze drying. Altay *et al*. [13] determined the drying rate, kinetics, and energy efficiency of *O. basilicum* L. leaves using the sun, freeze, hot air convective, and microwave oven. They indicated that the energy efficiency of hot air convective drying is better than that of freeze drying.

In this paper, modeling of thin layer hot air drying of micropropagated *O. basilicum* L. was statistically carried out using common-known equations. Furthermore, unlike many studies, the derived model equations, simultaneous temperature and time functions, were also used in statistical modeling tests. Finally, this work presents some quality test results of dried *O. basilicum* L. samples and an energy efficiency analysis of the drying process.

MATERIALS AND METHODS

Micropropagation of *O. basilicum* L.

O. basilicum L. seeds were planted in pots for cultivation. Then, grown seedlings were used in micropropagation experiments [19]. *O. basilicum* L. was micropropagated at the plant tissue culture laboratory of the Bioengineering Department of Fırat University (Elazığ in Turkey). The micropropagation process was performed in a Murashige and Skoog (M.S.) medium with a plant growth regulator (PGR) of 0.5 mg/L Kinetin, 0.5 mg/L 2,4-dichlorophenoxyacetic acid, and 0.8% (w/v) plant agar [20]. Seedling stems were collected using a sterile scalpel. They were washed with tap water and soaked in 70% ethanol for 30 seconds before being cultured. Plant explants filtered through ethyl alcohol were alcoholized and moved into a cabinet. They were kept for 5 min in sodium hypochlorite (NaClO) diluted with 50% (v/v) distilled water. Commercial bleach (5%, v/v) was used as sodium hypochlorite. Tween agent (1 drop–2 drops) was added to the plant explants to increase the surface

contact of sodium hypochlorite. The stems of different lengths (1.5 cm–2 cm) were transferred to media containing PGR. The shoots were incubated on rooting media at 3000 lux light for 16 hours and in the dark for eight hours at (24 ± 1) °C every day for four weeks. The rooted plants were gradually adapted to planting and environmental conditions during acclimatization (the final stage of micropropagation). The plants were removed from the rooting media and washed in tap water to purify them from the medium. Peat was used as a planting medium. The peat was sterilized in an autoclave at 121 °C for 15 minutes. Perlite (1:1 ratio) was added to the peat and put into pots. The rooted plants were planted into those pots.

Tray dryer experiments

Tray dryer experiments were carried out in the test setup consisting of a serpentine heater, a fan, a balance, and a computer at the laboratory of the Bioengineering Department of Fırat University [19]. The initial moisture content of the samples was measured using an infrared dryer (Schimadzu MOC63u, Kyoto, Japan). Each experiment involved five grams of *O. basilicum* L. leaf. The experimental studies were performed at 1 m/s air velocity and 30 °C, 40 °C, and 50 °C. The weight of the *O. basilicum* L. samples was measured at 10 minute intervals until the difference between the two values was 0.5%. Time-dependent dry basis moisture contents (w, g moisture/g dry matter) were calculated based on experimental data. The moisture ratio (Eq. 1) was calculated using the moisture and equilibrium moisture content [21,22]:

$$MR = \frac{\omega - \omega_e}{\omega_0 - \omega_e} \quad (1)$$

where *M.R.* is the dimensionless moisture ratio, w is the moisture content (db) at any time, w_e is the equilibrium moisture content, and w_0 is the initial solid moisture content. If the relative humidity of the drying air continuously changes, then the equilibrium moisture content measurement is difficult. In such cases, Eq. 1 can be simplified to the following equation [23,24]:

$$MR = \frac{\omega}{\omega_0} \quad (2)$$

Modeling

The experimental drying data were supplied from a previous article [19]. The moisture ratios were calculated using Eq. 2 and were statistically compared with the model equations (Table 1). The statistical analyses used nonlinear regression and a quasi-Newton optimization routine for parameter estimation (Statistica v.10). Chi-square (χ2), the root mean square (*RMSE*), the mean squared error (*RSS*), and Akaike information criteria (*AIC*) were used to test the model fit statistically in addition to the correlation coefficient (*R*).

Table 1. Mathematical models used to compare the experimental moisture ratio of O. basilicum L. samples statistically.

Model no	Model names	Mathematical expressions	References
1	Newton	$MR = \exp(-kt)$	[25]
2	Page	$MR = \exp(-kt^n)$	[26]
3	Henderson and Pabis	$MR = a\exp(-kt)$	[27]
4	Logarithmic	$MR = a\exp(-kt) + c$	[28]
5	Wang and Singh	$MR = 1 + at + bt^2$	[29]
6	Diffusion	$MR = a\exp(-kt) + (1-a)\exp(-kbt)$	[30]
7	Verma	$MR = a\exp(-kt) + (1-a)\exp(-gt)$	[31]
8	Two-term exponential	$MR = a\exp(-kt) + (1-a)\exp(-kat)$	[32]

$$\chi^2 = \frac{\left(\sum_{i=1}^{N}\left(MR_{\exp,i} - MR_{pred,i}\right)^2\right)}{N-n} \quad (3)$$

$$RMSE = \left[\left(\frac{1}{2}\sum_{i=1}^{N}\left(MR_{\exp,i} - MR_{pred,i}\right)^2\right)\right]^{0.5} \quad (4)$$

$$RSS = \sum_{i=1}^{N}\left(MR_{\exp,i} - MR_{pred,i}\right)^2 \quad (5)$$

$$AIC = -2\ln L + 2p \quad (6)$$

where $MR_{exp,i}$ and $MR_{pred,i}$ are the experimental and calculated moisture ratios, respectively, N is the number of data used in calculations, and n is the number of constants in model equations. In Eq. (6), L and p are the model equations' maximum likelihood and number of parameters [33]. The closer the chi-square (χ^2) or AIC, which is more useful when low data numbers are to zero, the better the fit between experimental and calculated data [34].

Quality tests

In this section, some chemical and physical properties of dried *O. basilicum* L. samples were

determined. For this purpose, total phenolic content, total flavonoid content, and antioxidant capacity values were measured, and the results were reported as means ± standard deviation for triplicate determinations. Also, FTIR and SEM analyses of dried *O. basilicum* L. samples were carried out.

Total phenolic content analysis

The phenolic content was measured using the Folin-Ciocalteu method [35]. According to this method, 300 µl of *O. basilicum L.* callus extract and 1.5 ml of 2 N Folin-Ciocalteu reagent were mixed in glass tubes. After this mixture was left for (1–2) minutes, 1.2 ml of 7.5% sodium carbonate solution was added, mixed in a vortex, and kept in the dark at 25 °C for 90 minutes. Its absorbance was measured at 765 nm against a blank (pure water) in a UV-VIS spectrophotometer (Shimadzu UV-mini-1240, Kyoto, Japan). Total phenol content was given as gallic acid equivalent (GAE) using the gallic acid calibration curve.

Total flavonoid analysis

The methanolic form was used to analyze the total flavonoid content [36]. For this analysis, 1 ml of plant callus extract and 1 ml of 2% $AlCl_3$ solution were mixed. The mixture was kept at room temperature (25 °C) for 10 minutes. The absorbances of the samples were read in a UV-VIS spectrophotometer (Shimadzu UV-mini-1240, Kyoto, Japan) at a wavelength of 394 nm against 2% $AlCl_3$ as a control sample. The flavonoid concentration was calculated by comparing it with the calibration curve of quercetin.

Antioxidant capacity analysis

Dried *O. basilicum L.* samples were subjected to methanol extraction at the solid/solvent ratio of 1:10 (g/mL) using a homogenizer to gain antioxidants in its content. Then, the extract obtained was centrifuged at 7000 rpm for ten minutes. The supernatant was used to determine antioxidant capacity using two common methods (ABTS and DPPH).

ABTS scavenging capacity

The antioxidant capacity of *O. basilicum L.* extracts was measured based on ABTS's radical cation scavenging ability [2,2'- azonobis(3- ethylbenzothiazoline-6-sulfonate)]. At the time of analysis, 1900 µl of diluted ABTS solution and 100 µl of *O. basilicum L.* callus extracts were added to the glass tubes and mixed in a dark room for 1 h. The absorbance of these mixtures was read against a blank (phosphate buffer) in a UV-VIS spectrophotometer (Shimadzu UV-mini-1240, Kyoto, Japan) at 734 nm. The inhibition percent of the ABTS was calculated using the following equation [37,38]. Also, the antioxidant capacity was given as Trolox equivalents antioxidant capacity (mmol TEAC/100 g dry *O. basilicum* L.).

$$ABTS\ \text{inhibition}(\%) = \left(\frac{A_{Control} - A_{Sample}}{A_{Control}}\right) \times 100 \quad (7)$$

DPPH scavenging capacity

The antioxidant capacity was also measured using DPPH [α-Diphenyl-b-picrylhydrazyl] method. For this purpose, DPPH solution (25 mg/L) was prepared in methanol. First, 4 ml of DPPH solution was mixed with 100 µL of *O. basilicum* L. extracts in the test tubes. Then these mixtures were vortexed and then incubated in the dark at 25 °C for 30 minutes. Finally, the absorbance was measured against a blank (methanol) at 517 nm [39]. The inhibition percent of the DPPH was calculated using the following equation:

$$DPPH\ \text{inhibition}(\%) = \left(\frac{A_{Control} - A_{Sample}}{A_{Control}}\right) \times 100 \quad (8)$$

FTIR and SEM analyses

Fourier-transform infrared (FTIR) spectroscopy of the dried *O. basilicum* L. samples was performed by Schimadzu IR Spirit Spectrophotometer QATR-S (Kyoto, Japan) device with a resolution of 4 cm^{-1} and the wave number ranging from 4.000 cm^{-1} to 400 cm^{-1}. In addition, the SEM image of the dried *O. basilicum* L. samples was observed using Carl Zeiss Evo MA10 (USA) device.

The energy efficiency of a hot-air dryer

The energy efficiency of the hot-air drying system was carried out at 1 m/s air velocity and 30 °C, 40 °C, and 50 °C. For this purpose, the specific moisture extraction rate (SMER), the moisture extraction rate (MER), and specific energy consumption (SEC) were calculated using the following Eqs. (9–11) [13]:

$$SMER = \frac{\text{Amount of water removed during drying (kg)}}{\text{Total energy supplied in drying process (kWh)}} \quad (9)$$

$$MER = \frac{\text{Amount of water removed during drying (kg)}}{\text{Drying time (h)}} \quad (10)$$

$$SEC = \frac{\text{Total energy supplied in drying process (kWh)}}{\text{Amount of water removed during drying (kg)}} \quad (11)$$

The total electrical current drawn by the hot-air dryer at a particular airspeed and drying temperature was measured with a DT3266L Clamp Multimeter Voltmeter Ammeter. The voltage, current, and time values were carried out under stable operating conditions of the dryer. As a result, the electrical power(kWh) was calculated as follows: The electrical

energy = current * voltage * time (h).

RESULTS AND DISCUSSION

Grown *O. basilicum* L. plants have soft leaves ranging from light green to dark green, 1 cm–5 cm in length and 1 cm–3 cm in width.

Modeling results based on drying time-dependent equations

The model constants and some statistical parameters of the eight equations used to model the drying of *O. basilicum* L. are given in Table 2. Verma equation (model 4) best fits the experimental moisture ratios at all temperatures. This result is based on having the lowest Chi-square (χ^2) and AIC values [13,23,34]. Page equation (model 2) provided the second-best fit between the experimental and predicted moisture ratios. Altay *et al.* [13] produced *O. basilicum* L using conventional methods and then examined the thin-layer drying of leaves. They found that the modified Henderson and Pabis, logarithmic, and Page equations best represented the sun, freezing, and microwave-convective drying, respectively. This study also employed convective drying. Altay *et al.* [13] did not test the Verma equation. We found that the Page was one of the equations that provided the best fit in drying *O. basilicum* L., which was micropropagated based on modeling. This result is consistent with that of Altay *et al.*

Table 2. The value of constants in model equations and some statistical parameters obtained from statistical analyses for drying O. basilicum L. samples at 1 m/s flow rate and different temperatures.

Model No	k	n	a	b	c	g	RMSE	RSS	χ^2	AIC
					30 °C					
1	0.0047	-	-	-	-	-	0.0913	0.0167	1.915×10^{-4}	-742.775
2	0.0045	1.0106	-	-	-	-	0.0906	0.0164	1.910×10^{-4}	-742.007
3	0.0046	-	0.9813	-	-	-	0.0854	0.0146	1.695×10^{-4}	-176.024
4	Not suitable									
5	-	-	-0.0031	2.360×10^{-6}	-	-	0.3660	0.2679	3.115×10^{-3}	-499.137
6	Not suitable									
7	1.6276	-	0.0225	-	-	0.0046	0.0841	0.0141	1.665×10^{-4}	-752.985
8	Not suitable									
					40 °C					
1	0.0132	-	-	-	-	-	0.0869	0.0151	1.738×10^{-4}	-751.233
2	0.0071	1.1359	-	-	-	-	0.0406	0.0033	3.827×10^{-5}	-881.877
3	0.0137	-	1.0348	-	-	-	0.0779	0.0121	1.409×10^{-4}	-768.445
4	0.0134	-	1.0369	-	-0.0055	-	0.0717	0.0103	1.195×10^{-4}	-780.797
5	Not suitable -									-294.900
6	Not suitable									
7	0.0210	-	-6.8356	-	-	0.0196	0.0345	0.0024	2.806×10^{-5}	-907.868
8	4.0043	-	0.0033	-	-	-	0.0886	0.0157	1.826×10^{-4}	-743.904
					50 °C					
1	0.0237	-	-	-	-	-	0.0233	0.0011	1.246×10^{-5}	-980.465
2	0.0211	1.0291	-	-	-	-	0.0193	0.0007	8.646×10^{-6}	-1011.28
3	0.0238	-	1.0060	-	-	-	0.0227	0.0010	1.193×10^{-5}	-983.267
4	0.0237	-	1.0065	-	-0.0013	-	0.0212	0.0009	1.048×10^{-5}	-992.577
5	Not suitable -									
6	0.0319	-	-1.0409	0.858069	-	-	0.0178	0.0006	7.489×10^{-6}	-1022.80
7	0.0302	-	-3.4147	-	-	0.0285	0.0177	0.0006	7.389×10^{-6}	-1023.97
8	Not suitable									

Figure 1 presents a graph showing the changes in experimental and predicted moisture ratios for the studied models, except for three model equations (Logarithmic, Diffusion, and Two-term exponential) where there is no fit. As seen from Figure 1, Wang and Singh's model amongst studied model equations is a poor fit. But, the fit of four model equations (Newton, Page, Henderson and Pabis, and Verma) is good since the actual and calculated values are on the diagonal. The following equations are time-dependent moisture ratio equations based on the modeling performed using the Verma equation with the highest fit at 30 °C, 40 °C, and 50 °C:

$$MR = 0.0225\exp(-1.6276t) + 0.9775\exp(-0.0046t), \text{ at } 30°C \quad (12)$$

$$MR = 0.0210\exp(-6.8356t) + 0.9790\exp(-0.0196t), \text{ at } 40°C \quad (13)$$

$$MR = 0.0302\exp(-3.4147t) + 0.9698\exp(-0.0285t), \text{ at } 50°C \quad (14)$$

Modeling drying curves using derived models

It is also possible to perform advanced modeling with the thin layer models by expressing the constants in the equations as a function of temperature [40]. The Verma and Page equations were the most suitable models for drying *O. basilicum* L. Table 3 shows the derived Verma and Page model equations defined according to exponent and exponential type

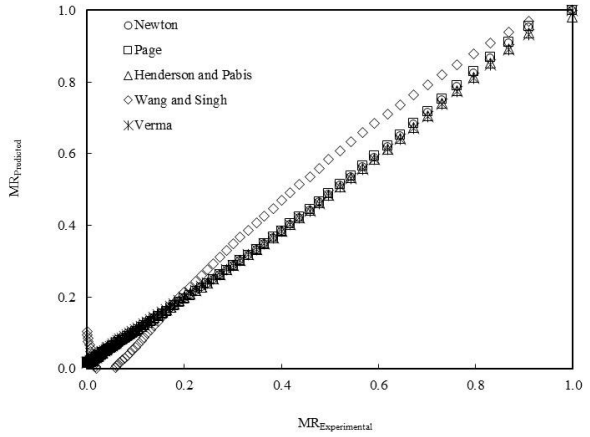

Figure 1. Changing the experimental moisture ratio with the predicted moisture ratio obtained from models used at an air velocity of 1 m/s and 30 °C.

expressions (Eq. 15 and Eq.16).

$$Exponent\ type = aT^{b} \quad (15)$$

$$Exponent\ type = a\exp(bT) \quad (16)$$

Table 4 shows the model constants and some statistical parameters obtained from the statistical analyses with derived model equations for drying *O. basilicum* L. As can be seen in Table 4, Eq. D9 is the model equation having the lowest *RMSE*, *MSE*, χ^2, and *AIC*.

D9 is obtained from the Verma model, and all its constants exponentially depend on temperature. For *O. basilicum* L. drying, the dependence of the moisture ratio (M.R.) on the temperature and the drying time is given in the following equation:

Table 3. Derived model equations obtained from Page and Verma models [40].

Model No	Source model	Mathematical expressions
D1	Page model	$MR = \exp(-k_1 T^{k_2} t)^{n_1 \exp(n_2 T)}$
D2		$MR = \exp(-k_1 T^{k_2} t)^{n_1 T^{n_2}}$
D3		$MR = \exp(-k_1 \exp(k_2 \mathrm{T})\mathrm{t})^{n_1 \exp(n_2 T)}$
D4		$MR = \exp(-k_1 \exp(k_2 T) t)^{n_1 T^{n_2}}$
D5	Verma model	$MR = a_1 T^{a_2} \exp(-(k_1 T^{k_2}) t) + (1 - a_1 T^{a_2}) \exp(-(g_1 \exp(g_2 T)) t)$
D6		$MR = (a_1 \exp(a_2 T)) \exp(-(k_1 T^{k_2}) t) + (1 - a_1 \exp(a_2 T)) \exp(-(g_1 \exp(g_2 T)) t)$
D7		$MR = a_1 T^{a_2} \exp(-(k_1 \exp(k_2 T)) t) + (1 - a_1 T^{a_2}) \exp(-(g_1 \exp(g_2 T)) t)$
D8		$MR = (a_1 \exp(a_2 T)) \exp(-(k_1 \exp(k_2 T)) t) + (1 - a_1 \exp(a_2 T)) \exp(-(g_1 T^{g_2}) t)$
D9		$MR = (a_1 \exp(a_2 T)) \exp(-(k_1 \exp(k_2 T)) t) + (1 - a_1 \exp(a_2 T)) \exp(-(g_1 \exp(g_2 T)) t)$

Table 4. The value of model constants in derived model equations and some statistical parameters obtained from statistical analyses for drying of micropropagated O. basilicum L. samples.

Model No	k_1	k_2	n_1	n_2	a_1	a_2	g_1	g_2	RMSE	RSS	χ^2	AIC
D1	0.0043	0.1950	0.6045	-0.0004	-	-	-	-	1.1797	2.7835	0.0208	-525.791
D2	0.0100	0.0052	0.6349	0.0000	-	-	-	-	1.4165	4.0130	0.0299	-475.669
D3	0.1588	-0.0859	10.9700	-0.0801	-	-	-	-	2.1466	9.2159	0.0688	-361.770
D4	0.0118	-0.0011	0.7906	0.00001	-	-	-	-	1.4101	3.9770	0.0216	-476.904
D5	0.1015	0.0000	-	-	0.1294	0.2599	0.0049	-0.0009	1.1882	2.8237	0.0214	-519.826
D6	-0.0099	0.1366	-	-	0.9537	-0.0284	0.0289	0.1863	1.1788	2.7792	0.0210	-521.999
D7	-0.8269	-0.6509	-	-	0.0520	0.0000	0.0134	-0.0012	1.1882	2.8238	0.0155	-519.822
D8	0.2185	0.1400	-	-	0.8811	-0.5139	0.0088	0.0000	1.2931	3.3441	0.0184	-496.650
D9	0.0099	0.0154	-	-	0.1447	0.0204	0.0107	0.0109	1.1532	2.6597	0.0146	-528.022

$$MR = \left(0.1447\exp\left(0.0204T\right)\right)\exp\left(-\left(0.0099\exp\left(0.0154T\right)\right)t\right) + \left(1-0.1447\exp\left(0.0204T\right)\right)\exp\left(-\left(0.0107\exp\left(0.0016T\right)\right)t\right) \quad (17)$$

Eq. 17 was obtained using D9, best representing the drying phenomenon among the derived models. The change of experimental and predicted according to Eq. 17 moisture ratios with drying time was illustrated in Figure 2. As shown in Figure 2, the developed model at 40 °C and 50 °C is better than at 30 °C. It indicates that the derived models are more effective at higher drying temperatures.

Quality test results

The total phenolic and flavonoid contents of micropropagated *O. basilicum L.* samples were measured as (2.538 ± 0.029) mg GAE/g, and (2.017 ± 0.088) mg quercetin/g, respectively. Mahirah *et al.* [41] determined the total phenolic content of *O. basilicum L.*as 2.61 mg GAE/g. In the literature, it has been shown that the flavonoid content of *O. basilicum L.* varies between 0.7 mg quercetin/g and 4.97 mg quercetin/g [42,43]. ABTS and DPPH inhibition (%) values of dried *O. basilicum L.* sample obtained using the micropropagation technique were 91.44 ± 0.419 and 95.528 ± 0.128 at 40 °C,

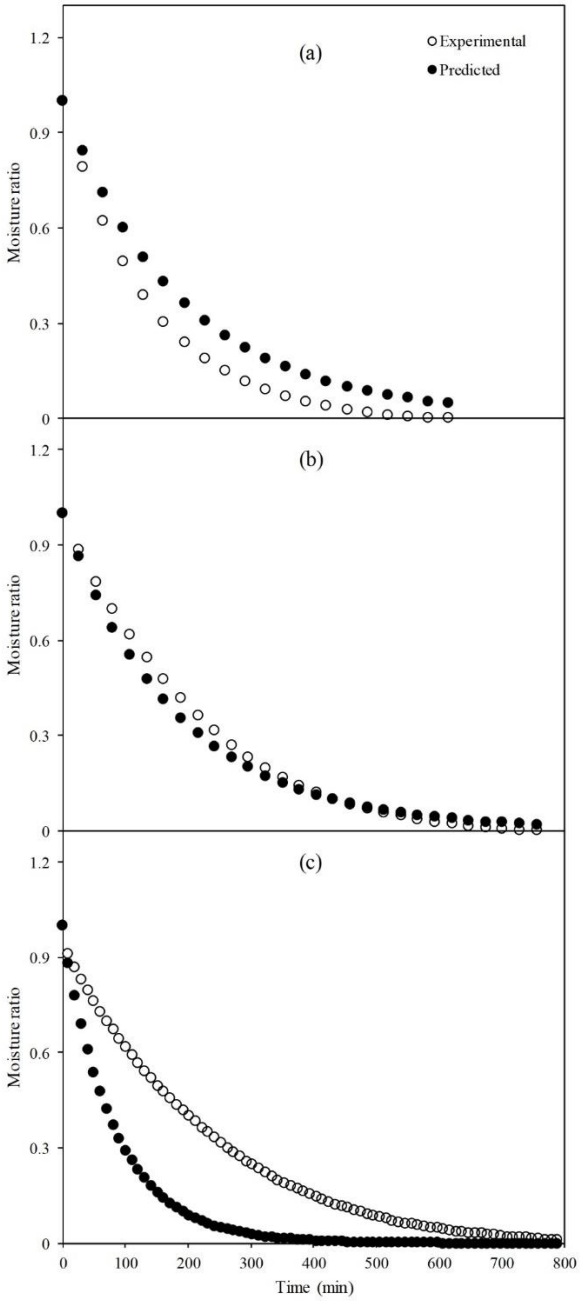

Figure 2. Change of the experimental and calculated (using Eq. 17) moisture ratios with the drying time for drying of O. basilicum L. at (a) 50 °C, (b) 40 °C, and (c) 30 °C.

respectively. In this context, the pictures supplied from ABTS and DPPH inhibition (%) experiments carried out using different *O. basilicum* L. extracts were illustrated in Figure 3. It was found that the inhibition (%) values calculated from both ABTS and DPPH methods were close to each other. Also, the antioxidant capacity of *O. basilicum* L. was calculated at (2.263 ± 0.001) mmol TEAC/100 g d.w. Kwee and Niemeyer [44] measured the antioxidant capacities of 15 basil (*O. basilicum* L.) cultivars. They determined that these capacity values varied from 0.28 mmol/100 g d.w. to 11.5 mmol/100 g d.w. Therefore, the antioxidant capacity of micropropagated *O. basilicum* L. grown agrees with the literature.

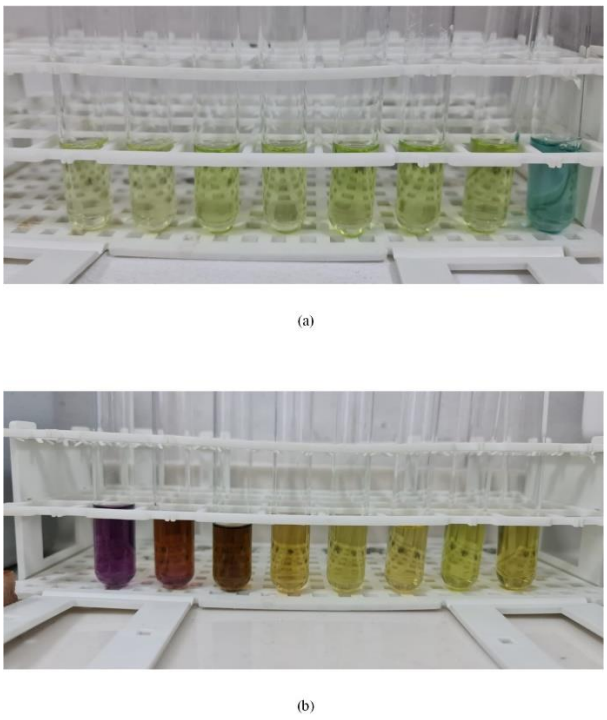

Figure 3. The color change of (a) ABTS and (b) DPPH solutions with the addition of O. basilicum L. extracts at different concentrations.

The FTIR spectra of *O. basilicum* L. samples are illustrated in Figure 4 at the temperature range of 30 °C to 50 °C. As seen in Figure 4, the spectrum peaks were observed in the same wavelength values at all temperatures studied. So, it can be said that no structural decomposition occurred during the drying of the basil samples. It has been observed that alkanes with C-H rock bond and C-H stretch, aromatics with C-C stretch, and amines/amides with N-H stretch are found in the wavelength ranges of 1350 cm^{-1}–1370 cm^{-1}, 2850 cm^{-1}–3000 cm^{-1}, 1585 cm^{-1}–1600 cm^{-1}, 3250 cm^{-1}–3400 cm^{-1}, respectively. These wavelength ranges were supplied from a previous study using *O. basilicum* crude powder [45].

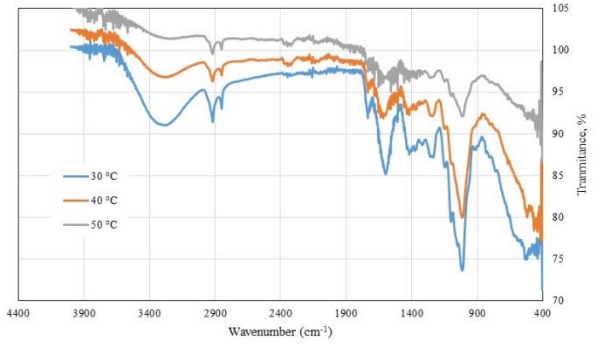

Figure 4. FTIR spectra of micropropagated O. basilicum L. samples in the temperature range of 30°C to 50 °C.

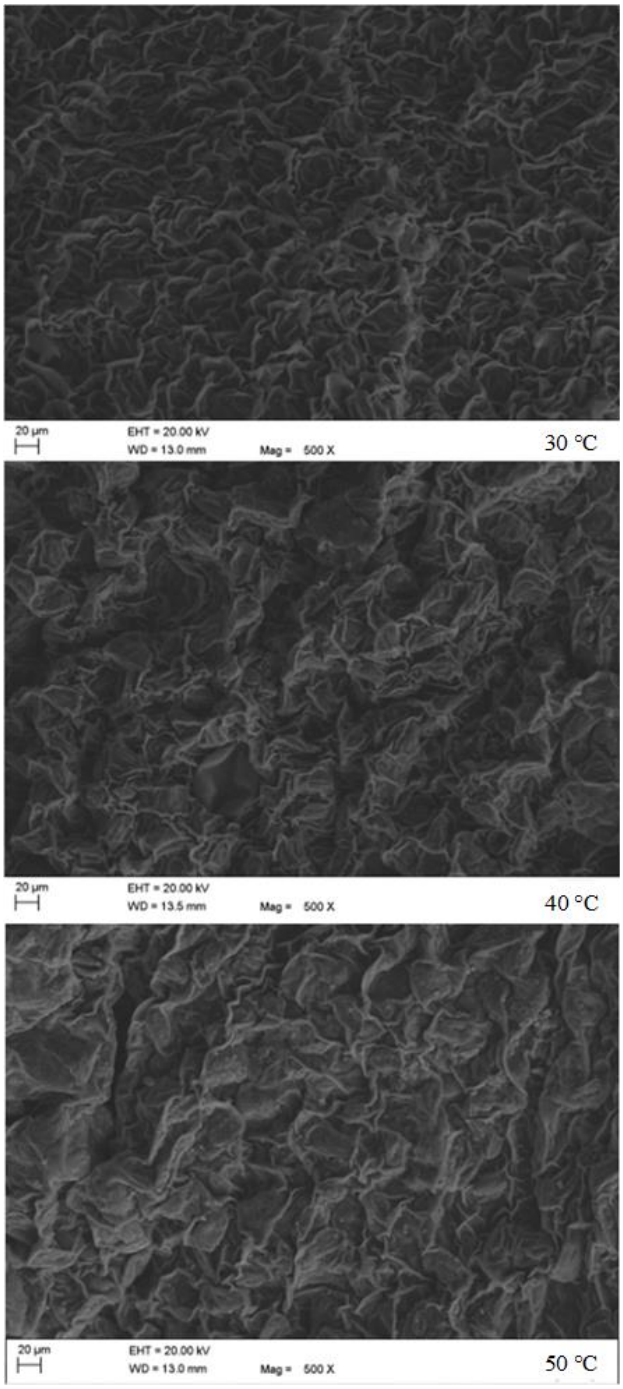

Figure 5. SEM images of micropropagated O. basilicum L. samples in the temperature range of 30°C to 50 °C.

The SEM images of dried *O. basilicum L*. are shown in Figure 5 at different drying temperatures. It is apparent that there are changes on the basil leaves' surface with the drying temperature. A collapse in the leaf's surface has been clearly observed at high temperatures. Similar results were obtained in the previous studies on basil or other plants [18,46,47]. However, FTIR results showed that these changes almost do not affect the functional groups on the surface of the *O. basilicum L*. leaves.

Energy efficiency results

The energy consumption values (SMER, MER, and SEC) of the hot-air dryer used in the micropropagated *O. basilicum L*. drying are given in Table 5. Table 5 shows that the energy consumed by the hot-air drying system used to dry the micropropagated *O. basilicum* L. increased with the drying temperature.

Table 5. The energy efficiency results of micropropagated O. basilicum L. at the 1 m/s air velocity at the studied temperatures.

Temperature (°C)	SMER (kg/kWh)	MER (kg/h)	SEC (kWh/kg)
30	0.0026	0.0003	387.67
40	0.0043	0.0007	234.81
50	0.0033	0.0011	306.61

A similar result for the energy consumption studies of tomato slices drying was obtained [48]. As seen in Table 5, the highest SMER and the lowest SEC values for drying the basil samples were obtained at 40 °C. The higher the SMER value, the better the drying efficiency. On the contrary, low SEC values are desired in the drying processes [13]. Although the energy consumption at 40 °C is lower than at 30 °C, the drying time at 40 °C (4.9 h) is clearly lower than at 30 °C (14.5 h). The electrical power (kW) of a hot air-drying system is multiplied by the drying time (h) to obtain the total energy consumption in SMER and SEC equations (Eq. 9 and Eq.11) [49].

Thus, it was determined that while the SMER value of the drying system at 40 °C is greater than at 30 °C, the SEC value is lower. However, while the SMER value at 50 °C is lower than at 40 °C, the SEC value is greater. It can be considered that this may be due to close drying times at these two temperatures (40 °C and 50 °C) and the higher energy consumption at 50 °C. Pal *et al*. [50] and Mancuhan *et. al*. [51] obtained similar results in their studies on the changes in SMER and SEC values with the drying temperature.

As expected, the MER (the amount of water removed in unit time) for drying micropropagated *O. basilicum* L. drying increases with increasing temperature [13]. The SMER and SEC results clearly show that the drying time affected energy consumption. This result is in agreement with that of a previous study [52]. As a result, it can be said that the best drying condition of micropropagated *O. basilicum L*. at 1 m/s air velocity is 40 °C. As seen in Table 6, the SMER value obtained from the present study agrees with previous studies using convective drying.

Table 6. The comparison of SMER values of this study with previous studies at different drying techniques.

Plant	Drying methods	Drying conditions	SMER (kg/kWh)	References
Orange slices	Convective	50 °C, machine learning	0.0040	[53]
Apple slices	Convective	50 °C	0.0500	[54]
Apple slices	Microwave	360 W	0.5800	[54]
Apple slices	Freeze	-56 °C, 100 kPa	0.0100	[54]
O. basilicum L.*	Microwave	350 W	0.3340	[13]
O. basilicum L.*	Freeze	-48 °C, 13.33 Pa	0.0010	[13]
O. basilicum L.*	Convective	55 °C, 1.5 m/s	0.0080	[13]
O. basilicum L.*	Convective	50 °C, 1.5 m/s	0.0080	[13]
O. basilicum L.*	Convective	45 °C, 1.5 m/s	0.0120	[13]
O. basilicum L. **	Convective	40 °C, 1.5 m/s	0.0043	This study

*grown as conventional; **micropropagated

CONCLUSION

Among the eight drying model equations used in the statistical tests, Verma and Page models having low χ^2 and AIC described efficiently the hot air thin layer drying of *O. basilicum* L. leaves at all temperatures studied. The statistical analyses performed using the derived models obtained from Verma and Page models indicated that the best-representing model was D9 based on the Verma equation. The total phenolic content, total flavonoid content, and antioxidant capacity of *O. basilicum L.* samples were measured as 2.538±0.029 mg GAE/g, 2.017±0.088 mg quercetin/g, and 2.263±0.001 mmol TEAC/100 g d.w., respectively. These characteristic values of the basil sample agreed with those of previous studies in the literature. From FTIR spectra, it has been observed that *O. basilicum L.* samples contain alkanes (C-H rock bond and C-H stretch), aromatics (C-C stretch), and amines/amides (N-H stretch). The bonds and stretching frequencies in the FTIR spectra of dried *O. basilicum L.* samples were typical at all studied temperatures. SEM images showed a collapse on the surface of *O. basilicum L.* leaves at exceptionally high temperatures. But, it can be said that this change does not affect functional groups on the surface of the *O. basilicum L.* leaves. The energy efficiency results determined an optimum temperature point (40 °C) in the SMER, and SEC values change with the drying temperature. As expected, MER values of the drying of the basil leave samples are increasing with the increasing temperature. In future studies, thin-layer drying behavior, final product quality, and energy efficiency of the dryer can be investigated for *O. basilicum* L. grown using different tissue culture techniques.

REFERENCES

[1] J.E. Simon, M.R. Morales, W.B. Phippen, R.F. Vieira, Z. Hao, Basil: A source of aroma compounds and a popular culinary and ornamental herb, Janick J (Ed) ASHS press,Alexandria , VA, (1999), p 499.

[2] K. Carović-Stanko, Z. Liber, V. Besendorfer, B. Javornik, B. Bohanec, I. Kolak, Z. Satovic, Plant Sys Evol Suppl 285 (2010) 13–22. https://doi.org/10.1007/s00606-009-0251-z.

[3] S. Filip, Int. J. Clin. Nutr. Diet 3 (2017) 118. https://doi.org/10.15344/2456-8171/2017/118.

[4] O. Makri, S. Kintzios, J. Herbs, Spices Med. Plants 13 (2008) 123–150. https://doi.org/10.1300/J044v13n03_10.

[5] K. Dhama, K. Sharun, M.B. Gugjoo, R. Tiwari, M. Alagawany, M. Iqbal Yatoo, P. Thakur, H.M. Iqbal, W. Chaicumpa, I. Michalak, Food Rev. Int. (2021) 1–29. https://doi.org/10.1080/87559129.2021.1900230.

[6] C. Jayasinghe, N. Gotoh, T. Aoki, S. Wada, J. Agric. Food Chem. 51 (2003) 4442–4449. https://doi.org/10.1021/jf034269o.

[7] L.C. Chiang, L.T. Ng, P.W. Cheng, W. Chiang, C.C. Lin, Clin. Exp. Pharmacol. Physiol. 32 (2005) 811–816. https://doi.org/10.1111/j.1440-1681.2005.04270.x.

[8] A.B. Mohammed, S. Yagi, T. Tzanova, H. Schohn, H. Abdelgadir, A. Stefanucci, A. Mollica, M.F. Mahomoodally, T.A. Adlan, G. Zengin, S. Afr. J. Bot. 132 (2020) 403–409. https://doi.org/10.1016/j.sajb.2020.06.006.

[9] A. Aye, Y.-D. Jeon, J.-H. Lee, K.-S. Bang, J.-S. Jin, Oriental Pharmacy and Experimental Medicine 19 (2019) 217–226. https://doi.org/10.1007/s13596-019-00372-2.

[10] N.A. Arikat, F.M. Jawad, N.S. Karam, R.A. Shibli, Sci. Hortic. (Amsterdam, Neth.) 100 (2004) 193–202. https://doi.org/10.1016/j.scienta.2003.07.006.

[11] R.L.M. Pierik, In vitro culture of higher plants, Kluwer Academic Publisher,Boston, (1997), p.301. 0792345274.

[12] M. Debnath, C. Malik, P.S. Bisen, Curr. Pharm. Biotechnol. 7 (2006) 33–49. DOI: 10.2174/138920106775789638.

[13] K. Altay, A.A. Hayaloglu, S.N. Dirim, Heat Mass Transfer. 55 (2019) 2173–2184. https://doi.org/10.1007/s00231-019-02570-9.

[14] S. Fang, Z. Wang, X. Hu, Int. J. Food Sci. Technol. 44 (2009) 1818–1824. https://doi.org/10.1111/j.1365-2621.2009.02005.x.

[15] B. Tepe, T.K. Tepe, A. Ekinci, Chem. Ind. Chem. Eng. Q. 22 (2022) 151–159. https://doi.org/10.2298/CICEQ210126026T.

[16] A.C. Ersan, N. Tugrul, Chem. Ind. Chem. Eng. Q. 27 (2021) 319–328. https://doi.org/10.2298/CICEQ201114050E.

[17] M. Özcan, D. Arslan, A. Ünver, J. Food Eng. 69 (2005) 375–379. https://doi.org/10.1016/j.jfoodeng.2004.08.030.

[18] A. Telfser, F.G. Galindo, LWT 99 (2019) 148–155. https://doi.org/10.1016/j.lwt.2018.09.062.

[19] A. Topdemir, J. Fırat Univ. Eng. Sci. 31 (2019) 545–550. https://doi.org/10.35234/fumbd.580212.

[20] T. Murashige, F. Skoog, Physiol. Plant. 15 (1962) 473–497. https://doi.org/10.1111/j.1399-3054.1962.tb08052.x.

[21] C.J. Geankoplis, A.A. Hersel, D.H. Lepek, Transport processes and separation process principles, Prentice Hall Boston, (2018). ISBN 0-13-045253-X.

[22] J.M. Coulson, J.F. Richardson, J.R. Backhurst, J.H. Harker, Chemical Engineering: Fluid flow, heat transfer and mass transfer, Pergamon press,London, (1954). ISBN: 9788181473868.

[23] Z. Erbay, F. Icier, Crit. Rev. Food Sci. Nutr. 50 (2010) 441–

464. https://doi.org/10.1080/10408390802437063.
[24] C. Ertekin, M.Z. Firat, Crit. Rev. Food Sci. Nutr. 57 (2017) 701–717. https://doi.org/10.1080/10408398.2014.910493.
[25] Q. Liu, F. Bakker-Arkema, J. Agric. Eng. Res. 66 (1997) 275–280. https://doi.org/10.1006/jaer.1996.0145.
[26] G.E. Page, Factors Influencing the Maximum Rates of Air Drying Shelled Corn in Thin layers., Master Thesis, Purdue University(1949). 1083231995.
[27] S. Henderson, S. Pabis, J. Agric. Eng. Res. 7 (1962) 85–89.
[28] A. Yağcıoğlu, A. Değirmencioğlu, F. Çağatay, Drying characteristics of laurel leaves under different drying conditions, in 7th Int Congr. Agric. Mechan. Energy, (1999) 565–569.
[29] C. Wang, R. Singh, Trans. Am. Soc. Agric. Eng. 11 (1978) 668–672.
[30] A. Kassem, Comparative studies on thin layer drying models for wheat, 13th Int. Congr. Agric. Eng., (1998) 2–6.
[31] M. Kalender, Constr. Build. Mater. 155 (2017) 947–955. https://doi.org/10.1016/j.conbuildmat.2017.08.094.
[32] L. Bennamoun, L. Kahlerras, F. Michel, L. Courard, T. Salmon, L. Fraikin, A. Belhamri, A. Léonard, Int. J. Energy Eng. 3 (2013) 1–6. https://hdl.handle.net/2268/134220.
[33] H. Akaike, Factor analysis and AIC, Springer,New York, (1987). ISBN 0-387-98355-4.
[34] F.P. Gomes, R. Osvaldo, E.P. Sousa, D.E. de Oliveira, F.R.d. Araújo Neto, Revista Brasileira de Engenharia Agrícola e Ambiental 22 (2018) 499–505. https://doi.org/10.1590/1807-1929/agriambi.v22n12p866-871.
[35] V.L. Singleton, J.A. Rossi, Am. J. Enol. Vitic. 16 (1965) 144–158. DOI: 10.5344/ajev.1965.16.3.144.
[36] J. Lamaison, C. Petitjean-Freytet, A. Carnat, Annales Pharmaceutiques Francaises (France) 48 (1990) 103–108.
[37] N.J. Miller, A.T. Diplock, C.A. Rice-Evans, J. Agric. Food Chem. 43 (1995) 1794–1801. https://doi.org/10.1021/jf00055a009.
[38] Y. Gökçe, H. Kanmaz, B. Er, K. Sahin, A. Hayaloglu, Food Bioscience 43 (2021) 101228. https://doi.org/10.1016/j.fbio.2021.101228.
[39] W. Brand-Williams, M.-E. Cuvelier, C. Berset, LWT-Food science and Technology 28 (1995) 25–30. https://doi.org/10.1016/S0023-6438(95)80008-5.
[40] H. Toğrul, J. Food Eng. 77 (2006) 610–619. https://doi.org/10.1016/j.jfoodeng.2005.07.020.
[41] Y. Siti Mahirah, M. Rabeta, R. Antora, Food Res. 2 (2018) 421–428. https://doi.org/10.26656/fr.2017.2(5).
[42] R. Oonsivilai, P. Prasongdee, Total phenolic contents, total flavonoids and antioxidant activity of Thai basil (*Ocimum basilicum* L.), 5th Int. Conf. Nat. Prod. Health Beauty, Thailand, (2014).
[43] H. Abramovic, V. Abram, A. Cuk, B. Ceh, S. Smole-Mozina, M. Vidmar, M. Pavlovic, N.P. Ulrih, Turk. J. Agric. For. 42 (2018) 185–194. https://doi.org/10.3906/tar-1711-82.
[44] E.M. Kwee, E.D. Niemeyer, Food Chem. 128 (2011) 1044–1050. https://doi.org/10.1016/j.foodchem.2011.04.011.
[45] U. Nazir, S. Javaid, H. Awais, F. Bashir, M. Shahid, Pure Appl. Biol. 10 (2021) 1004–1013. http://dx.doi.org/10.19045/bspab.2021.100105.
[46] A.N. Yousif, C.H. Scaman, T.D. Durance, B. Girard, J. Agric. Food Chem. 47 (1999) 4777–4781. https://doi.org/10.1021/jf990484m.
[47] D. Argyropoulos, J. Müller, Ind. Crops Prod. 52 (2014) 118–124. https://doi.org/10.1016/j.indcrop.2013.10.020.
[48] M. Dorouzi, H. Mortezapour, H.-R. Akhavan, A.G. Moghaddam, Solar Energy 162 (2018) 364–371. https://doi.org/10.1016/j.solener.2018.01.025.
[49] M. Ahmadi, K.R. Gluesenkamp, S. Bigham, Energy Convers. Manage. 230 (2021) 113763. https://doi.org/10.1016/j.enconman.2020.113763.
[50] U. Pal, M.K. Khan, S. Mohanty, Drying Technol. 26 (2008) 1584–1590. https://doi.org/10.1080/07373930802467144.
[51] E. Mancuhan, S. Özen, P. Sayan, S.T. Sargut, Drying Technol. 34 (2016) 1535–1545. https://doi.org/10.1080/07373937.2015.1135340.
[52] A. Tarafdar, N. Jothi, B.P. Kaur, J. Appl. Res. Med. Aromat. Med. Plants 24 (2021) 100306. https://doi.org/10.1016/j.jarmap.2021.100306.
[53] N. Çetin, J. Food Process. Preserv. 46 (2022) e17011. https://doi.org/10.1111/jfpp.17011.
[54] T. Baysal, N. Ozbalta, S. Gokbulut, B. Capar, O. Tastan, G. Gurlek, Therm. Sci. Technol. 35 (2015) 135–144.

MEHMET KALENDER
AYKUT TOPDEMIR

Department of Bioengineering, Fırat University, Elazığ, Turkey

ISTRAŽIVANJE SUŠENJA MIKROPROPAGIRANOG *OCIMUM BASILICUM* L. U TANKOM SLOJU: MODELOVANJE, KARAKTERISTIKE KVALITETA I ENERGETSKA EFIKASNOST

Ova studija prikazuje modelovanje sušenja mikropropagiranog Ocimum basilicum L. u tankom sloju, neke karakteristike kvaliteta osušenog proizvoda i analizu potrošnje energije za korišćenu sušaru. U statističkim analizama korišćeni su eksperimentalni podaci o sušenju dobijeni iz prethodnog članka. Statističko modelovanje je sprovedeno korišćenjem eksperimentalnih podataka pri brzini protoka vazduha od 1 m/s i temperaturi od 30 °C–50 °C. Statistička analiza je pokazala da je Verma jednačina najbolje prilagođen model sa najnižim hi-kvadrat i AIC vrednostima na svim temperaturama. Iz statističkih analiza korišćenjem razvijenih modela sušenja, otkriveno je da je D9 jednačina koja ima vrednost hi-kvadrat od 0,0146 i AIC vrednost od -528,0, najbolje slaganje modela sa eksperimentalnim podacima. Ukupan sadržaj fenola, flavonoida i antioksidativni kapacitet uzoraka osušenog bosiljka izmeren je kao (2,538 ± 0,029) mg GAE/g, (2,017 ± 0,088) mg kvercetina/g i (2,263 ± 0,001) mmol TEAC/100 g, redom. FTIR spektri pokazuju da su uzorci osušenog bosiljka imali tipične funkcionalne grupe. SEM slike su pokazale da je došlo do kolapsa na površini listova. Ali, ovaj kolaps ne utiče na funkcionalne grupe na površini listova. Iz analize potrošnje energije, utvrđeno je da je optimalna temperatura sušenja 40 °C. Vrednosti SMER, MER i SEC izračunate iz analize potrošnje energije na 40 °C bile su 0,0043 kg/kVh, 0,0007 kg/h i 234,81 kVh/kg, redom.

NAUČNI RAD

Ključne reči: mikropropagacija, O. basilicum L., sušenje u tankom sloju, modelovanje, karakteristika, potrošnja energije.

CI&CEQ
Chemical Industry & Chemical Engineering Quarterly

Available online at
Association of the Chemical Engineers of Serbia AChE
www.ache.org.rs/CICEQ

Chem. Ind. Chem. Eng. Q. 29 (4) 311–318 (2023) CI&CEQ

SRINIVASAN APPADURAI[1]
SARAVANAN KANTHASAMY GANESAN[2]
VISWANATHAN RANGASAMY[1]
KARTHIKEYAN SARAVANAN KANAKASABAPATHI[3]

[1]Department of Mechanical Engineering, AVS Engineering College, Salem, Tamil Nadu, India

[2]Department of Mechanical Engineering, Sona College of Technology, Salem, Tamil Nadu, India

[3]Department of Mechanical Engineering, Kongunadu College of Engineering and Technology, Trichy, Tamil Nadu, India

SCIENTIFIC PAPER

UDC 669.248'295:669.18:621

OPTIMIZATION AND EFFECT OF DIELECTRIC FLUID WITH Zr AND Ni ON ELECTRICAL DISCHARGE MACHINING OF DIE STEEL MATERIAL

Article Highlights

- Ni, Zr, and combined Ni with Zr were selected as powder inclusion in dielectric fluid
- Combined Ni and Zr powder mixed with dielectric fluid produced better results
- TOPSIS techniques were effectively performed for multi-objective optimization
- Combined Ni and Zr dielectric conditions greatly reduce micro-cracks and craters

Abstract

This work aims to optimize the machining parameters and study the effect of powder-mixed dielectric fluid on the electrical discharge machining (EDM) process. The TOPSIS method of optimization is adopted to identify the optimal machining parameters. HCHCr die steel is preferred as a machining material. Due to their hard and ductile nature, Ni, Zr, and Ni+Zr were selected as powder inclusion in dielectric fluid. An L9 array Taguchi DOE is preferred to perform the experiments with parameters like peak off time, pulse off time, and pulse current. TOPSIS study revealed that the third level of powder dielectric fluid (Ni+Zr), 7A peak current, 9 µs pulse on time, and 2 µs pulse off time were specified as the optimal condition. Pulse on time (T_{on}) significantly impacted metal removal rate and surface roughness while machining operation on HCHCr die steel. SEM analysis was done to find the effect of powder-mixed dielectric fluid, while EDAX analysis was done to ensure the presence of powder inclusion.

Keywords: optimization, electrical discharge machining, dielectric fluid, nickel, zirconium, metal removal rate, surface roughness.

Electrical discharge machining (EDM) is a promising technique used globally for producing complex shapes in both conductive and non-conductive materials. Recently, its industrial use has been extended to produce intricate profiles and machining high materials [1,2]. However, the minimum machining rate and improper surface finish restrain the use of the EDM process. A powder-mixed machining process is a novel approach to overcome this drawback and to get a high surface finish and improved machining rate [3,4]. Modern researchers explore the performance of powder-mixed dielectric fluid in the EDM process; nickel (Ni) and aluminum oxide are commonly used as dielectric fluid inclusion particles [5]. The performance of powder metallurgy electrodes in EDM of AISI steel was studied with the Taguchi technique. It noted that electrode material, duty cycle, and current had potential effects on machining parameters, and the copper electrode was recommended for a high machining rate [6]. The aluminum powder is added to dielectric fluid during the EDM process. It found that the grain size of

Correspondence: S. Appadurai, Department of Mechanical Engineering, AVS Engineering College, Salem-636003, Tamil Nadu, India.
E-mail: srivankumar14@gmail.com
Paper received: 15 December, 2022
Paper revised: 27 February, 2023
Paper accepted: 9 March, 2023

https://doi.org/10.2298/CICEQ221215005A

the inclusion particle significantly impacts the machining surface, surface finish, and metal removal rate (MRR). Improved MRR was achieved through increased grain size of aluminum powder in dielectric fluid [7]. Using the EDM process, kerosene was used as a dielectric fluid to make a hole. They found that the optimal machining conditions were the 60 V input voltage, 500 Ω resistance, and 1.5 μm/s feed [8].

Based on the experimental research with chromium powder mixed with dielectric fluid in EDM, and observed that MRR considerably increases with high current and duty cycle [9]. Powder concentration has a predominant effect on MRR. Surface modification in die steel material was studied using tungsten powder as dielectric fluid [10]. The research identified low discharge current, short pulse on time, and longer pulse off time as favorable machining conditions. Better MRR and minimum tool wear rate were achieved with abrasive powder mixed EDM [PMEDM] on 6061Al/Al_2O_3P/20p aluminum matrix composite (AMCs) [11]. The effects of graphite powder mixed with dielectric fluid on the machining of titanium alloy with the EDM process were investigated. They stated that increased discharge current and graphite powder concentration enhance the MRR [12]. Tool wear rate (TWR) depends on discharge current and is inversely proportional to mixed powder particle concentration [13]. The GRA (grey relational analysis) method optimized the machining parameters in the powder-mixed EDM process. They concluded that improved surface topography was achieved while machining with powder-mixed dielectric fluid [14]. When machining, adding powder particles in a proper size concentration minimizes surface roughness (Ra). The graphite electrode EDM process provides machining with high MRR and good surface roughness, followed by copper and brass electrodes, while using distilled water as dielectric fluid [15]. Experimental optimization is highly recommended to achieve repeated accurate results. Single-objective and multi-objective optimizations have been most commonly used in recent days. The Taguchi approach effectively optimizes the input parameters on MRR and TWR on powder-mixed EDM [16]. Several researchers used TOPSIS and GRA analysis to optimize the machining parameters [17–20].

The EDM process with powder-mixed dielectric fluid could be successfully carried out. Generally, alumina, Si, Gr, and Cr would be used to include dielectric fluid. Based on a detailed literature study, the EDM process was performed with kerosene dielectric fluid, a reputed powder mixture, and hard steel as work material. Identifying suitable particle inclusion for better machining conditions has scope in the EDM process. Past research reveals that Nickel powder was not used as a powder inclusion in dielectric fluid. This study is aimed to find the influence of Ni (Nickel) and Zr (Zirconium) mixed dielectric fluid in the EDM process. Due to the wide range of applications, HCHCr die steel is preferred as a workpiece. The TOPSIS optimization technique was used to optimize the machining parameters because of its simplicity and ability to provide accurate results.

MATERIALS AND METHODS

In this work, HCHCr steel with dimensions of 147 mm x 45 mm x 10 mm is used as work material. EDM uses a copper electrode with a 12 mm diameter and 20 mm length. The face of the electrode is smoothened before starting the experiments to obtain surface texture in the end face of the electrode. YBI EDM Oil BELDISCHA DCO-1000i was selected as a dielectric fluid due to flexibility and low viscosity [21,22]. Ni and Zr of 300 mesh are used as inclusion particles in dielectric fluid with a size of 46 μm dispersed uniformly. Zr is highly corrosive and resistant to saltwater, acids, alkalis, and other agents. Due to their hard and ductile nature, Ni and Zr were preferred as powder inclusion.

EDM machine (ELEMECH EDM Die Sink (Model S3500) is preferred for the experiments. A separate tank is added to the primary tank to prevent the dielectric powder flow in the main sump. This arrangement is required to avoid powder clogging in the filter system. EDM dielectric fluid circulation was done effectively with the help of the pump, which is kept inside the main tank. An L9 array Taguchi DOE is preferred to perform the experiments with parameters like peak off time, pulse off time, and pulse current. MRR and surface roughness (SR) were the machining output. MRR was calculated by Eq. (1), and the SR value was computed with the Surftest SJ-120 machine. The experimental setup is given in Figure 1. The experimental parameter and L9 DOE run order with measured output are given in Table 1.

$$MRR = \frac{(IM - FM) * 1000}{Density * MT} \quad (1)$$

where IM is the initial mass in g, FM is the final mass in g, and MT is the machining time in min.

RESULTS AND DISCUSSION

Single parameter optimization

Signal-to-noise (S/N) ratio is the first stage in single parameter optimization, and it is performed in Minitab 19. For high MRR, HB is preferred. For SR, a

Table 1. Experimental values.

Exp.No	Powder	I_P (Amp)	T_{on} (µs)	T_{off} (µs)	MRR (mm^3/min)	Ra (µm)
1	Zr	5	9	2	8.931	5.756
2	Zr	6	49	6	10.068	7.771
3	Zr	7	99	9	2.082	3.825
4	Ni	5	49	9	7.271	5.446
5	Ni	6	99	2	5.863	7.273
6	Ni	7	9	6	35.381	5.792
7	Zr + Ni	5	99	6	1.965	3.26
8	Zr + Ni	6	9	9	11.095	5.766
9	Zr + Ni	7	49	2	13.872	9.101

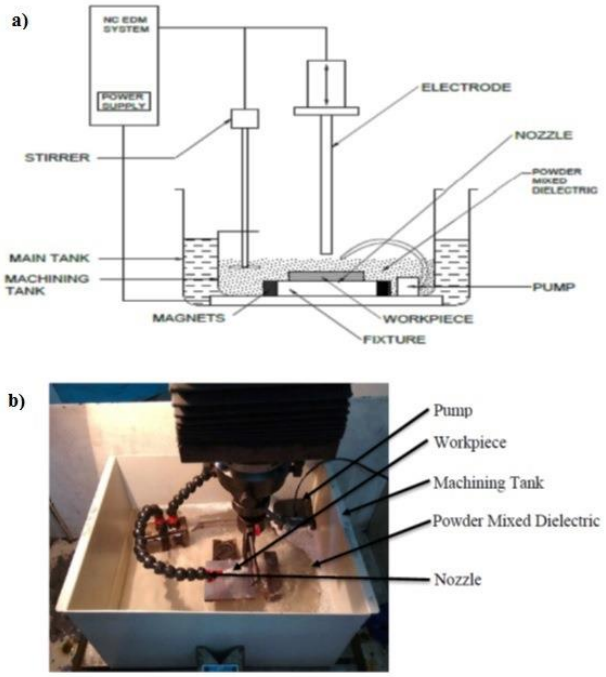

Figure 1. Experimental setup.

minimum value is preferred. The selected equation for the S/N ratio is given in Eqs. (2) and (3), respectively [23]:

$$\text{SB (Smaller the better): } S/N = -10 \log \frac{1}{n}\left[\sum_{i=1}^{n} y_i^2\right] \quad (2)$$

$$\text{HB (Higher the better): } S/N = -10 \log \frac{1}{n}\left[\sum_{i=1}^{n} \frac{1}{y_i^2}\right] \quad (3)$$

where n represents experiments performed and y represents the data.

Table 2 (a) shows that pulse on time greatly impacted MRR. Peak current holds second, followed by pulse off time and powder mixture (T_{on}(µs) > IP(Amp) > T_{off}(µs) > P). Here mixed powder dielectric does induce a high machining rate. The high current and pulse time combination increases the metal melting, producing high MRR [24]. Based on the S/N ratio, Ni mixed dielectric fluids, 6 IP, 9 T_{on}, and 2 T_{off}, were optimal for high machining MRR. High MRR was achieved with a 28.68 mm^3/min rate in optimal machining conditions. The improvement in MRR was found to be 66.32%. (Optimum condition for MRR = $(P)_2$ $(I_P)_2$ $(T_{on})_1$ $(T_{off})_1$).

Table 2. Response for SN Ratios-MRR & Ra.

Level	P	I_P (Amp)	T_{on} (µs)	T_{off} (µs)
a) MRR				
1	18.778	14.039	21.220	19.075
2	15.149	18.775	20.045	16.555
3	16.538	17.651	9.200	14.835
Delta	3.629	4.736	12.020	4.240
Rank	4	2	1	3
b) Ra				
1	-15.74	-13.40	-15.23	-17.21
2	-14.89	-16.75	-17.24	-14.44
3	-14.90	-15.36	-13.05	-13.86
Delta	0.85	3.36	4.19	3.34
Rank	4	2	1	3

Similarly, the response for Ra is presented in Table 2 (b). For better Ra, T_{on} dominates higher compared to other parameters. The dominant factor for Ra is T_{on} (µs) > IP (Amp) > T_{off} (µs) >P. In both MRR and Ra, dielectric fluid does not create a significant impact. Generally, increasing and decreasing on-time pulse duration in EDM enhances the dissolution in both lateral and linear paths, which results in high MRR and Ra. It is acceptable with research work [25]. From response Table 2(b), $(P)_3$ $(I_P)_1$ $(T_{on})_3$ $(T_{off})_3$ were identified as optimal conditions for achieving improvement in Ra. Ni+Zr mixed dielectric fluid is suggested to achieve a high Ra. A rise in T_{on} generally increases the intensity of spark in EDM and induces melting of material boundary much deeper and wider. It also improves Ra. The presence of Ni + Zr in dielectric fluid promotes better Ra due to the formation of fewer surface craters in HCHCr steel [26,27]. For validating the optimal parameters, a confirmation experiment was conducted. At optimal machining condition of $(P)_3$ $(I_P)_1$ $(T_{on})_3$ $(T_{off})_3$, Ra = 1.992 µm was achieved. The confirmation value indicates the improvement of Ra from 5.756 µm to 1.992 µm.

TOPSIS analysis

In modern research, the TOPSIS method is commonly applied to optimize the machining parameters with respect to multi-objective form. The decision matrix is the initial step (step 1) of the TOPSIS method and is represented in r_{ij} (Eq. 4). Secondly, the weightage of every response was done. In the third stage, computing normalized value was based on weightage and decision matrix, given in Eq. (5).

$$r_{ij} = \frac{a_{ij}}{\sqrt{\sum_{i=1}^{m} a_{ij}^2}} \quad (4)$$

$$Vij = Wi \times rij \quad (5)$$

In step 2, the ideal solution was computed. S+ and

S- indicated the ideal solution (positive and negative) given in Eq. (6) and Eq. (7):

$$S_i^+ = \sqrt{\sum_{j=1}^{M}\left(v_{ij} - v_j^+\right)^2} \quad (6)$$

$$S_i^- = \sqrt{\sum_{j=1}^{M}\left(v_{ij} - v_j^-\right)^2} \quad (7)$$

In step 3, CC (closeness coefficient) is computed with the help of Eq. (8).

$$CC_i = \frac{S_i^-}{S_i^+ + S_i^-} \quad (8)$$

The computed CC value and its rank are given in Table 3. Equal weightage was given while computing the normalized MRR and Ra values.

Table 3. Normalized, separation measures and CC.

SN ratio		Normalization		Weighted normalized		Separation measures		CC*	Rank
MRR	Ra	MRR	Ra	MRR	Ra	S+	S-		
19.018	-15.202	0.3103	0.3073	0.1551	0.1536	0.13033	0.15037	0.5357	4
20.059	-17.810	0.3498	0.4148	0.1749	0.2074	0.15169	0.14516	0.4890	5
6.370	-11.653	0.0723	0.2042	0.0362	0.1021	0.23148	0.14083	0.3783	8
17.232	-14.722	0.2526	0.2907	0.1263	0.1454	0.15247	0.13420	0.4681	6
15.362	-17.234	0.2037	0.3882	0.1018	0.1941	0.19698	0.08345	0.2976	9
23.740	-15.257	0.5343	0.3092	0.2672	0.1546	0.06758	0.24920	0.7867	1
5.867	-10.264	0.0683	0.1740	0.0341	0.0870	0.23302	0.15589	0.4008	7
20.903	-15.217	0.3854	0.3078	0.1927	0.1539	0.10008	0.18185	0.6450	2
22.843	-19.182	0.4819	0.4858	0.2409	0.2429	0.15808	0.20681	0.5668	3

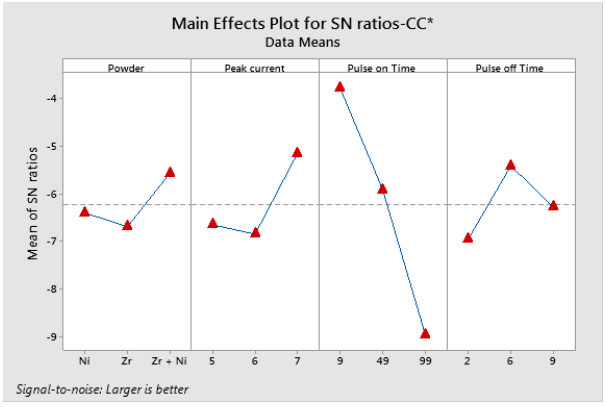

Figure 2. Mean S/N ratio - CC.*

From Table 2, the highest CC value was achieved in experiment run order 6 with the value of 0.7867. Based on the CC value, rank was given to every experiment. A lower CC value was seen in run order 5. Suggest run order with respect to CC is 6>8>9>1>2>4>7>3>5. With respect to the CC value, the mean S/N ratio plot was presented in Figure 2, and it was observed that T_{on} was indicated as the most dominant factor for achieving high MRR and Ra. *Ip* and T_{off} hold the second and third dominant factors for getting high MRR and Ra. An increase in pulse on time induces better machinability due to enhanced spark forming over the work material [28]. Powder mixed dielectric fluid created less effect on MRR and Ra. ANOVA was used to identify each parameter's contribution to machining [29]. Pulse on time holds a contribution rate of 75.47% on MRR and Ra, followed by a peak current of about 10.18%. The effect of mixed dielectric fluid represents less contribution of 4.18% on MRR and Ra. The effectiveness of the experiment was determined by computing the R^2 value [30–35]. From ANOVA, R^2 = 90.63% and R^2(adj) = 81.25%.

A validation experiment is key to the final output [30]. It represents the third level of powder dielectric fluid (Ni+Zr), 7 A peak current, 9 μs pulse on time, and 2 μs pulse off time indicated as the optimal condition. MRR increased from 8.931 mm^3/min to 28.608 mm^3/min, and Ra was enhanced from 5.756 μm to 4.845 μm. Improvement of CC on MRR and Ra was achieved by 35%. The experimental outcomes exposed that the combined (Zr+Ni) powder suspended in dielectric fluid significantly enhanced the MRR and reduced Ra [36,37]. The suspended powders in the dielectric fluid improve the machining performance [38].

SEM analysis

SEM analysis was performed to ensure surface quality in optimal conditions. Based on the multi-objective optimization technique, the third level of the powder dielectric fluid (Ni+Zr), 7 A peak current, 9 μs pulse on time, and 2 μs pulse off time was indicated as the optimal condition. Hence to identify the effect of powder-mixed dielectric fluid, three sets of SEM analyses were performed with varying dielectric fluids. First, Ni mixed, Zr mixed, and Ni+Zr mixed dielectric fluids were used for machining with optimal parameters of 7 A peak current, 9 μs pulse on time, and 2 μs pulse off time, as can be seen in Figure 3a–c, respectively.

SEM analysis shows craters on the machined surface (Figure 3a and Figure 3b) of HCHCr die steel using Zr and Ni mixed dielectric fluids. Debris on the machined surface produced large pits and micro-cracks on HCHCr steel [36,39]. At the same time, the minimum level of micro cracks and craters is noted in Figure 3c. It is due to material deposition from inclusion powders

and dielectric hydrocarbon at optimum pulse on condition. Based on the SEM analysis, machining of HCHCr die steel with Zr+Ni dielectric fluid produced good results at optimal machining conditions of 7 A peak current, 9 µs pulse on time, and 2 µs pulse off time. In addition, EDAX analysis was done to ensure the presence of inclusion particles over the machined surface, represented in Figure 4–6, respectively.

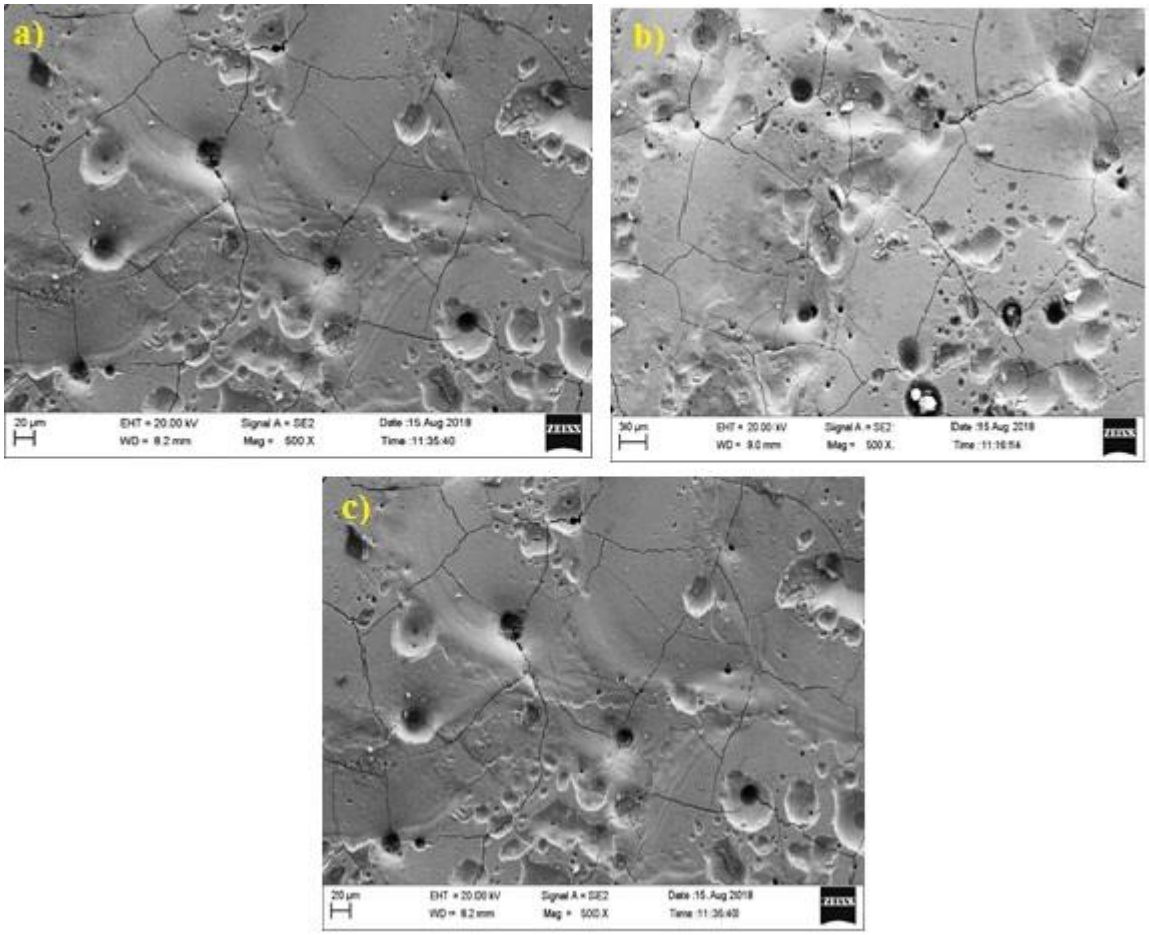

Figure 3. SEM Analysis of machined surface characteristics of powder mixed with dielectric; (a) zirconium, (b) nickel, and (c) combined zirconium and nickel.

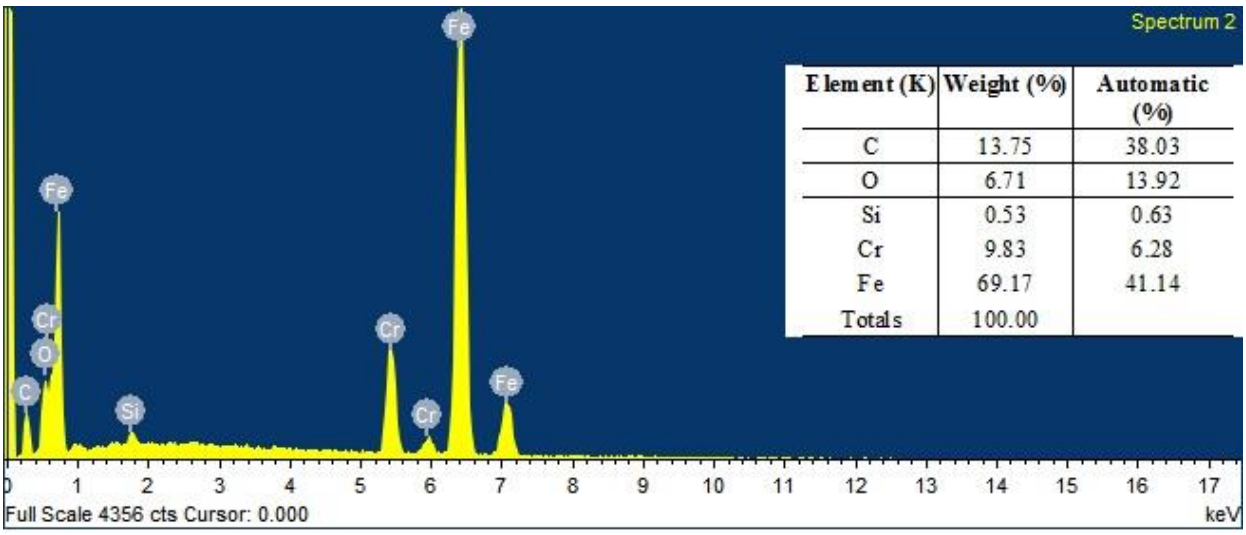

Element (K)	Weight (%)	Automatic (%)
C	13.75	38.03
O	6.71	13.92
Si	0.53	0.63
Cr	9.83	6.28
Fe	69.17	41.14
Totals	100.00	

Figure 4. EDAX analysis of machined surface for zirconium powder mixed in the dielectric.

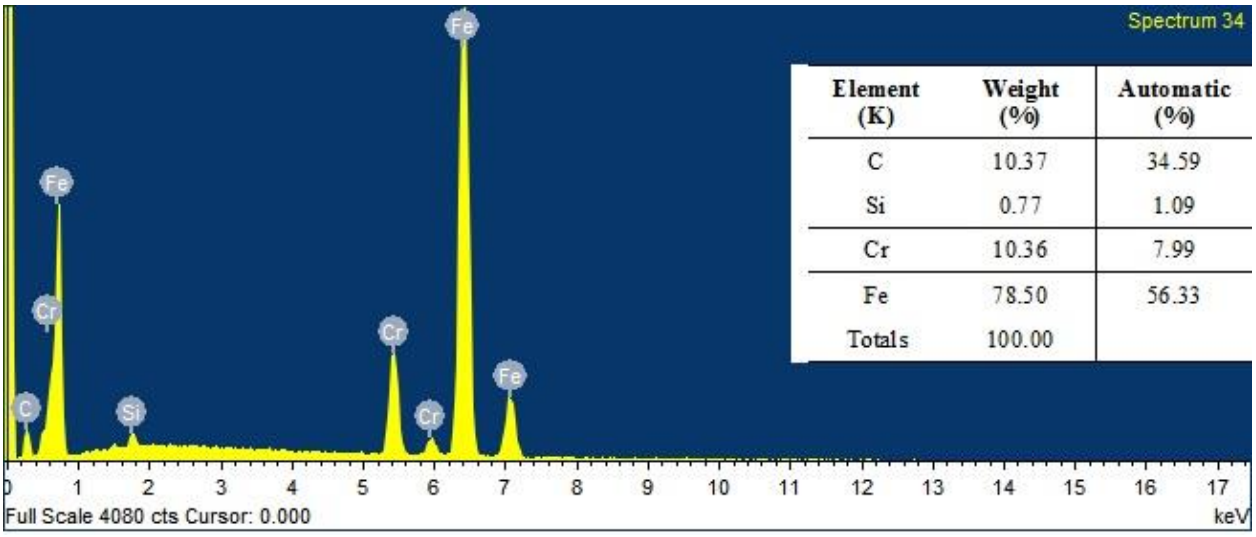

Element (K)	Weight (%)	Automatic (%)
C	10.37	34.59
Si	0.77	1.09
Cr	10.36	7.99
Fe	78.50	56.33
Totals	100.00	

Figure 5. EDAX analysis of machined surface for nickel powder mixed in the dielectric.

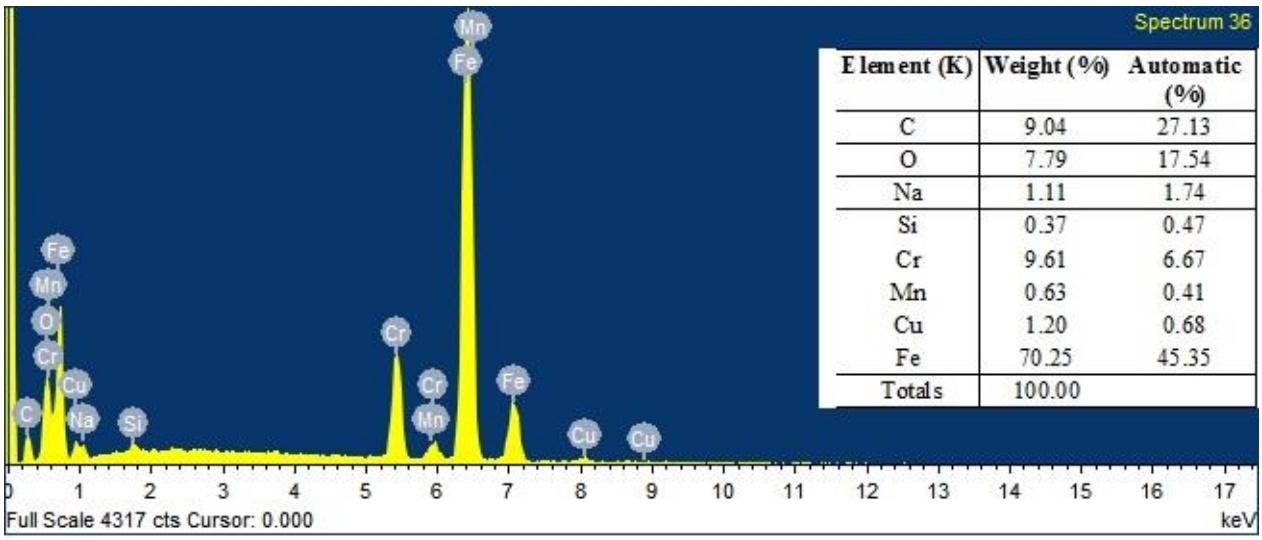

Element (K)	Weight (%)	Automatic (%)
C	9.04	27.13
O	7.79	17.54
Na	1.11	1.74
Si	0.37	0.47
Cr	9.61	6.67
Mn	0.63	0.41
Cu	1.20	0.68
Fe	70.25	45.35
Totals	100.00	

Figure 6. EDAX analysis of machined surface for combined zirconium and nickel powder mixed in the dielectric.

CONCLUSION

Present work was performed to study the effect of dielectric fluid and optimizing machining parameters on machining HCHCr die steel. For improving MRR, $(P)_2$ $(I_P)_2$ $(T_{on})_1$ $(T_{off})_1$, was identified as an optimal condition with respect to the single-objective optimization. For Ra, $(P)_3$ $(I_P)_1$ $(T_{on})_3$ $(T_{off})_3$ was identified as the optimal condition based on single objective optimization. TOPSIS study reveals that the optimal conditions for the third level of powder dielectric fluid are (Ni+Zr), 7 A peak current, 9 µs pulse on time, and 2 µs pulse off time. SEM study ensures a minimum level of micro cracks and craters are noted in Ni+Zr mixed dielectric fluid during optimal machining conditions. The confirmation experiment reveals that MRR improved from 8.931 mm^3/min to 28.608 mm^3/min, and Ra was enhanced from 5.756 µm to 4.845 µm. Improvement of CC on MRR and Ra by 35% and inclusion of material was ensured by the EDAX analysis.

REFERENCES

[1] W.S. Zhao, Q.G. Meng, Z.L. Wang, J. Mat. Process. Technol. 129 (2002) 30–33. https://doi.org/10.1016/S0924-0136(02)00570-8.

[2] P. Pecas, E. Henriques, Int. J. Mach. Tools Manuf. 43 (2003) 1465–1471. https://doi.org/10.1016/S0890-6955(03)00169-X.

[3] K.H. Ho, S.T. Newman, Int. J. Mach. Tools Manuf. 43 (2003) 1287–1300. https://doi.org/10.1016/S0890-6955(03)00162-7.

[4] A.Y. Joshi, A.Y. Joshi, Heliyon 5 (2019) e02963. https://doi.org/10.1016/j.heliyon.2019.e02963.

[5] H.K. Kansal, S. Singh, P. Kumar, J. Mat. Process. Technol. 184 (2007) 32–41.

https://doi.org/10.1016/j.jmatprotec.2006.10.046.

[6] N. Beri, S. Maheshwari, C. Sharma, A. Kumar, Int. J. Mech. Mechatron. Eng. 2 (2008) 225–229. https://doi.org/10.5281/zenodo.1327508.

[7] S. Sharma, A. Kumar, N. Beri, D. Kumar, Int. J. Adv. Eng. Technol. 1 (2010) 13–24. https://www.technicaljournalsonline.com/ijeat/VOL%20I/IJAET%20VOL%20I%20ISSUE%20III%20OCTBER%20DECEMBER%202010/IJAET%20OCT-DEC,2010%20ARTICLE%202.pdf.

[8] J.H. Jung, W.T. Kwon, J. Mech. Sci. Technol. 24 (2010) 1083–1090. https://doi.org/10.1007/s12206-010-0305-8.

[9] K. Ojha, R.K. Garg, K.K. Singh, J. Min. Mat. Charact. Eng. 10 (2011) 1087–1102. https://doi.org/10.4236/jmmce.2011.1011083.

[10] S. Kumar, U. Batra, J. Manuf. Process. 14 (2012) 35–40. https://doi.org/10.1016/j.jmapro.2011.09.002.

[11] S. Singh, M.F. Yeh, (2012). J. Mater. Eng. Perform. 21 (2012) 481–491. https://doi.org/10.1007/s11665-011-9861-z.

[12] M. Kolli, A. Kumar, Eng. Sci. Technol. Int. J. 18 (2015) 524–535. https://doi.org/10.1016/j.jestch.2015.03.009.

[13] M. Kolli, A. Kumar, Int. J. Ind. Eng. Manage. Sci. 4 (2014) 62–67. https://doi.org/10.9756/BIJIEMS.4820.

[14] S. Tripathy, D.K. Tripathy, Eng. Sci. Technol, Int. J. 19 (2016) 62–70. https://doi.org/10.1016/j.jestch.2015.07.010.

[15] M. Patel, G. Chandrashekarappa, S. Kumar, D.Y. Jagadish, Pimenov, K. Giasin, Metals 11 (2021) 419. https://doi.org/10.3390/met11030419.

[16] S. Thamos, S. Ramesh, J. Jeykrishnan, Int. J. of Latest Trends in Eng. Technol. 7 (2016) 61–66. http://dx.doi.org/10.21172/1.73.009.

[17] N. Sivashankar, R. Viswanathan, K. Periasamy, R. Venkatesh, S. Chandrakumar, Mater. Today: Proc. 37 (2021) 214–219. https://doi.org/10.1016/j.matpr.2020.05.033.

[18] A. Kannan, R. Mohan, R. Viswanathan, N. Sivashankar, J. Mat. Res. Technol. 9 (2020) 16529–16540. https://doi.org/10.1016/j.jmrt.2020.11.074.

[19] R. Viswanathan, S. Ramesh, S. Maniraj, V. Subburam, Measurement 159 (2020) 107800. https://doi.org/10.1016/j.measurement.2020.107800.

[20] R. Karthik, R. Viswanathan, J. Balaji, N. Sivashankar, R. Arivazhagan, IOP Conf. Ser.: Mater. Sci. Eng. 1013 (2021) 012005. https://doi.org/10.1088/1757-899X/1013/1/012005.

[21] C. Wang, Z. Qiang, Adv. Mat. Sci. Eng. (2019) 5625360. https://doi.org/10.1155/2019/5625360.

[22] P. Sadagopan, B. Mouliprasanth, Int. J. Adv. Manuf. Technol. 92 (2017) 277–291. https://doi.org/10.1007/s00170-017-0039-1.

[23] P. Suresh, R. Venkatesan, T. Sekar, N. Elango, V. Sathiyamoorthy, J. Mech. Eng. 60 (2014), 656–664. https://doi.org/10.5545/sv-jme.2014.1665.

[24] R. Shinde, N. Patil, D. Raut, R. Pawade, P. Brahmankar, Proc. Int. Conf. Commun. Signal Process. (ICCASP 2016), Atlantis Press (2016), India. https://doi.org/10.2991/iccasp-16.2017.47.

[25] L. Praveen, P. Geeta Krishna, L. Venugopal, N.E.C. Prasad, IOP Conf. Series: Mat. Sci. Eng. 330 (2018) 012083. https://doi.org/10.1088/1757-899X/330/1/012083.

[26] F. Klocke, S. Schneider, L. Ehle, H. Meyer, L. Hensgen, A. Klink, Procedia CIRP, 42 (2016) 580–585. https://doi.org/10.1016/j.procir.2016.02.263.

[27] S. Kang, D. Kim, J. Mech. Sci. Technol. 17 (2003) 1475–1484. https://doi.org/10.1007/BF02982327.

[28] S.H. Aghdeab, A.I. Ahmed, Eng. Technol. J. 34 (2016) 2940–2949. http://dx.doi.org/10.30684/etj.34.15A.14.

[29] N. Pragadish, E. Natarajan, M. Selvam, A. Singh, N. Saravanakumar, Lecture Notes in Mechanical Engineering. Springer, Singapore (2023) 535–546. https://doi.org/10.1007/978-981-19-3053-9_40.

[30] V. Manoharan, S. Tamilperuvalathan, E. Natarajan, P. Ponnusamy, Lecture Notes in Mechanical Engineering, Springer, Singapore (2022) 27–34. https://doi.org/10.1007/978-981-16-4222-7_4.

[31] P. Nagarajan, P.K. Murugesan, E. Natarajan, Medziagotyra 25 (2019) 270–275. https://doi.org/10.5755/j01.ms.25.4.20899.

[32] R. Viswanathan, K.G. Saravanan, J. Balaji, R. Prabu, K. Balasubramani, Mater. Today: Proc. 47 (2021) 4449–4453. https://doi.org/10.1016/j.matpr.2021.05.308.

[33] A. Kanakaraj, R. Mohan, R. Viswanathan, J. Ceram. Process. Res. 23 (2022) 268–277. https://doi.org/10.36410/jcpr.2022.23.3.268.

[34] M. Srinivasan, S. Ramesh, S. Sundaram, R. Viswanathan, J. Ceram. Process. Res. 22 (2021) 345–355. https://doi.org/10.36410/jcpr.2021.22.3.345.

[35] K. Periasamy, N. Sivashankar, R. Viswanathan, J. Balaji, J. Ceram. Process. Res. 23 (2022) 335–343. https://doi.org/10.36410/jcpr.2022.23.3.335.

[36] S. Ramesh, N. Vijayakumar, R. Viswanathan, S. Saravanan, Lecture Notes in Mechanical Engineering, Springer, Singapore (2021) 167–185. https://doi.org/10.1007/978-981-16-2086-7_14.

[37] V. N. Sulakhe, R. Dalu, N. Seth, P. Sharma, N. Sanghai, AIP Conf. Proc. 020021 (2018) 1–9. https://doi.org/10.1063/1.5058258.

[38] E. Natarajan , V. Kaviarasan , W. H. Lim, S. Ramesh, K. Palanikumar , T. Sekar, V. H. Mok, Adv. Mat. Sci. Eng. 3072663 (2022), 1–14. https://doi.org/10.1155/2022/3072663.

[39] P. Nagarajan, P. K. Murugesan, E. Natarajan, Mat. Sci. 25 (2019) 270–275. http://dx.doi.org/10.5755/j01.ms.25.3.20899.

SRINIVASAN APPADURAI[1]
SARAVANAN KANTHASAMY GANESAN[2]
VISWANATHAN RANGASAMY[1]
KARTHIKEYAN SARAVANAN KANAKASABAPATHI[3]

[1]Department of Mechanical Engineering, AVS Engineering College, Salem, Tamil Nadu, India

[2]Department of Mechanical Engineering, Sona College of Technology, Salem, Tamil Nadu, India

[3]Department of Mechanical Engineering, Kongunadu College of Engineering and Technology, Trichy, Tamil Nadu, India

NAUČNI RAD

OPTIMIZACIJA I EFEKAT DIELEKTRIČNE TEČNOSTI SA Zr I Ni NA MAŠINSKU OBRADU ČELIČNOG MATERIJALA ELEKTRIČNIM PRAZNJENJEM

Ovaj rad ima za cilj optimizaciju parametara obrade i proučavanje uticaja dielektrične tečnosti pomešane sa prahom na proces obrade električnim pražnjenjem (EDM). TOPSIS metoda optimizacije je usvojena za identifikaciju optimalnih parametara obrade. HCHCr čelik je poželjniji kao materijal za mašinsku obradu. Zbog svoje tvrde i duktilne prirode, Ni, Zr i Ni+Zr su odabrani kao inkluzioni prahovi u dielektričnoj tečnosti. L9 niz Taguchi plan je poželjniji za izvođenje eksperimenata sa parametrima, kao što su vreme vršnog isključenja, vreme isključenja impulsa i impulsna struja. Studija TOPSIS je otkrila da su treća vrsta praškastog dielektričnog fluida (Ni+Zr), vršna struja od 7 A, vreme uključenog impulsa od 9 µs i vreme isključenog impulsa od 2 µs optimalni uslovi. Impuls vremena značajno je uticao na brzinu uklanjanja metala i hrapavost površine tokom mašinske operacije na HCHCr čeliku. SEM analiza je urađena da bi se utvrdio efekat praha mešanog dielektričnog fluida, dok je EDAX analiza urađena da bi se osiguralo prisustvo inkluzije praha.

Ključne reči: optimizacija, obrada sa električnim pražnjenjem, dielektrični fluid, nikl, cirkonijum, brzina uklanjanja metala, hrapavost površine.

CI&CEQ
Chemical Industry & Chemical Engineering Quarterly

Available online at
Association of the Chemical Engineers of Serbia AChE
www.ache.org.rs/CICEQ

Chem. Ind. Chem. Eng. Q. 29 (4) 319–331 (2023) CI&CEQ

DAYSE MARIA SÁ DA SILVA[1]
JORGE VINÍCIUS FERNANDES LIMA CAVALCANTI[1]
ADALBERTO DO NASCIMENTO FREIRE JÚNIOR[2]
SÉRGIO PERES[2]
MARILEIDE MORAES ALVES[3]
MOHAND BENACHOUR[1]

[1]Departamento de Engenharia Química, Universidade Federal de Pernambuco, Recife-PE, Brazil

[2]Escola Politécnica de Pernambuco, Universidade de Pernambuco, Recife-PE, Brazil

[3]Bragança Campus, Universidade Federal do Pará, Bragança- PA, Brazil

SCIENTIFIC PAPER

UDC 662.767.2:628:597(81)

BIOGAS PRODUCTION AND GREENHOUSE GAS MITIGATION USING FISH WASTE FROM BRAGANÇA/BRAZIL

Article Highlights

- Fish waste from Bragança/Brazil and anaerobic sludge to the production of biogas
- Several inoculum/fish waste ratios were performed to determine the viability of the best condition
- Methane content ranged from 50 to 65%, and its yield varied from 80 to 140 mL·g_{vs}^{-1}
- Estimate of GHG reduction and electrical energy of 1.62x10^3 tons of CO_{2e} and 370 MWh·$year^{-1}$
- Potential electrical energy can supply more than 100 local houses in the circular economy

Abstract

The potential of biogas production using fish waste (FW) and its effect on greenhouse gas (GHG) reduction and energy production were evaluated in this research. FW was co-digested with anaerobic sewage sludge (SS). The FW was collected in Bragança, northern Brazil, where the fish industry is the main activity with an FW production of approximately 9,000 kg·day^{-1}. The experimental part included five SS/FW ratios, and in two experiments, hydrogen was added. The experiments were carried out for 30 days, and the effect on the cumulative biogas and methane yields were analyzed. The GHG reduction was estimated using the amount of FW not discarded in the Bragança open dump, and the electricity generation was calculated using the methane yield. Besides, two kinetic models were performed. The results presented a GHG reduction of 1,619 tons of CO_{2e} and an electricity production of 372 MWh·$year^{-1}$ to 956 MWh·$year^{-1}$. Furthermore, the analysis of variance indicated that the methane production was highly dependent on the SS/FW ratios, which ranged from 76 mL·g_{vs}^{-1} to 138 mL·g_{vs}^{-1}. Finally, this research showed the benefit of using FW to generate biogas and electricity while reducing GHG emissions in a city without energy.

Keywords: biogas, energy, fish waste, greenhouse gases, kinetic models, methane.

The fishing Industry is one of the leading market sectors worldwide, including traditional fishing on open systems and even inland aquaculture operations. The world per capita fish consumption increased from 6.1 kg in 1950 to 20.3 kg in 2016 [1].

In 2014, global fish production was approximately 170 million tons in live weight [2]. Considering 45% of the live weight is waste, the environmental management of fish waste is a worldwide problem [3]. Usually, FW is discarded in landfills, open dumps, or incinerated. However, these methods cause environmental problems, such as groundwater pollution and the emission of toxic gases [4,5].

FW comprises many parts, like the viscera, head, skin, and bones. These sub-products can produce fish sauce, flour, oil and/or food. Besides, FW has great

Correspondence: J.V.F.L. Cavalcanti, Departamento de Engenharia Química, Universidade Federal de Pernambuco, Post-graduation Program in Chemical Engineering - Rua Professor Artur de Sá, s/N, CEP - 50740-521, Recife-PE, Brazil.
E-mail: jorge.cavalc@ufpe.br
Paper received: 14 June, 2022
Paper revised: 6 February, 2023
Paper accepted: 9 March, 2023

https://doi.org/10.2298/CICEQ220614004S

potential for energy production. The renewable energy market suggests that these feedstocks could play a part in the future of biofuels [1,6].

The anaerobic digestion process can be separated into four steps: hydrolysis, acidogenesis, acetogenesis, and methanogenesis. During hydrolysis, the organic material is converted to oligomers by hydrolytic enzymes. Acidogenesis is the step whereby the products from hydrolysis are converted to volatile fatty acids and alcohols by primary fermentative bacteria. In acetogenesis, the different products from acidogenesis are converted by secondary fermentative bacteria to acetate, carbon dioxide, and hydrogen. Finally, in methanogenesis, the hydrogen and carbon dioxide and the syntrophic oxidized acetate are converted into methane [7]. Furthermore, hydrogen gas may be inserted into the anaerobic digestion reactor to enable the methanogenic communities to produce more methane through the biochemical reaction between H_2 and CO_2, augmenting the methane content in the biogas [8].

Anaerobic digestion is one of the alternatives that can be used for energy production. Biogas can be used as fuel in boilers, motor generators, gas turbines, and cogeneration units to produce heat or energy while reducing production costs and adding value to processes and products [9,10,53]. Besides, producing biogas using locally available substrates and renewable resources is an efficient and environmentally friendly technology, reducing GHG emissions and creating a circular economy [11–13]. Unfortunately, when improperly disposed at landfills or open dumps, many substrates, such as FW, may cause a natural emission of GHG (diffuse and unusable) at the landfill site, increasing the GHG emission. However, using this substrate, associated with anaerobic wastewater sludge abundant in Bragança, could be useful for three purposes: mitigating GHG emissions, generating clean energy using biogas as fuel, and producing electrical energy. These three options were evaluated in this paper.

The main objective of this paper was to evaluate biogas production using FW and anaerobic sewage sludge as co-substrates. Five SS/FW ratios were initially used, called experiments A (A_1 to A_5). Subsequently, among the five SS/FW ratios studied, the two best results regarding the methane yield and concentration were used in the experiments using hydrogen. These two new experiments were named experiments B (B_1 and B_2). First, the physical-chemical and microbiological characterization of the SS and FW were determined. Then, the cumulative biogas and methane yields were evaluated, and an analysis of variance was performed to study the process variables to determine the influence of the SS/FW ratios and the digestion time. Next, a kinetic study was performed using the First-order and Gompertz models. Finally, the mitigation of GHG emissions and the production of electrical energy using the Bragança FW were determined.

MATERIALS AND METHODS

Fish waste and SS preparation

The FW was collected in a fish processing plant located in the city of Bragança, state of Pará, northern Brazil, which processes approximately 20,000 kg·day^{-1} of fish, generating 9,000 kg·day^{-1} of FW (45%) [3,14]. Generally, the FW is disposed of in an open dump in this location, emitting GHG as there is no biomass valorization program in this municipality.

The FW consists of viscera, head, skin, and bones from several types of fish species, such as *Epinephelus Marginatus* and *Cynoscion Acoupa* [14]. First, a sample of FW was separated and refrigerated at 5 °C. Then, it was crushed using Trapp TRF 80M crusher and a food processor, Philips-Walita RI7630. The processed waste was a finely divided suspension screened in a 40-mesh screen. Finally, the processed FW was stored in a closed container at -18 °C [15,16]. This reduction in the FW size (pretreatment) was necessary to improve the digestion process, especially the hydrolysis step [49].

It is important to emphasize that the pretreatment and freezing, i.e., the FW conditioning, were necessary to transport the substrate, by plane, from Bragança, in the state of Pará in the Amazon Region, to the Instrumental Chromatography Laboratory (LCI) at the UFPE-DEQ, in the state of Pernambuco, distant 1,530 km, to carry out the anaerobic digestion experiments and analysis. Furthermore, commercially, the FW will be treated on-site as feedstock in a biodigester to produce biogas locally.

The SS was collected from a sanitary sewage treatment plant in Recife, Pernambuco, in northeast Brazil, specifically from a biological digester decanter. The SS samples were collected in 2 L polyethylene flasks, sealed, and refrigerated at 5 °C [10].

Fish waste and SS characterization

The FW and SS were characterized at the LCI-UFPE, following different protocols, indicated in Table 1.

Experimental setup and analytical methods

The anaerobic digestion (AD) experiments were carried out using 50 mL flasks (bench scale biodigester)

Table 1. Main characterizations of fish waste and SS.

Fish Waste		SS	
Moisture	ISO 1442 [36]	Moisture	ISO 1442 [36]
pH	ISO 2917 [37]	pH	ISO 2917 [37]
Salt content	FAO Codex Stan 167 [42]	Conductivity	APHA/SM 2510 [44]
Phosphorus content	ISO 13730 [38]	COD	APHA/SM 5220 [46]
Fat content	ISO 1444 [39]	BOD_5	APHA/SM 5210 [45]
Total solids	APHA/SM 2540 [43]	Total solids	APHA/SM 2540 [43]
Fixed solids	APHA/SM 2540 [43]	Fixed solids	APHA/SM 2540 [43]
Volatile solids	APHA/SM 2540 [43]	Volatile solids	APHA/SM 2540 [43]
Elemental Analysis	ASTM D3176-84 [46]	Elemental Analysis	ASTM D3176-74 [48]
Protein content	ISO 1871 [40]	Anaerobic and aerobic colony-forming units (CFU)	São Paulo [47]
Potassium content	ISO 5310 [41]		

FAO: Food and Agriculture Organization of the United Nations; ISO: International Organization for Standardization; ASTM: American Society for Testing and Materials – standard methods for the ultimate analysis of coal and coke; APHA/SM: American Public Health Association/standard methods; São Paulo Government - Secretary of agriculture - Normative Instruction n° 62.

with an adequate volume of 30 mL and a headspace of 20 mL, airtight closed by a rubber septum and aluminum seal. In each flask, the needle of a 60 mL syringe was inserted through the septum to enable the measurement of the biogas yield by the volume of the displaced plunger, as shown in Figure 1. The biogas yields were determined daily.

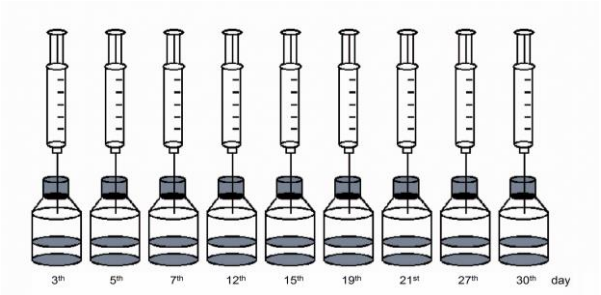

Figure 1. Anaerobic digestion experimental setup - 50 mL flasks and 60 mL syringe.

Five experiments (A1 to A5) were initially performed with five different SS/FW ratios. For example, experiment A_1 used 1.00 g of SS, 9.00 g of FW (SS/FW ratio of 0.11 $g.g^{-1}$), and 20.00 g of water. The same composition was used in 18 flasks (9 flasks in duplicate).

The biogas composition and the substrate pH of each flask pair were analyzed on days 3rd, 5th, 7th, 12th, 15th, 18th, 21st, 27th, and 30th. The methane, carbon dioxide, and hydrogen contents were determined by gas chromatography. To obtain the gas samples for each flask and to inject the biogas samples in the GC, 1000 μL gastight syringe was used. Finally, carefully, upon the internal pressure removal, the flask pair were opened to determine their pH. The other pairs of flasks (digesters), experiments A_2 to A_5, followed the same procedure, and they were analyzed on the predetermined days to conclude the AD experiments and pH analyses. The SS/FW ratios were:

A_2 = 2.15g/8.00g (0.27 $g \cdot g^{-1}$),

A_3 = 3.00g/7.00g (0.43 $g \cdot g^{-1}$),

A_4 = 8.25g/1.75g (4.71 $g \cdot g^{-1}$) and

A_5 = 9.00g/1.00g (9.00 $g \cdot g^{-1}$).

These SS/FW ratios were based on the research found in the literature, such as 10.0 $g.g^{-1}$ and 6.7 $g.g^{-1}$, respectively [16,32]. As the best results were obtained on experiments A_4 and A_5, the same ratios were used in the same conditions. However, on the 7th and 18th days, 0.16 mmol of hydrogen was injected in the digesters, using a 5000 μL gastight syringe, through the rubber septum (with a very fine needle). These two new experiments were named B_1 and B_2. Hydrogen injection aimed to verify how hydrogen would affect the methane content in the biogas through the $H_2 + CO_2$ reaction in the methanogenic phase [8].

Determining the optimum SS/FW ratio is a very important parameter in anaerobic digestion studies, as it can maximize biogas yield with the methane concentration [17–19]. Therefore, the results of biogas yields and methane concentrations were expressed regarding volatile solids (VS), considering the FW and SS volatile solids. The volatile solids consist of the organic phase in the fermentable solid matter. Hence, the VS was standard to express the biogas and methane yields [50,51].

The cumulative biogas and methane yields from the SS control (blank experiments) were performed using the same conditions of experiments A_1 to B_2 without FW insert. In this case, the yields were evaluated only on the 12th, 21st, and 30th days. Blank (control) experiments are important to compare the biogas and methane yields without inserting both substrates.

All experiments are summarized in Table 2. These experiments were carried out for 30 days at a temperature of 30 °C ± 2 °C, with manual agitation four times a day.

The methane and carbon dioxide content in each SS/FW ratio were analyzed by gas chromatography (GC) using a gas chromatograph HP 5890 with a thermal conductivity detector (TCD). The column used was a Porapak-N: 6.0 m x 2.5 mm i.d. The injector and detector temperatures were 100 °C. The GC oven temperature was 40.0 °C (3.0 min), heated at 20.0 °C·(1 min) to 100.0 °C (2.0 min). Nitrogen was a carrier gas at a constant flow of 30.0 mL·min^{-1}. The volume of the biogas injected (splitless mode) was 100 μL, using a 1000 μL GC syringe. The GC gas standard was a mixture of CH_4 (55%), CO_2 (40%), H_2 (1%), and N_2 (4% for balance), provided by White Martins Inc., with 99.9% purity. For experiments B_1 and B_2, the residual hydrogen content was measured by GC at the same temperatures and nitrogen flow rate. However, a 5A molecular sieve column, 3.0 m x 2.5 mm i.d, was used.

Table 2. Anaerobic digestion experimental resume.

Experiment	I (g)	FW (g)	SS/FW (g·g^{-1})	Water (g)	Control (blank)
A_1	1.00	9.00	0.11	20.00	1.00 g (I) + 20 g (water)
A_2	2.15	8.00	0.27	19.85	2.15 g (I) + 20 g (water)
A_3	3.00	7.00	0.43	20.00	3.00 g (I) + 20 g (water)
A_4	8.25	1.75	4.71	20.00	8.25 g (I) + 20 g (water)
A_5	9.00	1.00	9.00	20.00	9.00 g (I) + 20 g (water)
B_1	8.25*	1.75	4.71	20.00	8.25 g (I) + 20 g (water)
B_2	9.00*	1.00	9.00	20.00	9.00 g (I) + 20 g (water)

T = 30 °C ± 2 °C; *0.16 mmol of hydrogen at the days 7th and 18th.

Analysis of variance

The analysis of variance (ANOVA) was performed using the best results concerning the biogas and methane concentrations in the AD experiments with no hydrogen injected. The best results were obtained in experiments A_3, A_4, and A_5. In these analyses, the independent variables were the SS/FW ratios and the digestion time (DT) [17–19]; and the dependent variable was the cumulative methane yield in terms of VS [50–51]. The pH and temperature were not evaluated in this statistical study, but they were quantified during the process, and the results were discussed [28,33,52]. All experiments were carried out according to Table 3.

Table 3. Experimental design for analysis of variance.

Experiment	SS (g)	FW (g)	SS/FW	DT (days)
A_3	3.00	7.00	0.43 g·g^{-1} (-1)	12 (-1), 21 (0), 30 (+1)
A_4	8.25	1.75	4.71 g·g^{-1} (0)	12 (-1), 21 (0), 30 (+1)
A_5	9.00	1.00	9.00 g·g^{-1} (+1)	12 (-1), 21 (0), 30 (+1)

A 3^2 factorial design was developed, and the experimental conditions were: SS/FW ratios (g·g^{-1}) 0.43 (-1), 4.71 (0) and 9.00 (+1); DT 12 days (-1), 21 days (0), and 30 days (+1), representing the experiments A_3, A_4, and A_5, respectively. In this case, ANOVA was justified to seek satisfactory methane yield in the function of the SS/FW ratios and DT within these process domains [20].

In this statistical study, a mathematical model was developed to synthesize this union of results, according to Eq. (1):

$$y = a_0 + a_1x_1 + a_2x_2 + a_3x_1x_2 \quad (1)$$

The domains of x_1 and x_2 were $\{x \in R / -1 \leq x \leq 1\}$, attributed to SS/FW ratios and DT, respectively. Coefficients a_0 to a_3 are experimentally determined model coefficients and image (y) represents the cumulative methane yield (mL.g$_{sv}^{-1}$).

The coefficient of determination (R^2) was calculated according to the analysis of variance studies [20], and it represents the approach of the mathematical model to experimental data. This coefficient configures a relation between the regression sum of squares $(\hat{y}_i - \bar{y})^2$ and the total sum of squares $(y_{ij} - \bar{y})^2$. The percentage of the variation explained, or the coefficient of determination (R^2), was calculated according to Eq. (2):

$$R^2 = \frac{\sum_i^m \sum_j^n (\hat{y} - \bar{y})^2}{\sum_i^m \sum_j^n (y_{ij} - \bar{y})^2} = \frac{RSS}{RSS + rSS} = \frac{RSS}{TSS} \quad (2)$$

where y_{ij} are experimental values (i level and j repetition), $\hat{y}_i$ represents the values calculated according to the model, Eq. (1), and $\bar{y}$ represents the global mean. An F test was done to evaluate the model fit. This test was performed using the total sum of squares (TSS), regression sum of squares (RSS), residual sum of squares (rSS), and the corresponding mean squares [20]. The influence of process variables was presented using a Pareto chart, and the model visualization was done by response surface.

Kinetic modeling

Two kinetic models, First-order and Gompertz, were applied to simulate anaerobic biodegradation, using the best results obtained among the experiments described in Table 2, which were experiments A_4 and A_5.

Cumulative methane yield was fitted to the First-order kinetic model, described by Eq. (3), and the Gompertz model, described by Eq. (4) [10,21]:

$$y(t) = y_0\left[1 - e^{(-kt)}\right] \quad (3)$$

$$y(t) = y_0 e\left\{-e\left[\left(\frac{2.72R}{y_0}\right)(\gamma - t)\right] + 1\right\} \quad (4)$$

where y_0 is the methane production potential ($mL \cdot g_{vs}^{-1}$), k is the first-order hydrolysis constant (day^{-1}), R is maximum methane production rate [$mL \cdot (g_{vs} \cdot day)^{-1}$], and γ is the lag phase (days).

The kinetic study is justified to fit a model of the methane yield as a function of the digestion time, founding a natural lag phase, maximum slope, and estimating methane potential. These parameters could be used to compare different systems in different conditions [10].

Estimation of the GHG mitigation

There are several standard methodologies to calculate GHG emissions [22,54,67] by the different biomass types of disposal. This research used the Excel GHG Protocol Brazil Spreadsheet [23], a framework created by World Resources Institute (WRI) in 1998, widely used in corporate and academic calculations.

The theoretical estimate of the GHG emissions reduction, in terms of carbon dioxide equivalent (CO_{2e}), was determined using these parameters: FW disposal of 3,240 $tons \cdot year^{-1}$ (9,000 $kg \cdot day^{-1}$) [14], an average rainfall of 2,501 $mm \cdot year^{-1}$, an average temperature of 27 °C, and shallow open dump (< 5m) [23]. The unit-denominated carbon dioxide equivalent represents the integration of emissions from various GHG based on their global warming potential [57]. The main idea is not to discharge this biomass and use it as a substrate for biogas generation.

Estimation of the electrical energy production

According to the biogas yield, the electrical energy production (in terms of $MWh \cdot year^{-1}$) was determined using the methane lower heating value (LHV) of 35,500 $kJ \cdot m^{-3}$ [24]. The methane lower heating value can also be expressed, by mass, 50,000.0 $kJ \cdot kg^{-1}$ [55] (considering the methane density of 0.66 $kg \cdot m^{-3}$ [56]) or by mol, 890 $kJ \cdot mol^{-1}$ (considering the methane molar weight of 0,016 $kg \cdot mol^{-1}$) [56]. In this research, the methane potential production was measured regarding volatile solids in the batch experiments. For the estimation of the electrical energy production, the Bragança annual FW production and an efficiency of 35% for the motor-electricity generator set [25] were used, as seen in Eq. (5):

$$P = \left[CH_4\left(mL\ g_{VS}^{-1}\right)\right]\left[VS_{I+FW}\left(g_{VS}\right)\right]\left[\frac{FW_{annual}(g)}{FW_{batch}(g)}\right]\left[\frac{1\ m^3}{10^6\ ml}\right] \left[\frac{35{,}500\ kJ}{m^3}\right]\left[\frac{1\ MWh}{3.6\times10^6\ kJ}\right][0.35] \quad (5)$$

RESULTS AND DISCUSSION

Characterization of the fish waste and SS

The characterization of FW and SS is shown in Table 4.

As shown in Table 4, the FW sample presented a moisture content of 71.00%, which may favor the anaerobic digestion process due to the natural transport of nutrients and microorganisms [60]. Kafle and Kim [21] and Cadavid-Rodríguez *et al.* [15] have found similar FW moisture values, 68.7 and 74.8, respectively. Besides, FW presented total solids and volatile solids contents of 29.0% and 24.9%, respectively, representing a good fermentable material content [50,51].

The C/N ratio from FW samples was 4.5. This result may be correlated to the high contents of nitrogen and protein, 11.22% and 18.09%, respectively, which may inhibit biogas formation [27]. Other researchers have found C/N ratios of 5.7, 10.7, and 6.5 in FW samples, and despite that, in their experiments, good biogas and methane yields were obtained [15,16,26]. These results may have occurred due to other parameters influencing the AD process, such as SS/FW ratios, DT, SS type, and so forth [61–63].

The COD/BOD_5 ratio was 2.9. It is recommended that the COD/BOD_5 ratio be lower than 4.0, as this indicates a good biodegradability of the substrate [28]. The SS presented a moisture content of 94.94%, favorable to the nutrients transport [60], total solids of

Table 4. Characterization of fish waste and SS.

Fish Waste		SS	
Moisture % (w/w)	71.00	Moisture % (w/w)	94.94
pH	7.19	pH	6.90
Salt content ($g \cdot 100g^{-1}$)	0.30	Conductivity ($mS \cdot cm^{-1}$)	8,13
Phosphorus content ($g \cdot 100g^{-1}$)	0.88	COD ($gO_2 \cdot L^{-1}$)	12.140
Fat content ($g \cdot 100g^{-1}$)	7.00	BOD ($gO_2 \cdot L^{-1}$)	4.150
Protein content ($g \cdot 100g^{-1}$)	18.09	Total solids ($g \cdot L^{-1}$)	50.6
Potassium content ($mg \cdot kg^{-1}$)	1.44	Fixed solids ($g \cdot L^{-1}$)	9.7
Total solids ($g \cdot L^{-1}$)	290.0	Volatile solids ($g \cdot L^{-1}$)	40.9
Fixed solids ($g \cdot L^{-1}$)	41.0	C % (w/w)	34.54
Volatile solids ($g \cdot L^{-1}$)	249.0	H % (w/w)	6.13
C % (w/w)	50.89	N % (w/w)	4.73
H % (w/w)	8.35	S % (w/w)	1.60
N % (w/w)	11.22	O % (w/w)	53.00
S % (w/w)	1.44	Anaerobic CFU	1.84×10^9
O % (w/w)	28.10	Aerobic CFU	0.33×10^9

5.06%, and volatile solids of 4.09%, comparable to others reported anaerobic sludges [10,15]. The SS C/N ratio was 7.3. In anaerobic digestion processes, the recommended values of the C/N ratio vary from 10 to 30. Values of a C/N ratio less than 10 may cause low biogas and methane yields [10,29,30]. The SS and FW C/N ratios were 7.3 and 4.5, respectively. Hence, they were lower than the recommended values in the literature [10,29,30]. However, other parameters can influence biogas production [61–63].

The anaerobic colony forming units (CFU) and the aerobic CFU presented values of 1.84×10^9 and 0.33×10^9, respectively. So, the anaerobic CFU was 6 times greater than the anaerobic CFU. These results suggested that the substrates (SS and FW) were good AD feedstocks. Furthermore, the SS anaerobic CFU value was similar to the results of 2.71×10^9 and 1.80×10^9 obtained by [65] and [66], respectively, in the same AD condition.

The elemental analysis of the FW and SS led to their chemical formulas, $C_5H_{10}O_3N$ and $C_8H_{18}O_{10}N$, respectively. These formulas were used to estimate the methane yield (M_{th}) through Eq. (6) ($C_aH_bO_cN_d$) [31]

$$M_{th}\left(mL\ g_{VS}^{-1}\right) = 1000\left[\frac{(22.415/8)(4a+b-2c-3d)}{(12a+b+16c+14d)}\right] \quad (6)$$

Hence, the SS and FW theoretical methane yields were 213 $mL \cdot g_{vs}^{-1}$ and 446 $mL \cdot g_{vs}^{-1}$, respectively. The same equation was used to estimate the biogas and methane yields for experiments A_4 and A_5 which presented the best results concerning biogas yields and methane content in the biogas. Experiment A_4 used 8.25 g of SS and 1.75 g of fish waste. Then, its calculated theoretical methane yield was 268.7 mL g_{vs}^{-1}. For experiment A_5 (9.00 g of SS and 1.00 g of fish waste), the calculated theoretical methane yield was 190.3 $mL \cdot g_{vs}^{-1}$.

These results represent the maximum theoretical methane production based on the organic matter's elemental composition. Hence, these calculated results are likely higher than those obtained in the experiments due to the strong dependence on several operative parameters of the anaerobic process.

Cumulative biogas and methane yields and methane content

The cumulative biogas yields of experiments A_1 to B_2 are shown in Fig. 2. Table 5 illustrates the cumulative biogas yield ($mL \cdot g_{vs}^{-1}$), the cumulative methane yield ($mL \cdot g_{vs}^{-1}$), and the methane content (%, v/v) data obtained on the 30th day for the experiments A_1 to B_2 and control.

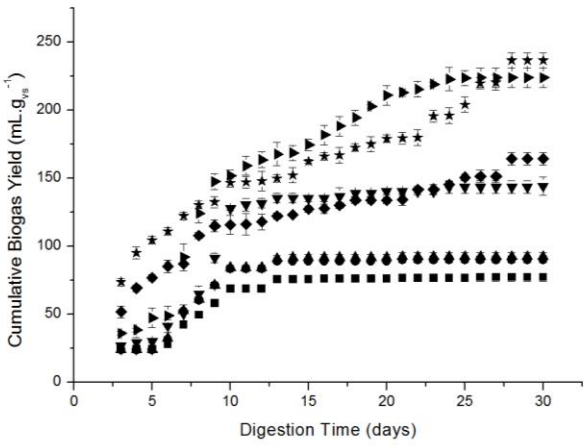

Figure 2. Cumulative biogas yield ($mL \cdot g_{vs}^{-1}$) - experiments: A_1 (■), A_2 (●), A_3 (▲), A_4 (▼), B_1 (◆), A_5 (►), B_2 (★).

The low biogas yields, and methane content, after

30 days of fermentation, for experiments A_1, A_2, and A_3 were due to the small numbers of microorganisms capable of degrading the organic matter present in the SS /FW ratios completely, respectively, 0.11 $g \cdot g^{-1}$ (A_1), 0.27 $g \cdot g^{-1}$ (A_2), 0.43 $g \cdot g^{-1}$ (A_3). The SS supplied the microorganisms to the AD process, acting as inoculum. However, 30 days (RT) seemed insufficient to form a colony capable of completely degrading the substrates due to the low SS to FW ratios. Hence, the SS/FW ratios for experiments A_1, A_2, and A_3 were inappropriate for the DT used [10,17,19]. For these reasons, the ratios used in experiments A_1, A_2, and A_3 were discontinued due to the low efficiency of the 30 days AD process.

On the order hand, the experiments A_4 (SS/FW of 4.71 $g \cdot g^{-1}$), A_5 (SS/FW of 9.00 $g \cdot g^{-1}$), B_1 (SS/FW of 4.71 $g \cdot g^{-1}$, and the 0.16 mmol of hydrogen injected on the 7th and 18th days) and B_2 (SS/FW of 9.00 $g \cdot g^{-1}$, and the 0.16 mmol of hydrogen injected on the 7th and 18th days), presented results showing that the biogas yields, methane yields, and methane contents increased. These results can be seen in Table 5 and Fig. 3. According to Table 5 and Fig. 3, the biogas yields ranged between 80 $mL \cdot g_{vs}^{-1}$ and 140 $mL \cdot g_{vs}^{-1}$, with the methane content exceeding 50%. These results showed an increase in the microbial population due to a higher SS content in AD reactors, enabling the substrate organic matter for SS and FW to degrade more efficiently. These results were similar to 50 $mL \cdot g_{vs}^{-1}$–200 $mL \cdot g_{vs}^{-1}$ of methane yields and 50%–75% of methane content obtained by other researchers [6,15,16,32].

Table 5. Summary of anaerobic digestion results on the 30th day.

Experiment	Cumulative Biogas Yield ($mL \cdot g_{vs}^{-1}$)	Biogas Yield from control ($mL \cdot g_{vs}^{-1}$)	Cumulative Methane Yield ($mL \cdot g_{vs}^{-1}$)	Methane Yield from control ($mL \cdot g_{vs}^{-1}$)	Methane Percentual in volume (%, v/v)
A_1	77.29 ± 2.95	10.05 ± 0.75	6.11 ± 0.70	0.77 ± 0.08	7.58 ± 1.48
A_2	90.06 ± 2.31	16.85 ± 0.81	9.90 ± 1.05	1.85 ± 0.11	11.10 ± 2.50
A_3	92.46 ± 2.92	18.30 ± 1.02	18.02 ± 5.50	3.48 ± 0.49	19.47 ± 5.35
A_4	144.21 ± 6.81	30.91 ± 1.45	75.52 ± 5.47	6.48 ± 0.58	52.37 ± 1.32
A_5	224.03 ± 7.11	40.30 ± 1.87	137.94 ± 9.29	9.92 ± 0.85	61.57 ± 2.19
B_1	164.26 ± 5.45	56.91 ± 2.09	89.52 ± 5.40	10.85 ± 0.63	54.50 ± 2.78
B_2	236.59 ± 5.69	81.02 ± 3.12	157.18 ± 8.94	17.81 ± 0.81	66.54 ± 5.38

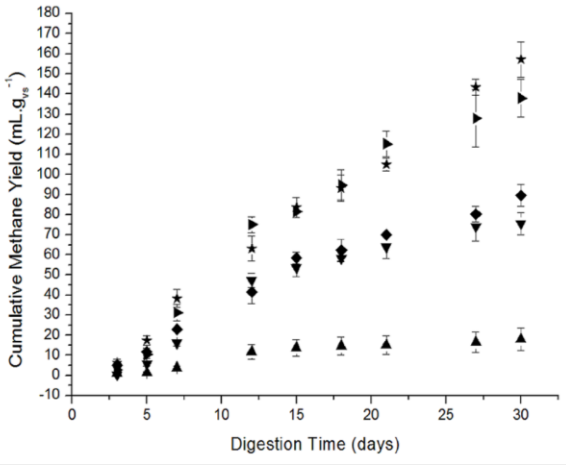

Figure 3. Cumulative methane yield ($mL \cdot g_{vs}^{-1}$) - experiments: A_3 (▲), A_4 (▼), B_1 (♦), A_5 (►), B_2 (✱).

In the AD processes, several parameters affect the biogas yield and methane content. These parameters are, for instance, the substrate (S) type and composition, type of inoculum (I) used to start up the AD, the I/S ratio, moisture content, temperature, pH, agitation, and digestion time [15,17,19,21,28,33,60]. In this research, the variation of temperature and pH were not studied. However, in all experiments, the temperatures were kept at 30 °C ± 2 °C and the pH varied between 6.2 and 7.4. When the pH ranges between 5.5 and 6.0, acidogenic bacteria increase, impairing the fermentative process. Conversely, methanogenic bacteria increase with pH values ranging from 6.8 to 7.2, favoring the fermentative process [28]. When the pH is below 8.0, the nitrogen remains in aqueous ammonium form NH_4^+. However, when pH exceeds 8.0, the methanogens community is affected, inhibiting methane production [33].

After 30 days, the methane contents obtained in experiments A_4 and B_1 were 52.37% ± 1.32% and 54.50% ± 1.78%, originating at the same SS/FW ratio (4.71 $g \cdot g^{-1}$). However, experiment B_1 used 0.16 mmol of hydrogen added on the 7th and 18th days. As a result, there was an increase in the methane content of 4.06% for B_1. Similarly, after 30 days, the methane contents from experiments A_5 and B_2 were 61.57% ± 2.19% and 66.44% ± 2.17%, originating at the same SS/FW ratio (9.00 $g \cdot g^{-1}$). But, experiment B_2 used 0.16 mmol of hydrogen added on the 7th and 18th days. Hence, there was an increase of 7,9% in the methane content in the biogas. This augmentation of the methane content in the biogas in the experiments in which hydrogen was injected may suggest the researches were capable of

synthesizing more methane in the methanogenesis phase of the AD process, as there was more hydrogen available for the carbon dioxide and hydrogen reactions, as suggested by some researchers [8,61–62]. Further experiments injecting hydrogen in the AD reaction are necessary to obtain more detailed and confident data on the influence of hydrogen in the biogas methane content. The influence of the injected hydrogen on the biogas methane content will be investigated.

Despite the experiments using hydrogen, B_1, and B_2 produced interesting and promising results, more investigation will be needed to establish the effect of the injected hydrogen on the biogas methane content. This matter will be considered for future research. For this reason, experiments A_3, A_4, and A_5 were selected to continue the ANOVA, and only A_4 and A_5 for the kinetics, GHG emissions reduction, and electrical energy production studies.

Cumulative methane yield and analysis of variance (ANOVA)

The evolution of methane yield depended on the SS/FW ratio and DT (independent variables). An ANOVA was performed for experiments A_3, A_4, and A_5 to verify the effect of the SS/FW ratio and DT on the methane yield. The ANOVA results are shown in Table 6.

According to Table 6, the results indicated that SS/FW ratios and DT were significant to methane yield. Among them, the influence of the SS/FW ratio was the most significant. The inoculum/substrate ratio can affect not only the biodegradability but also the methane production rate and/or hydrolysis rate [10,17]. SS provided the microbes for the organic matter degradation in the co-digestion experiments. At the same time, FW was the fresh substrate with insufficient microbes to decompose the organic matter faster and more efficiently.

The combined effect (x_1x_2) was significant. The diversity of combined effects and the dynamism of the process need a complex mathematical model. So, the mathematical model that described the methane yields in the domain of experimental design is shown in Eq. (7).

$$y\left(mL\ g_{VS}^{-1}\right) = 62.211 + 47.219x_1 + 16.224x_2 + 14.140x_1x_2 \quad (7)$$

The domains of x_1 and x_2 were $\{x \in R / -1 \leq x \leq 1\}$, and they were attributed to SS/FW ratio and DT, respectively, as described in Table 3. Furthermore, an *F* test was performed, and this model was observed to be statistically significant because F_1 (RMS/rMS) was higher than $F_{3,14}$, 807.90 > 5.56, respectively. Also, this model was predictive because F_2 (LFMS/PEMS) was less than $F_{5,9}$, 5.35 < 6.63 [20]. Finally, the proportion of the explained variation relative or coefficient of determination was 0.99, which indicated a good approximation of the analytical model to the experimental data.

Table 6. Study of analysis of variance - experiments A_3 to A_5.

Experiment	SS/FW	DT (days)	Experimental Designed	CH_4 ($mL \cdot g_{vs}^{-1}$)	
A_3	0.43 (-1)	12 (-1)	-1 -1	11.73 ± 3.48	
A_3	0.43 (-1)	21 (0)	-1 0	15.18 ± 4.63	
A_3	0.43 (-1)	30 (+1)	-1 +1	18.02 ± 5.50	
A_4	4.71 (0)	12 (-1)	0 -1	47.31 ± 3.40	
A_4	4.71 (0)	21 (0)	0 0	63.89 ± 5.79	
A_4	4.71 (0)	30 (+1)	0 +1	75.52 ± 5.47	
A_5	9.00 (+1)	12 (-1)	+1 -1	75.09 ± 4.00	
A_5	9.00 (+1)	21 (0)	+1 0	115.21 ± 6.44	
A_5	9.00 (+1)	30 (+1)	+1 +1	137.94 ± 9.29	
RSS	31,513.88	Df	3	RMS	10,504.63
rSS	182.03	Df	14	rMS	13.00
TSS	31,695.91	Df	17	F_1 (RMS/rMS)	807.90
Lack of fit (LFSS)	136.19	Df	5	LFMS	27.24
Pure error (PESS)	45.84	Df	9	PEMS	5.09
R^2(RSS/RSS+rSS)	0.994			F_2(LFMS/PEMS)	5.35

Figures 4a and 4b illustrate the mathematical model, Eq. (7), and the Pareto chart, which shows the influence of the variables on the methane yield, respectively. Experiments A_4 and A_5 will be considered for the kinetic study, energy production estimate, and GHG reduction.

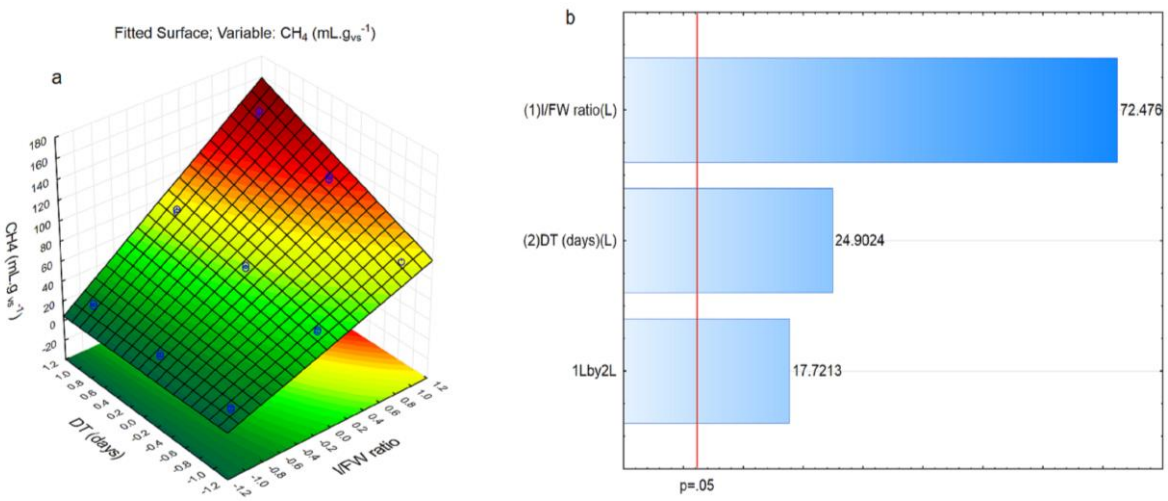

Figure 4. Fitted surface (a) and Pareto chart (b) - dependent variable: CH_4 yield ($mL \cdot g_{vs}^{-1}$).

Kinetic modeling

A kinetic study was performed for a DT of 30 days with SS/FW ratios equal to 4.71 $g \cdot g^{-1}$ (A_4) and 9.00 $g \cdot g^{-1}$ (A_5). Two kinetic models were fitted, the First-order kinetic model (Eq. 3) and the Gompertz model (Eq. 4). The results are shown in Figure 5. The model's parameters are shown in Table 7.

The first-order model considers continuous methane production, with a maximum production rate at the beginning of the AD process. Differently, the Gompertz model considers a lag phase before methane production starts and a maximum production rate during the process. And so, the results showed a better approximation of the Gompertz model ($R^2 > 0.97$) compared to the first-order model ($R^2 > 0.91$).

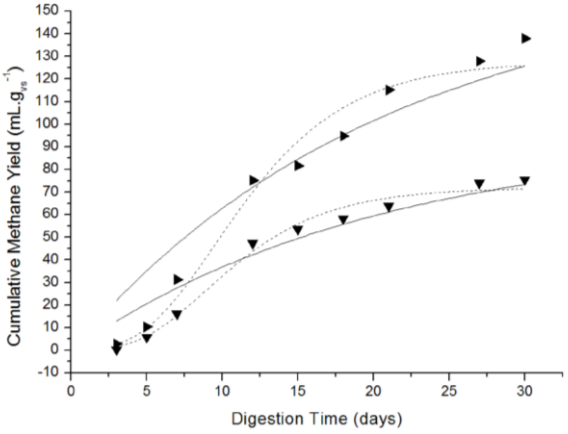

Figure 5. Kinetic study of the cumulative methane yield ($mL \cdot g_{vs}^{-1}$) - first-order model (solid line) and Gompertz model (dash line) - A_4 (▼), A_5 (►).

Table 7. Parameters of the kinetic models.

Experiment	First-order model			Gompertz model			
	y_0 ($mL \cdot g_{vs}^{-1}$)	k (day^{-1})	R^2	y_0 ($mL \cdot g_{vs}^{-1}$)	R ($mL \cdot g_{vs}^{-1} \cdot day^{-1}$)	γ (day)	R^2
A_4	95.661 ± 5.371	0.049 ± 0.005	0.912	71.996 ± 1.890	6.225 ± 0.398	4.502 ± 0.449	0,985
A_5	164.509 ± 8.882	0.048 ± 0.004	0.921	127.766 ± 4.984	10.415 ± 1.109	4.714 ± 0.676	0,970

The presence of lag phases and maximum derivatives of methane yields ($\partial y/\partial t$) were observed in other research [10,21], suggesting an initial period since the hydrolyses process to methanogenic reaction (obviously after acidogenic and acetogenic ways).

GHG emission reduction and estimate of energy production

In a real process involving biogas formation by biodigestion, it is necessary to perform a complete study with several parameters (economic, operational, and logistic, among others).

At the end of this research, two scenarios were presented, performed by experiments A_4 and A_5, both in a batch study. Moreover, the annual FW production from Bragança (Brazil) was 3,240 $tons \cdot year^{-1}$. This information was necessary to calculate the GHG emission reduction estimate and electrical energy production. Furthermore, a summarized study of the possible biogas plant implementation was conducted in

similar conditions.

GHG emission reduction

Using the Excel GHG Protocol Brazil Spreadsheet, with a waste amount of 3,240 tons·year^{-1}, and applying these conditions: average rainfall of 2,501 mm·year^{-1}, an average temperature of 27 °C, in a shallow open dump (< 5 m); the results showed an expected GHG reduction of 1,619 tons of CO_{2e} (cumulative reduction for 20 years). Regarding methane reduction, with a global warming potential of 1/25 compared to CO_{2e} [57], a reduction of 64.76 tons of CH_4 was observed (1,619/25 tons of CH_4). Or, in volume, 98,121 m^3 (considering the methane density of 0.66 kg·m^{-3} [56]). Considering the biomass amount of 3,240 tons, the methane emission reduction would be 30.28 m^3·ton^{-1} (98,121/3,240 cubic meters per ton). This result can be compared with 26-62 m^3CH_4·ton^{-1}, calculated from the LandGEM 3.02 model, using refractory organic compounds and/or easily degradable organic compounds for 20 years [54].

Estimate of the energy production

Conform was mentioned, and experiments A_4 and A_5 were considered to guide this research. To experiment A_4, the methane production potential was 75.52 mL·$g_{vs}$$^{-1}$, and the SS/FW proportion was 8.25 g per 1.75 g, respectively. So, the weight from volatile solids was 0.77 g (8.25x0.0409 + 1.75x0.249). To experiment A_5, the methane production potential was 137.94 mL·$g_{vs}$$^{-1}$, and the SS/FW ratio was 9.00 g per 1.00 g, respectively. So, the weight from volatile solids was 0.62 g (9.00x0.0409 + 1.00x0.249).

For experiments A_4 to A_5, the results of the estimation of the production of energy (P, MWh·year^{-1}) were calculated by Eq. (5), with respective values, which Eq. (5a) is correlated to experiment A_4, and Eq. (5b) is correlated to experiment A_5.

$$P = \left[75.52\left(mL\ g_{VS}^{-1}\right)\right]\left[0.77\left(g_{VS}\right)\right]\left[\frac{3.24\times10^{9}\left(g\right)}{1.75\left(g\right)}\right]\left[\frac{1\ m^3}{10^6\ mL}\right]\left[\frac{35{,}500\ kJ}{m^3}\right]\left[\frac{1\ MWh}{3.6\times10^6\ kJ}\right]\left[0.35\right] = 371.58 \quad (5a)$$

$$P = \left[137.94\left(mL\ g_{VS}^{-1}\right)\right]\left[0.62\left(g_{VS}\right)\right]\left[\frac{3.24\times10^{9}\left(g\right)}{1.00\left(g\right)}\right]\left[\frac{1\ m^3}{10^6\ mL}\right]\left[\frac{35{,}500\ kJ}{m^3}\right]\left[\frac{1\ MWh}{3.6\times10^6\ kJ}\right]\left[0.35\right] = 956.36 \quad (5b)$$

Finally, the estimated energy production varied between 372 MWh·year^{-1} and 956 MWh·year^{-1}, which would be enough to power from 310 to 797 local houses approximately (e.g., fishermen community), which have an average consumption of 1.20 MWh·year^{-1} (or 100 kWh·month^{-1}) [34,35].

Regarding electrical energy production per ton of biomass (3,240 tons·year^{-1}), the results showed a production of 0.11 MWh·ton^{-1} to 0.30 MWh·ton^{-1} (371 MWh or 956 MWh per 3,240 tons of FW). These results can be compared to 0.54 MWh·ton^{-1}, described by Ravanipour *et al.* [59], in a study of fish and shrimp waste disposed of in Bushehr, Iran [59].

Finally, the cost of energy in biogas plants was described by other researchers, such as 9.22 Indian Rupias per kWh (or approximately 0.11 USD·kWh^{-1}) [63]; or USD 1.54 kWh per 9.42 kWh, a cost of 0.16 USD·kWh^{-1} [64]. So, it's now possible to establish a relationship between electrical energy production and the cost of a biogas plant (approximately).

CONCLUSION

Highlighting the SS/FW ratios of 4.71 g·g^{-1} and 9.00 g·g^{-1}, the biogas production using anaerobic digestion of fish waste with domestic wastewater sludge was promising. The methane yields were between 76 mL·$g_{vs}$$^{-1}$ and 138 mL·$g_{vs}$$^{-1}$, and the methane content was superior to 50%. The study of analysis of variance indicated that the evolution of methane yield was dependent on the SS/FW ratio and digestion time. The First-order (R^2 > 0.91) and Gompertz kinetic models (R^2 > 0.97) fitted very satisfactorily. However, the Gompertz kinetic model presented the best adjustment. Using 9 tons·day^{-1} (or 3,240 tons·year^{-1}) of FW, the estimate of GHG reduction was 1,619 tons of CO_{2e} for 20 years, according to the GHG Protocol Brazil Spreadsheet. Finally, the estimate of electrical energy production was between 372 MWh·year^{-1} and 956 MWh·year^{-1}, which can be useful for generating energy for more than 300 local houses, increasing life quality, and developing a circular economy for the community.

ACKNOWLEDGMENTS

Post-Graduate Program in Chemical Engineering of the Universidade Federal de Pernambuco; Universidade Federal do Pará (Bragança Campus); Escola Politécnica da Universidade de Pernambuco; and the Capes Foundation, for the grant awarded to the researcher.

REFERENCES

[1] A.R. Picos-Benítez, J.M. Peralta-Hernández, J.D. López-Hincapié, A. Rodríguez-García, J. Water Process. Eng. 32 (2019) 100933. https://doi.org/10.1016/j.jwpe.2019.100933.

[2] K. Ivanovs, K. Spalvins, D. Blumberga, Energy Procedia

147 (2018) 390–396. https://doi.org/10.1016/j.egypro.2018.07.108.

[3] A.K. Rai, H.C. Swapna, N. Bhaskar, P.M. Halami, N.M. Sachindra, Enzyme Microb. Technol. 46 (2010) 9–13. https://doi.org/10.1016/j.enzmictec.2009.09.007.

[4] E.U. Kiran, Y. Liu, Fuel 159 (2015) 463–469. https://doi.org/10.1016/j.fuel.2015.06.101.

[5] Y. Ren, M. Yu, C, Wu, Q. Wang, M. Gao, Q. Huang, Y. Liu, Bioresour. Technol. 247 (2018) 1069–1076. https://doi.org/10.1016/j.biortech.2017.09.109.

[6] G.K. Kafle, S.H. Kim, K.I. Sung, Bioresour. Technol. 127 (2013) 326–336. https://doi.org/10.1016/j.biortech.2012.09.032.

[7] J. Moestedt, J. Malmborg, E. Nordell, Energies 8 (2015) 645–655. https://doi.org/10.3390/en8010645.

[8] M. Szuhaj, N. Ács, R. Tengölics, A. Bodor, G. Rákhely, K.L. Kovács, Z. Bagi, Biotechnol. Biofuels 9 (2016) 1–14. https://doi.org/10.1186/s13068-016-0515-0.

[9] W.B. Aoun, B. Gabrielle, B. Gagnepain, OCL: Oilseeds Fats, Crops Lipids 20 (2013) 1–12. https://doi.org/10.1051/ocl/2013027.

[10] L.A. Santos, R.B. Valença, L.C.S. Silva, S.H.B. Holanda, A.F.V. Silva, J.F.T. Jucá, A.F.M.S. Santos, J. Clean. Prod. 256 (2020) 120389. https://doi.org/10.1016/j.jclepro.2020.120389.

[11] I.U. Khan, M.H.D. Othman, H. Hashim, T. Matsuura, A.F. Ismail, M. Rezaei-DashtArzhandi, I.W. Azelee, Energy Convers. Manag. 150 (2017) 277–294. https://doi.org/10.1016/j.enconman.2017.08.035.

[12] B. Bharathiraja, T. Sudharsana, J. Jayamuthunagai, R. Praveenkumar, S. Chozhavendhan, J. Iyyappan, Renew. Sust. Energ. Rev. 90 (2018) 570–582. https://doi.org/10.1016/j.rser.2018.03.093.

[13] K.A. Lyng, A.E. Stensgård, O.J. Hanssen, I.S. Modahl, J. Clean. Prod. 182 (2018) 737–745. https://doi.org/10.1016/j.jclepro.2018.02.126.

[14] J.L. Freire, B.B. Silva, A.S. Souza, Economic and hygienic-sanitary aspects of fish marketing in the city of Bragança (PA) (In Portuguese), https://pdfs.semanticscholar.org/0ddb/5cb49498dba19d786534920b0b8e5a7613e0.pdf (accessed 03 January 2023).

[15] L.S. Cadavid-Rodríguez, M.A. Vargas-Muñoz, J. Plácido, Sustain. Energy Technol. Assess. 34 (2019) 110–115. https://doi.org/10.1016/j.seta.2019.05.006.

[16] U. Choe, A. M. Mustafa, H. Lin, J. Xu, K. Sheng, Bioresour. Technol. 283 (2019) 340–349. https://doi.org/10.1016/j.biortech.2019.03.084.

[17] V. Moset, N. Al-zohairi, H.B. Møller, Biomass Bioenergy 83 (2015) 474–482. http://dx.doi.org/10.1016/j.biombioe.2015.10.018.

[18] S.Y. Xu, O.P. Karthikeyan, A. Selvam, J.W.C. Wong, Bioresour. Technol. 126 (2012) 425–430. http://doi.org/10.1016/j.biortech.2011.12.059.

[19] J. Xu, A.M. Mustafa, K. Sheng, Environ. Technol. 38 (2016) 2517–2522. http://dx.doi.org/10.1080/09593330.2016.1269837.

[20] B. Barros Neto, I.S. Scarminio R.E. Bruns, in How to do experiments: research and development in science and industry (in Portuguese), UNICAMP, 2nd Ed., Campinas/Brazil (2002), p.201–296. ISBN 85-268-0544-4.

[21] G.K. Kafle, S.H. Kim, J. Biosyst. Eng. 37 (2012) 302–313. http://dx.doi.org/10.5307/JBE.2012.37.5.302.

[22] S. Finnegan, S. Sharples, T. Johnston, M. Fulton, Energy 153 (2018) 256–264. https://doi.org/10.1016/j.energy.2018.04.033.

[23] Getulio Vargas Foundation, Brazilian GHG Protocol Program, https://eaesp.fgv.br/en/study-centers/center-sustainability-studies/projects/brazilian-ghg-protocol-program (accessed 16 June 2021).

[24] A.S. Souza, S. Peres, J. Eng. Appl. Res. 4 (2019) 1–9. https://doi.org/10.25286/repa.v4i2.1221.

[25] S. Achinas, V. Achinas, G.J.W. Euverink, Engineering 3 (2017) 299–307. https://doi.org/10.1016/J.ENG.2017.03.002.

[26] F. Bücker, M. Marder, M.R. Peiter, D.N. Lehn, V.M. Esquerdo, L.A.A. Pinto, O. Konrad, Renewable Energy 147 (2020) 798–805. https://doi.org/10.1016/j.renene.2019.08.140.

[27] E. Kovács, R. Wirth, G. Maróti, Z. Bagi, K. Nagy, J. Minárovits, G. Rákhely, K.L. Kóvacs, Bioresour. Technol. 178 (2015) 254–261. https://doi.org/10.1016/j.biortech.2014.08.111.

[28] M. Von Sperling, Introduction to water quality and to wastewater treatment (in Portuguese), UFMG, 1st Ed., Belo Horizonte/Brazil (2005), p. 10–100, ISBN 8570411146.

[29] A. Carvalho, R. Fragoso, J. Gominho, E. Duarte, Waste Biomass Valorization 10 (2019) 75–83. https://doi.org/10.1007/s12649-017-0048-1-

[30] S. Peres, M.R. Monteiro, M.L. Ferreira, A.F. Nascimento Junior, M.L.A.P.F. Palha, Bioenergy Res. 12 (2019) 150–157. https://doi.org/10.1007/s12155-018-9942-z.

[31] C. Roati, S. Fiore, B. Ruffino, F. Marchese, D. Novarino, M.C. Zanetti, Am. J. Environ. Sci. 8 (2012) 291–296. https://doi.org/10.3844/ajessp.2012.291.296.

[32] L. Solli, A. Schnürer, S.J. Horn, Renewable Energy 125 (2018) 529–536. https://doi.org/10.1016/j.renene.2018.02.123.

[33] J.L. Chen, R. Ortiz, T.W.J. Steele, D.C. Stuckey, Biotechnol. Adv. 32 (2014) 1523–1534. https://doi.org/10.1016/j.biotechadv.2014.10.005.

[34] O. Velasquez, Characterization and analysis of the electrical energy demand in the ZNI of the department of Nariño (in Spanish), http://sired.udenar.edu.co/886/ (accessed 18 April 2022).

[35] J.A.V. Piñas, O.J. Venturini, E.E.S. Lora, O.D.C. Roalcaba, Renewable Energy 117 (2018) 447–458. https://doi.org/10.1016/j.renene.2017.10.085.

[36] International Organization for Standardization, Meat and meat products - Determination of moisture content, https://www.iso.org/standard/6037.html (accessed 16 August 2021).

[37] International Organization for Standardization, Meat and meat products - Measurement of pH, https://www.iso.org/standard/24785.html (accessed 16 August 2021).

[38] International Organization for Standardization, Meat and meat products - Determination of total phosphorus content,

https://www.iso.org/obp/ui/#iso:std:iso:13730:ed-1:v1:en (accessed 16 August 2021).

[39] International Organization for Standardization, Meat and meat products - Determination of free fat content, https://www.iso.org/obp/ui/fr/#iso:std:iso:1444:ed-2:v1:en (accessed 16 August 2021).

[40] International Organization for Standardization, Food and feed products - General guidelines for the determination of nitrogen by the Kjeldahl method, https://cdn.standards.iteh.ai/samples/41320/e632a064184c4ed992c920bd7b22819d/ISO-1871-2009.pdf (accessed 16 August 2021).

[41] International Organization for Standardization, Fertilizers - Determination of potassium content - Titrimetric method, https://www.iso.org/standard/11317.html (accessed 16 August 2021).

[42] Food and Agriculture Organization of the United Nations, Standard for salted fish and dried salted fish of the Gadidae family of fishes, http://www.fao.org/input/download/standards/113/CXS_167e.pdf (accessed 17 August 2021).

[43] American Public Health Association, 2540 Solids, https://www.standardmethods.org/doi/10.2105/SMWW.2882.030 (accessed 16 August 2021).

[44] American Public Health Association, 2510 Conductivity, https://www.standardmethods.org/doi/10.2105/SMWW.2882.027 (accessed 16 August 2021).

[45] American Public Health Association, 5210 Biochemical Oxygen Demand (BOD), https://www.standardmethods.org/doi/10.2105/SMWW.2882.102 (accessed 16 August 2021).

[46] American Public Health Association, 5220 Chemical Oxygen Demand (COD), https://www.standardmethods.org/doi/10.2105/SMWW.2882.103 (accessed 16 August 2021).

[47] São Paulo Government, Analysis of anaerobic and aerobic colony forming units, https://www.defesa.agricultura.sp.gov.br/legislacoes/instrucao-normativa-sda-62-de-26-08-2003,665.html (accessed 17 August 2021).

[48] American Society for Testing and Materials, Standards method for the ultimate analysis of coal and coke [C, H, S, N, O] (1988) section D3176-84, p. 409–412.

[49] A. Kasinath, S. Fudala-Ksiazek, M. Szopinska, H. Bylinski, W. Artichowicz, A. Remiszewska-skwarek, A. Luczkiewicz, Renewable and Sustainable Energy Rev. 150 (2021) 111509. https://doi.org/10.1016/j.rser.2021.111509.

[50] K. Pilarski, A. A. Pilarska, P. Boniecki, G. Niedbala, K. Durczak, K. Witaszek, N. Mioduszewska, I. Kowalik, Energies 13 (2020) 1280. https://doi.org/10.3390/en13051280.

[51] B. Deepanraj, N. Senthilkumar, J. Ranjitha, Energ. Source Part A 43 (2021) 1329–1336. https://doi.org/10.1080/15567036.2019.1636902.

[52] X. Wang, R. Su, K. Chen, S. Xu, J. Feng, P. Ouyang, Front. Microbiol. 10 (2019) 1–10. https://doi.org/10.3389/fmicb.2019.00341.

[53] M. Ravanipour, A. Hamidi, A. H. Mahvi, Renewable Sustainable Energy Rev. 150 (2021) 111426. https://doi.org/10.1016/j.rser.2021.111426.

[54] S. S. Hosseini, K. Yaghmaeian, N. Yousefi, A. H. Mahvi, Global J. Environ. Sci. 4 (2018) 493–506. https://doi.org/10.22034/gjesm.2018.04.009.

[55] L. Santoli, R. Paiolo, G. Lo Basso, Energy Procedia 126 (2017) 297–304. https://doi.org/10.1016/j.egypro.2017.08.224.

[56] J. M. Smith, H. C. Van Ness, M. M. Abbott, in Introduction to Chemical Engineering Thermodynamics (in Portuguese), LTC, 7nd Ed., Rio de Janeiro (2007), p. 514. ISBN 0-07-310445-0.

[57] S. Riya, R. Imano, J. Li, H. Sun, S. Zhou, M. Hosomi, Pedosphere 32 (2022) 928–932. https://doi.org/10.1016/j.pedsph.2022.06.040.

[58] N. Pour, P. A. Webley, P. J. Cook, Energy Procedia 114 (2017) 6044–6056. https://doi.org/10.1016/j.egypro.2017.03.1741.

[59] M. Ravanipour, R. Bagherzadeh, A. H. Mahvi, J. Mater. Cycles Waste Manag. 23 (2021) 1394–1403. https://doi.org/10.1007/s10163-021-01219-2.

[60] W. L. Chow, S. Chong, J. W. Lim, Y. J. Chan, M. F. Chong, T. J. Tiong, J. K. Chin, G-T. Pan, Processes 8 (2020) 1–21. https://doi.org/10.3390/pr8010039.

[61] I. Bassani, P. G. Kougias, L. Treu, I. Angelidaki, Environ. Sci. Technol. 49 (2015) 12585–12593. https://doi.org/10.1021/acs.est.5b03451.

[62] J. C. Lee, J. H. Kim, W. S. Chang, D. Pak, J. Chem. Technol. Biotechnol. 87 (2012) 844–877. https://doi.org/10.1002/jctb.3787.

[63] A. Pal, S. Bhattacharjee, Energy 203 (2020) 117819. https://doi.org/10.1016/j.energy.2020.117819.

[64] K. Obileke, G. Makaka, N. Nwokolo, E. L. Meyer, P. Mukumba, Chemengineering 6 (2022) 1–12. https://doi.org/10.3390/chemengineering6050067.

[65] V. S. Santos, P. F. Martins, L. Borgo, P. S. A. Faria, C. F. Silva, A. Jakelaitis, Cienc. Rural 51 (2021) 1–9. https://doi.org/10.1590/0103-8478cr20200263.

[66] C. Feng, D. Cheng, Y. Feng, W. Qi, Z. Jia, L. Weaver, Y. Liu, Z. Li, J. Integr. Agric. 19 (2020) 1127–1136. https://doi.org/10.1016/S2095-3119(19)62764-4.

[67] S. Golbaz, A. H. Mahvi, M. M. Emamjomeh, A. N. Baghani, Int. J. Environ. Waste Manag. 28 (2021) 298–316. https://doi.org/10.1504/IJEWM.2021.118367.

DAYSE MARIA SÁ DA SILVA[1]
JORGE VINÍCIUS FERNANDES LIMA CAVALCANTI[1]
ADALBERTO DO NASCIMENTO FREIRE JÚNIOR[2]
SÉRGIO PERES[2]
MARILEIDE MORAES ALVES[3]
MOHAND BENACHOUR[1]

[1]Departamento de Engenharia Química, Universidade Federal de Pernambuco, Recife-PE, Brazil
[2]Escola Politécnica de Pernambuco, Universidade de Pernambuco, Recife-PE, Brazil
[3]Bragança Campus, Universidade Federal do Pará, Bragança- PA, Brazil

NAUČNI RAD

PROIZVODNJA BIOGASA I UBLAŽAVANJE GASOVA SA EFEKTOM STAKLENE BAŠTE KORIŠĆENJEM RIBLJEG OTPADA IZ BRAGANSE U BRAZILU

U ovom istraživanju je procenjen potencijal proizvodnje biogasa korišćenjem ribljeg otpada (FW) i njegov uticaj na smanjenje gasova sa efekotom staklene bašte i proizvodnju energije. Riblji otpad je ko-digestiran sa anaerobnim kanalizacionim muljem (SS). Riblji otpad je sakupljen u Braganci, u severnom Brazilu, gde je ribarska industrija glavna delatnost sa proizvodnjom ribljeg otpada od približno 9.000 kg/dan. Eksperimentalni deo obuhvatao je pet odnosa SS/FV, a u dva eksperimenta je dodat vodonik. Eksperimenti su izvedeni 30 dana i analiziran je uticaj na kumulativne prinose biogasa i metana. Smanjenje gasova sa efekotom staklene bašte je procenjeno korišćenjem količine ribljeg otpada koja nije bačena na otvorenu deponiju Bragance, a proizvodnja električne energije je izračunata korišćenjem prinosa metana. Pored toga, urađena su dva kinetička modela. Rezultati su pokazali smanjenje gasova sa efekotom staklene bašte za 1.619 tona CO_{2e} i proizvodnju električne energije od 372 MVh·godišnje do 956 MVh·godišnje. Štaviše, analiza varijanse je pokazala da je proizvodnja metana u velikoj meri zavisila od odnosa SS/FV, koji su se kretali od 76 ml/g do 138 ml/g. Konačno, ovo istraživanje je pokazalo korist od upotrebe ribljeg otpada za proizvodnju biogasa i električne energije uz smanjenje emisija gasova sa efekotom staklene bašte u gradu bez energije.

Ključne reči: biogas, energija, riblji otpad, gasovi staklene bašte, kinetički modeli, metan.

Journal of the
Association of Chemical Engineers of
Serbia, Belgrade, Serbia

Chemical Industry & Chemical Engineering Quarterly

CI&CEQ Vol. 29 Contents: Issues 1–4 YEAR 2023

No. 1

No. 2

No. 3

No. 4

Journal of the
Association of Chemical Engineers,
Belgrade, Serbia

Chemical Industry & Chemical Engineering Quarterly

CI&CEQ Vol. 29 Author Index YEAR 2023

A

B

C

D

E

F

G

H